ISSN 1590-8844
Vol. 27 No. 01
2026

International Journal of Mechanics and Control

Editor: Andrea Manuello Bertetto

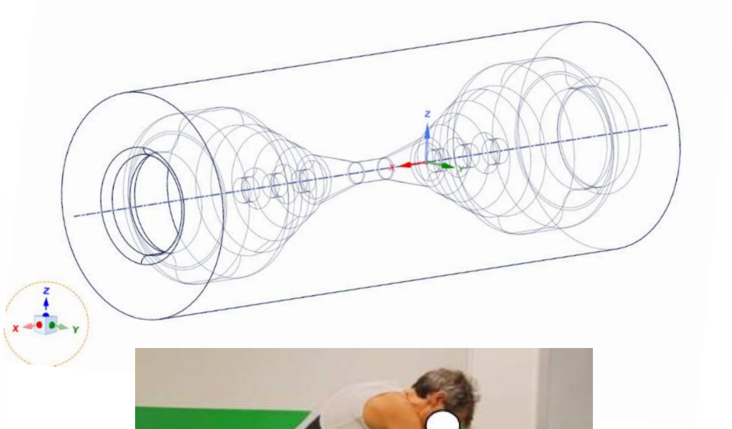

Scopus Indexed Journal

Reference Journal of IFToMM Italy
International Federation for the Promotion of Mechanism and Machine Science

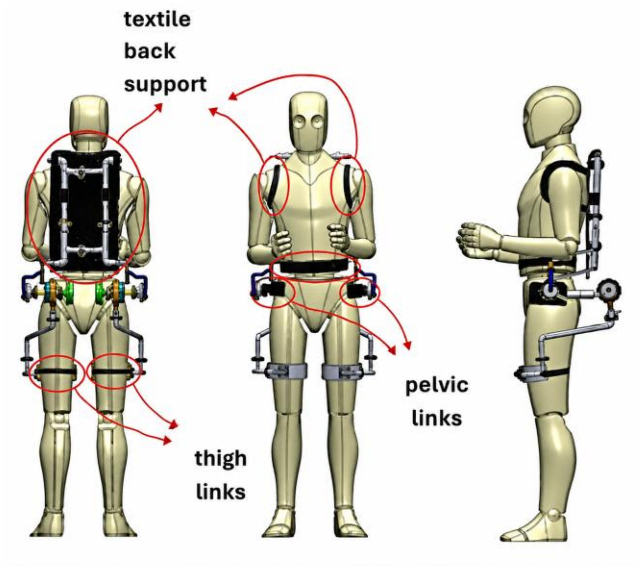

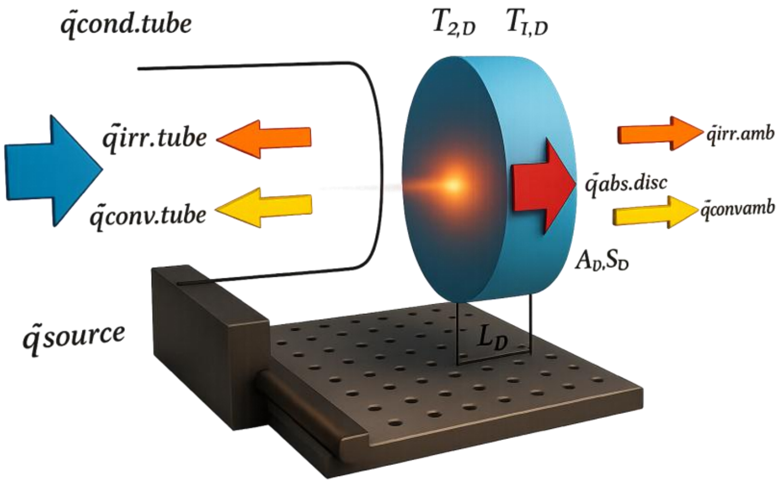

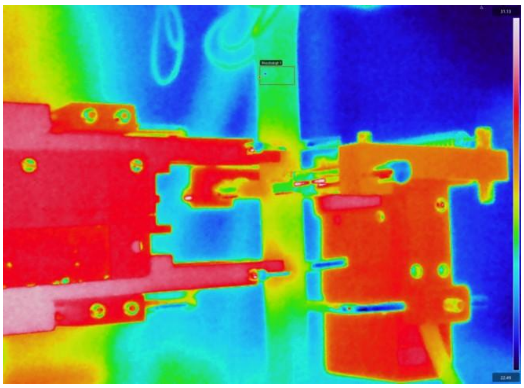

Published by ASTRA M B S.R.L.
Via Febo, 22 – 10133 – Torino (Italy)

International Journal of Mechanics and Control

Associate Editors

Published by ASTRA M B S.R.L. – Torino – Italy E.C.

Official Torino Italy Court Registration
n. 5390, 5th May 2000
Deposito presso il Tribunale di Torino
n. 5390 del 5 maggio 2000
Direttore responsabile:
Andrea Manuello Bertetto

International Journal of Mechanics and Control

The Journal is addressed to scientists and engineers who work in the fields of mechanics (mechanics, machines, systems, control, structures). It is edited in Turin (Northern Italy) by ASTRA M B S.R.L., with an international board of editors. It will have not advertising. Turin has a great and long tradition in mechanics and automation of mechanical systems. The journal would will to satisfy the needs of young research workers of having their work published on a qualified paper in a short time, and of the public need to read the results of researches as fast as possible.
Interested parties will be University Departments, Private or Public Research Centres, Innovative Industries.

Aims and scope

The *International Journal of Mechanics and Control* publishes as rapidly as possible manuscripts of high standards. It aims at providing a fast means of exchange of ideas among workers in Mechanics, at offering an effective method of bringing new results quickly to the public and at establishing an informal vehicle for the discussion of ideas that may still in the formative stages.

Language: English

International Journal of Mechanics and Control will publish both scientific and applied contributions. The scope of the journal includes theoretical and computational methods, their applications and experimental procedures used to validate the theoretical foundations. The research reported in the journal will address the issues of new formulations, solution, algorithms, computational efficiency, analytical and computational kinematics synthesis, system dynamics, structures, flexibility effects, control, optimisation, real-time simulation, reliability and durability. Fields such as vehicle dynamics, aerospace technology, robotics and mechatronics, machine dynamics, crashworthiness, biomechanics, computer graphics, or system identification are also covered by the journal.

Please address contributions to

Prof. Andrea Manuello Bertetto
PhD Eng. Matteo D. L. Dalla Vedova

Dept. of Mechanical and Aerospace Engineering
Politecnico di Torino
C.so Duca degli Abruzzi, 24
10129 - Torino - Italy

www.jomac.it
e_mail: jomac@polito.it

Subscription information

Subscription order must be sent to the publisher:

ASTRA M B S.R.L.
Via Febo, 22
10133 - Torino - Italy

e_mail: astra.mb.srl@gmail.com
mob.: +39 347 490 2080

International Journal of Mechanics and Control

Scientific Board

Published by ASTRA M B S.R.L.– Torino – Italy

Official Torino Italy Court Registration
n. 5390, 5th May 2000

Deposito presso il Tribunale di Torino
n. 5390 del 5 maggio 2000

Editor in Chief

Direttore responsabile:
Andrea Manuello Bertetto

ISSN 1590-8844
International Journal of Mechanics and Control, Vol. 27, No. 01, 2026
https://doi.org/10.69076/jomac.2026.0000

STUDY AND DESIGN OF AN ACTIVE TRUNK EXOSKELETON WITH A NON-CONVENTIONAL STRUCTURE

Gabriella Eula* Luigi Mazza* Terenziano Raparelli* Alberto Vignolo**

* Department of Mechanical and Aerospace Engineering, Politecnico di Torino, Torino Italy

** Master of Science in Mechanical Engineering, Politecnico di Torino, Torino Italy

ABSTRACT

This article presents an active industrial trunk support exoskeleton design with a non-conventional structure. A earlier design was improved, eliminating the leg links and placing two active multifunctional pneumatic actuation groups at the sides of the wearer's trunk. The backframe along the wearer's back was also eliminated, with an eye to having its function performed via the actuation groups themselves and a textile vest that can be stiffened if necessary with elastic bands inserted into pockets in the fabric. In the future, the authors plan to design an alternative solution using electric actuators. Experimental tests were carried out with a volunteer to gain a better understanding of the physiological trunk movement, while future tests will be conducted with a larger number of individuals and AI pose estimation models. Results proved useful for design optimization. The exoskeleton structure provides excellent wearability, compact dimensions, can be further optimized in weight, and is designed to fit a near-universal range of wearers.

Keywords: active trunk exoskeleton; non-conventional trunk exoskeletons; pneumatically controlled trunk exoskeleton; innovative trunk exoskeleton without leg-link

1 INTRODUCTION

Over the past several years, advances in new technologies and robotics [1-4] have fueled the spread of wearable machines, i.e., exoskeletons. Exoskeletons have been used for a variety of purposes including military, rehabilitation and nursing applications, and, more recently, industry. In the industrial sector, many types of active and passive exoskeletons have been developed [5-8] to support the trunk, arms or lower limbs, and to aid in lifting loads and maintaining a mobile sitting position. Wearable robotic exoskeletons are used in industry to support the wearer in a variety of tasks. They reduce musculoskeletal fatigue, enhance the wearer's performance and make workplace accidents less likely [9-11]. Obviously, wearer safety and comfort is a prime consideration in the use of these devices. Care must be taken to ensure that they do not put excessive stress on the wearer's body, especially in the long term, and that they are always used for their intended purpose. Ongoing studies conducted on volunteers have highlighted these devices' usefulness, and 9 out of 10 workers report that wearing an exoskeleton has improved their working lives [10]. In any case, long-term evaluations will be necessary to assess the effects these devices may have on the body of a worker wearing them, performing certain tasks, and using the device for many hours a day and for several consecutive days. This is particularly important given that the relationship between man and machine has become ever closer over the years, to the point that robots have in some cases been replaced with wearable exoskeletons. Physically demanding sectors such as agriculture, construction, and industrial mechanical production and logistics have received the most attention in this respect, as workers exert considerable effort in repetitive tasks that impose high stresses on the spinal column [12-17]. Currently, other authors have presented trunk support exoskeletons [9-11] with no leg links, though most designs feature leg links as well as a backframe [18]. They are in general wearable robots capable of limiting muscle fatigue in the lumbar region and reducing dangerous compressive loads on the spine. Patents have been filed for exoskeletons supporting

Contact author: Gabriella Eula
[1] Dept. of Mechanical and Aerospace Engineering.
E-mail: gabriella.eula@polito.it

the wearer's trunk while bending forward for many hours, some dating from as early as the beginning of the twentieth century [19] and having important applications in agriculture. Some of these designs are also interesting in terms of their actuation mechanics, as they feature noteworthy mechanisms and assemblies [20]. Analyzing the evolution of leg link geometry over the years can yield valuable insights into this component's function which can be useful in design exoskeletons with no leg links. In previous exoskeleton designs such as those presented in [19-21] and later, we find leg links consisting of: a front support on the thigh connected by a spring to the backframe [19]; leg links connected to an actuation assembly consisting of mechanical parts such as springs, locking or release stops, etc., mounted on the front of the body, with an innovative mechanism that, despite the presence of the leg link, allows unrestricted upright walking regardless of leg stance [21]; leg links consisting of rigid material with a narrow band around the thigh for agricultural and other applications [22]; leg links consisting of rigid material with a plate pressed against the leg [23, 24]; leg links consisting of flexible materials such as textiles [25-30]. For many years, the Politecnico di Torino Department of Mechanical and Aerospace Engineering (DIMEAS) has constructed exoskeleton prototypes consisting both of rigid bodies [31-36] and textile structures [37] for rehabilitation, pressotherapy, active suits, industrial purposes, etc. Simulations and other studies have also been carried out [38]. This paper presents a new type of trunk support exoskeleton with no leg links or backframe. Pneumatic actuators are used, providing a less rigid structure and ensuring that the action of the exoskeleton on the wearer's body can be changed with ease.

2 THE NEW EXOSKELETON PROTOTYPE

The exoskeleton prototype presented here is based on DIMEAS's extensive experience with exoskeletons for industrial applications [31,32,36] and for robotic neurorehabilitation [33-35, 37].

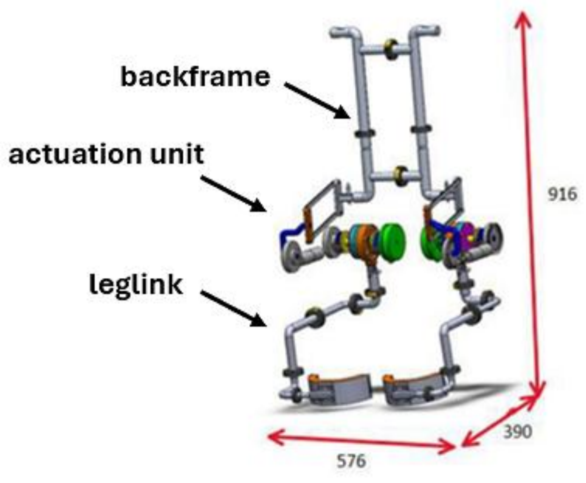

Figure 1a Earlier DIMEAS industrial trunk support exoskeleton [31,36].

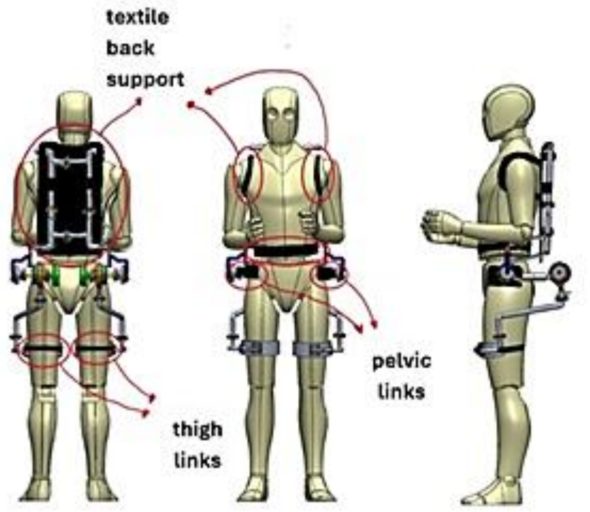

Figure 1b Details of this exoskeleton as worn [36].

Earlier industrial trunk support exoskeletons were designed with a conventional structure (Figures 1a and 1b) featuring active hip joint actuation units, a backframe carried on the wearer's back, and leg links in contact with the thigh. Optimized wearability of some of these exoskeletons is illustrated in Figures 1a and 1b [36]. In this case, the multifunctional actuation units employ electric motors. As a result of earlier studies conducted by the authors [31,32,36], these multifunction units accommodate three exoskeleton operating modes: allowing the wearer's legs to move freely during emergencies or special situations; moving the wearer's trunk in flexion or extension, providing 30% of peak muscle torque; and supporting the wearer's trunk in bending forward while stationary, when the actuation system locks the exoskeleton in the required position. To improve weights, dimensions and "legs-free" mode, the authors have designed a new geometry for an industrial trunk support exoskeleton with no leg links (Figure 2a). The new design features four pneumatic actuators at each side of the wearer's trunk (Figures 2b and 2c) that impose a rotation initially on the hip axis and then, after the physiological delay [14] between spine joint motion and hip joint motion during forward bending, on the wearer's back. Flat actuators were selected to reduce overall exoskeleton dimensions and improve wearability. Currently consisting of standard materials, these actuators can in the future be replaced with similar technopolymer actuators to further reduce weight. The backframe carried on the wearer's back was also eliminated, with an eye to having its function performed via the actuation groups themselves and a textile vest that can be stiffened if necessary by elastic bands inserted into pockets in the fabric. In this way, the top actuators move the torso C-frame slightly after the bottom actuators move the hip bar. As there are no leg links, "legs-free" mode is automatically guaranteed, with the option of immediately reducing the pressure in each cylinder, leaving the operator free to move in the event of emergencies or indisposition. To provide the delay between normal spine joint and hip joint movement [14], two devices (dubbed "delayers") were located at the end of the top rod actuators.

ISSN 1590-8844
International Journal of Mechanics and Control, Vol. 27, No. 01, 2026

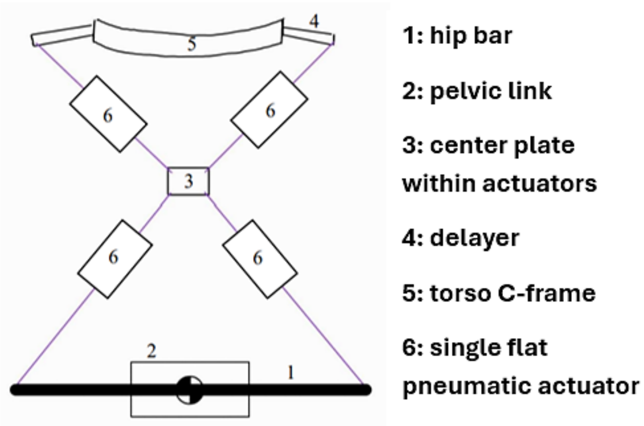

Figure 2a The new actuation unit structure.

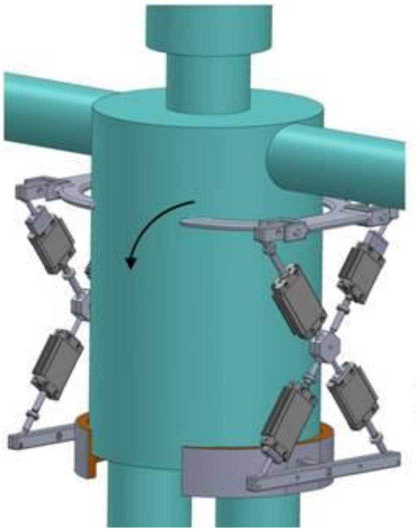

Figure 2b The new DIMEAS exoskeleton with no leg links worn by a 95%ile male.

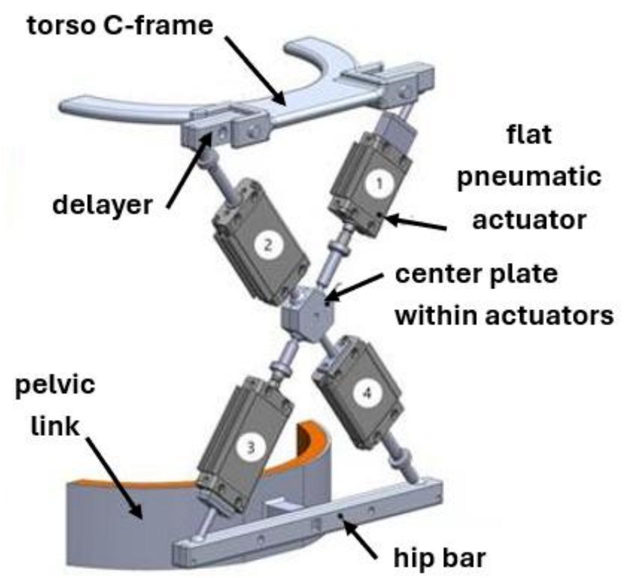

Figure 2c Details of the new DIMEAS exoskeleton with no leg links.

This actuation unit design, and the use of pneumatic actuators, also guarantee that the exoskeleton's other functions can be performed (viz., providing the required percentage of muscle torque at the hip and trunk, and fully supporting the trunk when leaning forward). Consequently, this new design also qualifies as a "multifunctional actuation unit." These units now have a pneumatic actuators, but the authors plan to design an alternative solution with electric actuators in the future. In designing exoskeletons of this type, knowledge of the human pelvis and spine is also fundamental. Accordingly, the authors reviewed key literature [12-16] and developed spreadsheets whereby they can determine the main dimensions of the human pelvis [17], especially the distance from the hip axis to the lumbosacral joint.

3 EXOSKELETON PROTOTYPE GEOMETRY AND OPERATION

As shown in Figure 3, the bottom actuators act on the hip axis by imparting a rotational motion to a bar whose length is such that the system guarantees the necessary torque-assist even at pressures below 5 bar. The top actuators act on a C-shaped component placed at a certain distance from the hip bar and called the "torso C-frame." To minimize air consumption and ensure wearer safety, the exoskeleton is designed to guarantee sufficient assistive torques with pressures below 5 bar (1 bar = 10^5 Pa). Given its structure, the actuation unit is self-balancing when the wearer is standing upright, as all four actuators are identical and supplied at the same pressure. During forward trunk flexion, the actuator axes are no longer perfectly aligned; as will be discussed below, however, this misalignment does not cause problems or place excessive forces on the wearer.

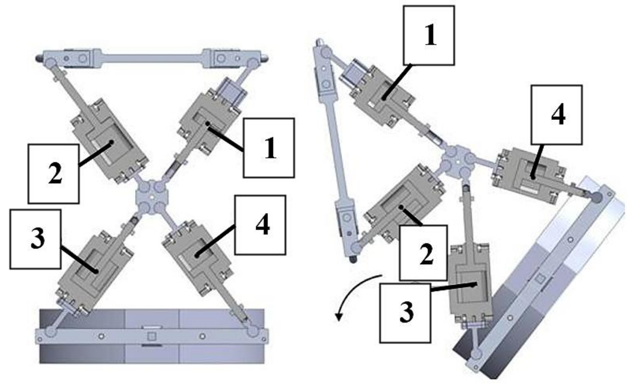

Figure 3 Details of DIMEAS exoskeleton operation.

3.1 PNEUMATIC ACTUATOR SELECTION

In selecting actuator bore and stroke, the objective was to provide the highest possible percentage of torque at the hip with pressures below 5 bar at all times. The final actuator geometry shown in Table 1 was determined on the basis of the minimum bores available in the manufacturer's catalog. Flat actuators were chosen because of the need to limit overall dimensions, improve wearability and prevent piston rotation [39]. For optimization purposes, similar commercial

Table I – Pneumatic cylinder characteristics (1 bar=10^5 Pa)

Actuator	Characteristic
Model	Festo series DZF
Bore	25 mm
Stroke	Actuator 1 = 10 mm; 2 = 40 mm; 3 = 40 mm; 4 = 25 mm
Type	Rectangular section, anti-rotation
Mass	Actuator 1 = 0.186 kg; 2 = 0.240 kg; 3 = 0.240 kg; 4 = 0.204 kg
Envisaged operating pressure	< 5 bar
Maximum operating pressure	10 bar

actuators consisting of lightweight materials such as technopolymers are now being sought.

4 WEARABILITY STUDY

Given the X-configuration of each actuation unit, it is advisable to avoid the need to make anthropometric adjustments for individual wearers which would change the distance between the hip bar and torso C-frame, and thus affect actuation unit performance and operation. Accordingly, the design of the X-configuration and the distance between the hip hinge and the C-frame was based on an in-depth anthropometric study to accommodate wearers ranging from 5th percentile women to 95th percentile men. As shown in Figures 4a and 4b (dimensions in millimeters) the current geometry will fit wearers down to 10th percentile women without modifying the arrangement of the actuation unit components. For 5th percentile women, it may be necessary to make a small geometric modification to the torso C-frame, creating a concave shape that allows the exoskeleton to fit equally well without interfering with the wearer's axillary area [40-43]

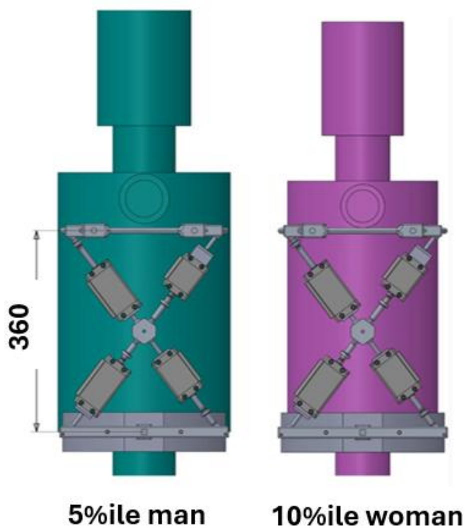

Figure 4a Distance between hip bar and torso C-frame accommodates a wide range of wearers.

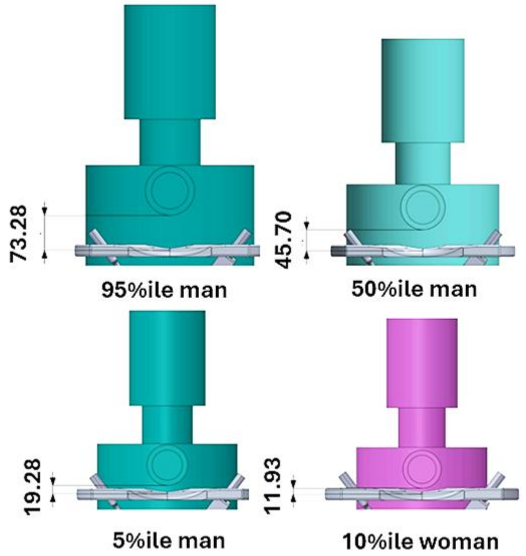

Figure 4b Distance between torso C-frame and axillary fossa in various wearers.

5 MOVEMENT STUDIES

The new exoskeleton's design was also based on experimental studies of trunk flexion. For this preliminary evaluation, a volunteer performed all movements, which were videotaped and analyzed using Tracker, a free software tool [27] (2024 version). In the future, movement studies will also be conducted with a larger number of volunteers and with pose estimation techniques using AI models (pre-trained or otherwise) developed with appropriate software as shown in Figures 5a and 5b [45,46].

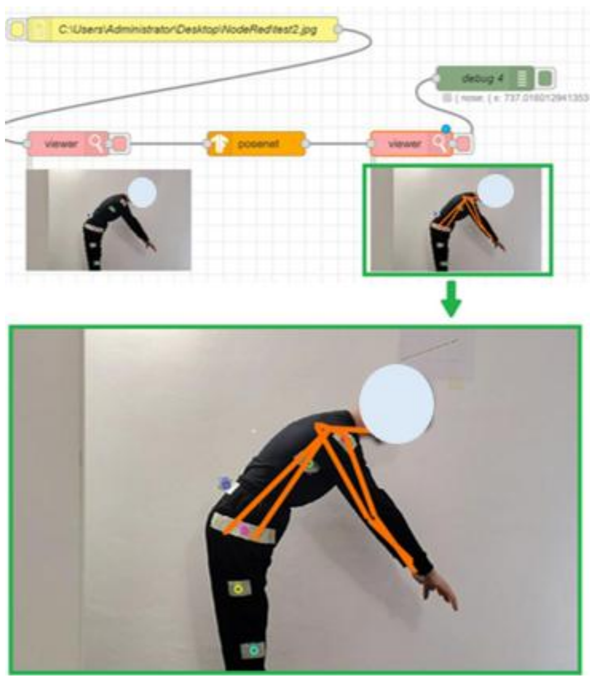

Figure 5a Pose estimation with pre-trained models in Node-RED (version 18.50, Posenet TensorFlow) [45].

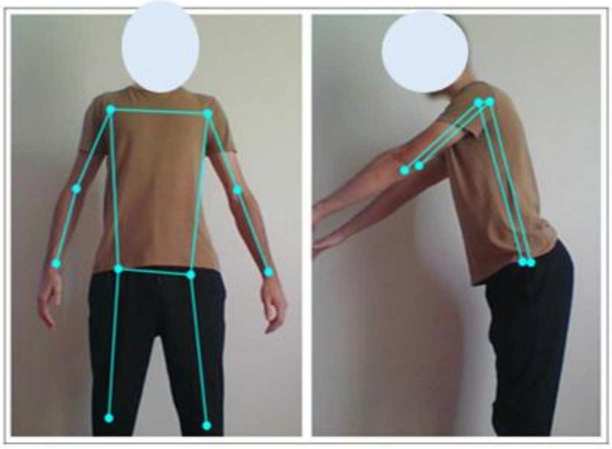

Figure 5b Pose estimation using author-trained models in Teachable Machine (version 2.0) [46].

In this exoskeleton design procedure, a single subject movement was studied because this study is focused to verify some information on this topic from the general literature but also by referring to studies and experimental tests and simulations previously conducted by the authors [.31,32,38]. The study of motion is here aimed only at the exoskeleton design and analysis the subject not wearing the exoskeleton. The authors have already begun experimental tests with other subjects and with multiple subjects (both women and men) to further their understanding of this motion in healthy individuals not wearing the exoskeleton and with the purpose only to better know this kind of movement. These studies are also now conducted by the authors using AI pose estimation models for the human body. After all these further considerations, authors will start some more verifications simulating and analyzing various kind of subjects wearing the exoskeleton.

5.1 VOLUNTEER SELECTION AND VIDEO RECORDING CONDITIONS

To expedite this initial movement study, a single volunteer was selected [12-16, 43,47,48]. Characteristic data were collected and markers were placed on the clothed volunteer so that trunk movement could be analyzed using the Tracker software. The markers were placed over the subject's clothing, since the exoskeleton will always be worn by a clothed subject. It was thus also possible to analyze clothing movements. Videos were recorded using an ordinary Android smartphone placed at a distance of 2 m from the subject. All videos were shot in the sagittal plane. A healthy volunteer's physiological trunk flexion and extension was recorded. Table II presents the volunteer's main characteristics. Studying physiological trunk motion rather than the specific motion of an individual lifting a load from the ground is essential in designing a trunk exoskeleton that respects the anatomy of the pelvis, which has two different hinges: the hip axis and the lumbosacral joint, where the spine connects to the pelvis.

It is also important to study movement dynamics to design a device that respects the delays between pelvis and spine movements [14]. A study of this type also allows for repeatability in experimental motion analysis. The exoskeleton presented here is primarily designed to support the motion of the trunk and support it when bent forward. For the moment, the case of lifting a load from the ground has not been addressed in detail.

Table II - Subject characteristics

Characteristic	Value
Gender	Male
Age	25
Profession	Mechanical engineer
Body mass	70 kg
Height	1.75 m
Right-handed/left-handed	Right-handed
Sports	Trekking
Surgical operations	None
Hip axis to lumbosacral joint	160 mm
Hip axis to axillary fossa	450 mm
Hip axis to neck attachment	550 mm
Hip axis to top of head	820 mm
Hip axis to knee axis	430 mm
Pelvis width	340 mm
Hip axis to torso C-frame	360 mm

6 EXPERIMENTAL MOVEMENT ANALYSIS

Markers were placed on the shoulder joint, at the point under the armpit where the torso C-frame will make contact, on the lumbosacral joint, on the hip axis, at the mid-point of the thigh and on the knee joint to correctly examine the entire physiological motion of the trunk in flexion and subsequent return to the upright position. Marker positions and motion angles of the trunk and of the pelvis are shown in Figures 6a and 6b. In particular authors underline that: α is the trunk angle; β is the torso C-frame forward flexion angle; θ is the pelvis angle.

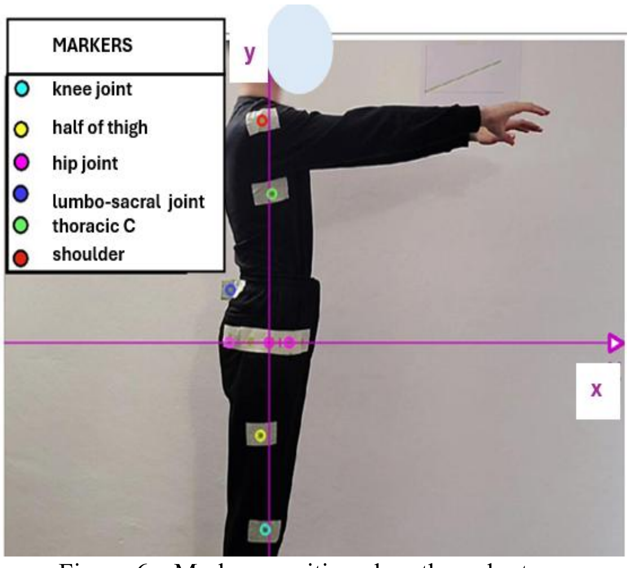

Figure 6a Markers positioned on the volunteer.

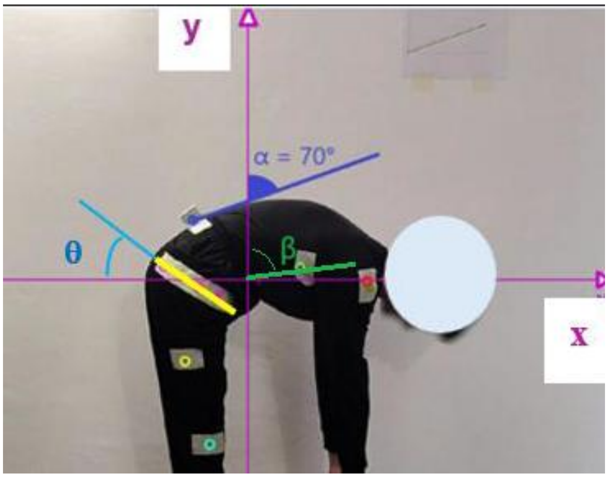

Figure 6b Motion angles used by the authors.

The experimental and theoretical curves for torso C-frame forward flexion are shown in Figure 7a. The experimental results were in complete agreement with the theoretical cycloidal law typical of this movement.

Pelvis and spine rotation angles and angular velocities are shown in Figures 7b and 7c; in particular, Figure 7c also shows motion onset and thus the physiological delay between pelvis rototranslation and trunk forward flexion [12-16].

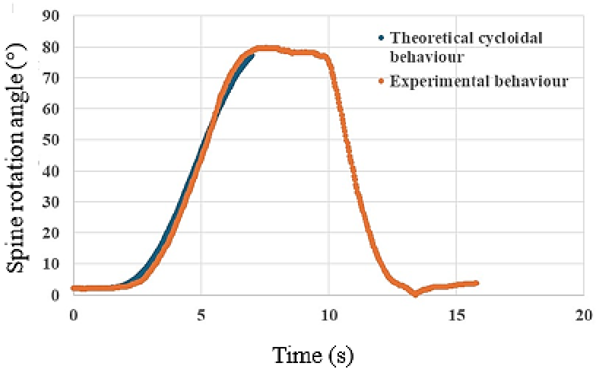

Figure 7a Experimental and theoretical curves for torso C-frame forward flexion (β angle) versus time.

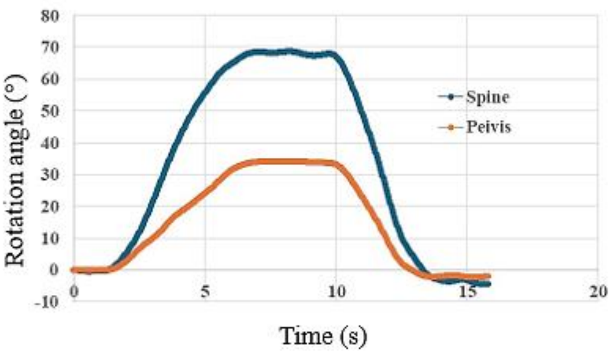

Figure 7b Pelvis (θ) and spine (α) rotation angles versus time.

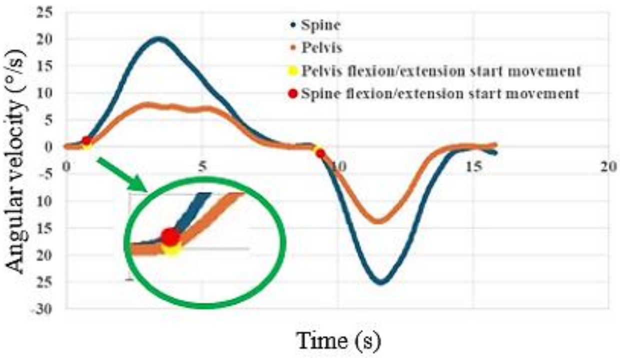

Figure 7c Pelvis and spine angular velocity versus time.

As can be seen, experimental tests and analysis are in good agreement with theory and the literature, and are consistent with normal physiological trunk motion. Figures 8a and 8b compare the current results for pelvis and spine motion during trunk forward flexion with those obtained in a preliminary experimental study carried out at DIMEAS a few years ago [32]. Current results are shown in Figure 8a, while results of the earlier tests are shown in Figure 8b. It should emphasized that the curves and displacements from the current study are consistent with those obtained in the 2019 study with different subjects and motion tracking methods [32]. During trunk flexion, the pelvis undergoes a rototranslation. In [14,15] with a trunk flexion of 63.89°, pelvic backward shift is approximately 146 mm, while under other test conditions, it is approximately 160 mm, as determined in earlier experimental tests conducted at DIMEAS (2019 with a 25 year old male subject [32]). In the current motion analysis, pelvic backward shift was approximately 130 mm. The disparities between these values are entirely acceptable in view of the differences between the subjects and testing methods.

7 EXOSKELETON OPERATION

A model of the exoskeleton worn by the volunteer was constructed in a CAD environment (SolidWorks software version 2024) (Figure 9) to check its operation during trunk flexion and determine each actuator's lever arm with respect to the hip axis and the center of the torso C-frame, thereby obtaining the torques.

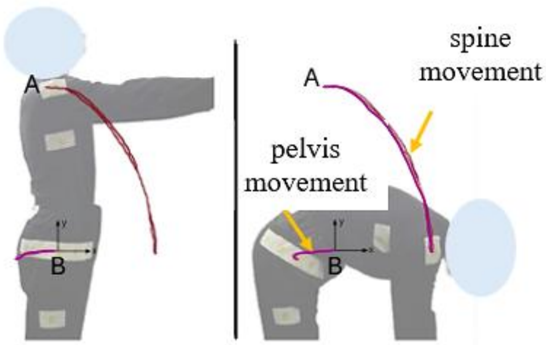

Figure 8a Pelvis and spine movements during trunk flexion determined experimentally in this study.

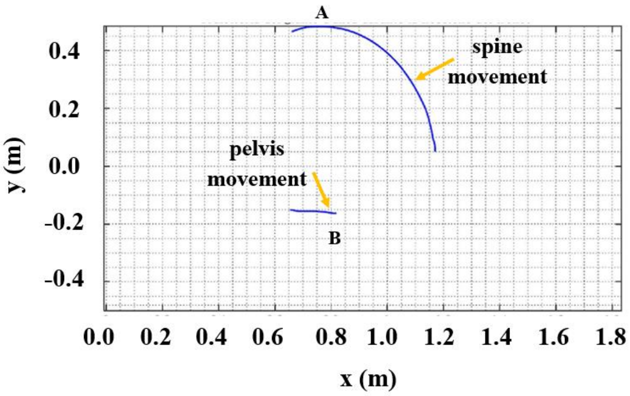

Figure 8b Pelvis and spine movements during trunk flexion determined experimentally by the authors in 2019 [32].

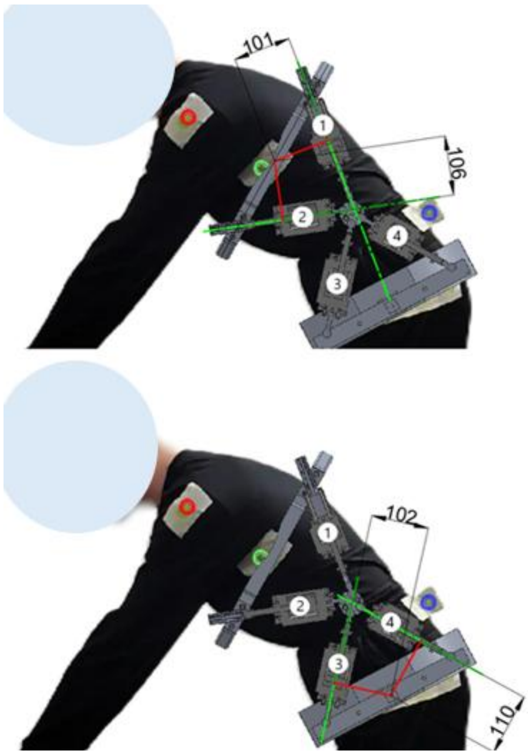

Figure 9 Cylinder lever arms relative to the hip axis and the lumbosacral joint during motion.

Obviously, exoskeleton dimensions and design have not yet been optimized. It was thus possible to evaluate lever arm variation during exoskeleton operation in trunk flexion from 0° to 70°: actuator 1 lever arm is shortened by approximately 10 mm, while that of actuator 2 remains almost constant relative to the center of the torso C-frame. Actuator 3 lever arm is shortened by approximately 10 mm, while that of actuator 4 lengthens by approximately 7 mm relative to the hip joint axis. Given this information, changes in the torque delivered by the exoskeleton during trunk flexion and extension were quantified as shown in Figures 10 a-d, where the blue bar represents the torque required with that trunk flexion angle. In particular, Figures 10a and b shows the maximum torques provided by actuators supplied at 5 bar. Practically all actuators provide much more torque than is required. Figures 10c and d show the maximum torque provided at 2 bar supply pressure. The torques thus obtained are better than those at 5 bar, as they are all lower and reduce air consumption. Supply pressure laws can thus be plotted for trunk flexion and extension (Figures 11a and 11b) to optimize the future control system. In this way, as shown in Figures 12a and 12b, all torques are optimized during movement, and are never too far above or below the maximum required muscle torque. It is important to bear in mind that the exoskeleton need only deliver a percentage of the maximum required muscle torque. This improves actuator operation and demonstrates an advantage of using pneumatic power. It can be concluded from the results reported in the bar charts (Figures 10) that having a constant power supply for the entire duration of the movement is ineffective, as it is likely to produce excessive or insufficient torques for certain trunk angles.

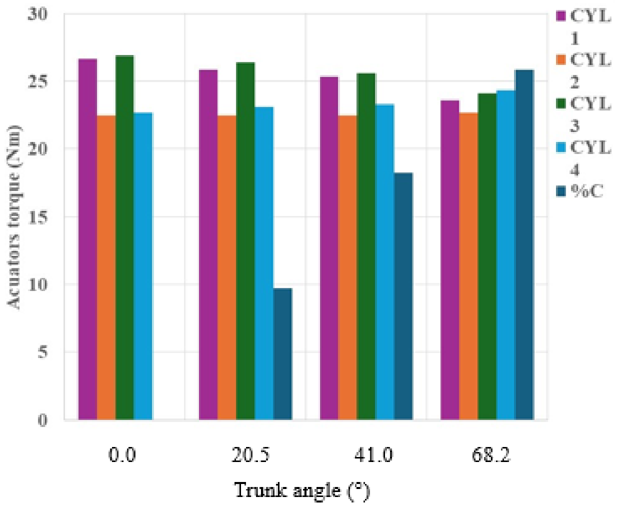

Figure 10a Actuator torque versus trunk flexion angle (supply pressure: 5 bar).

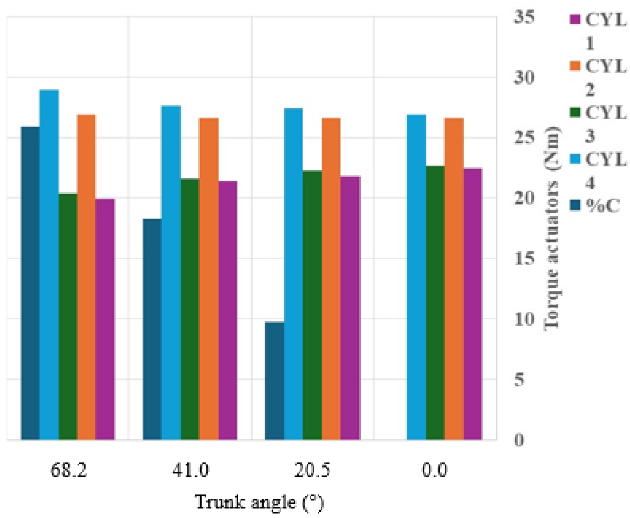

Figure 10b Actuator torque versus trunk extension angle (supply pressure: 5 bar).

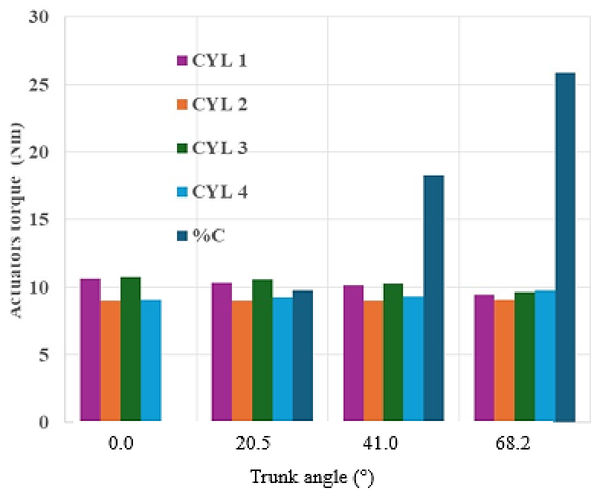

Figure 10c Actuator torque versus trunk flexion angle (supply pressure: 2 bar).

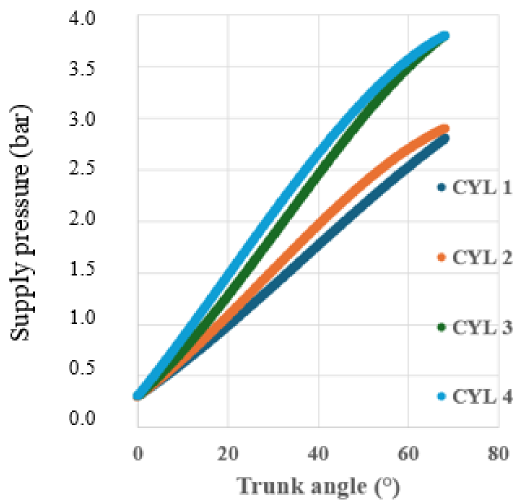

Figure 11a Optimized supply pressure versus trunk flexion angle.

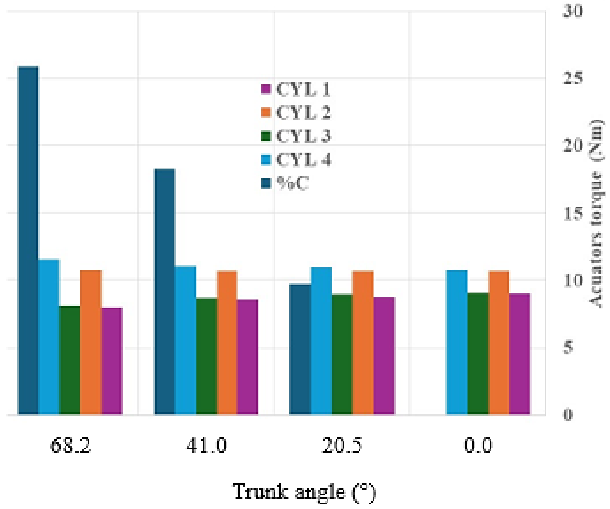

Figure 10d Actuator torque versus trunk extension angle (supply pressure: 2 bar).

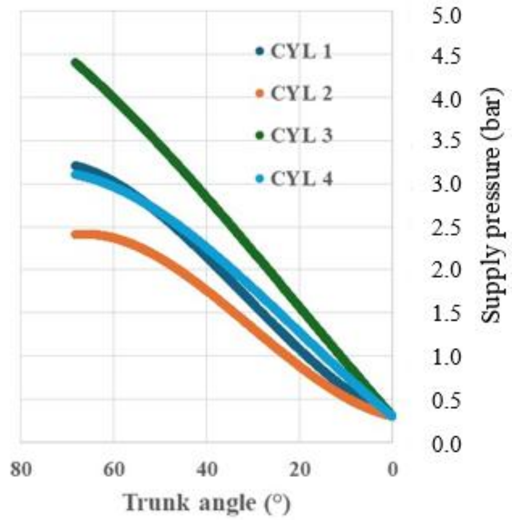

Figure 11b Optimized supply pressure versus trunk extension angle.

A time-pressure law should thus be used to ensure that the pressure reached is sufficient to obtain the correct torque for each angular position reached over time. The supply pressure law was determined interactively in such a way as to obtain the maximum percentage of active exoskeleton support at every angle reached during flexion. It was thus possible to construct the supply pressure law that, with an appropriate control system, will optimize exoskeleton operation in all phases of trunk motion (Figures 11a and 11b). Figures 12a and 12b also show the new torque percentages that can thus be obtained. Results of this analysis are very satisfactory, and useful both for understanding actual exoskeleton operation and for designing the future control system.

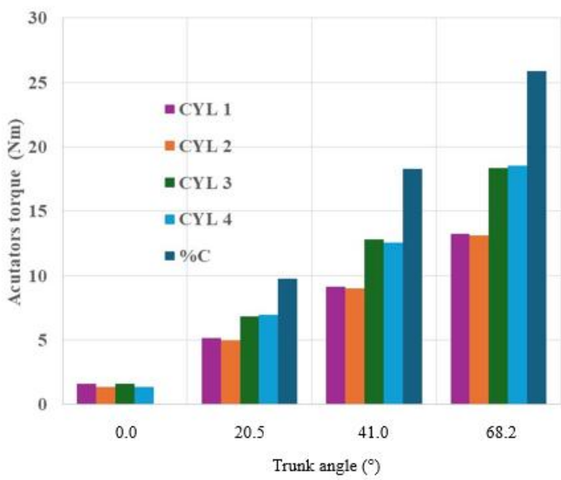

Figure 12a Actuator torque optimized via the indicated supply pressure law (trunk flexion angle).

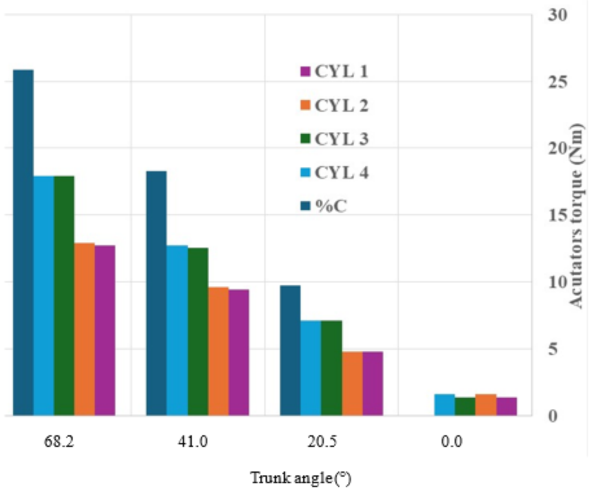

Figure 12b Actuator torque optimized via the indicated supply pressure law (trunk extension angle).

8 DELAYERS

A delay reflecting the physiological delay between spine joint motion and hip joint motion must be provided between the activation of the bottom cylinders driving the hip lever and the top cylinders driving the torso C-frame. Devices called “delayers” were thus designed that allow the top actuators to move the C-frame only after a predetermined time lapse from bottom cylinder activation [49]. With this solution, the correct delay can be provided either in parallel with the future actuator control system to ensure a high level of wearer safety, or independently (i.e., instead of the control system) to simplify the control logic. Initially, these delayers were conceived as a connecting rod hinged on one side to the C-frame and on the other to the piston of the top actuators, with an interposed damper (or spring) capable of delaying top cylinder action on the C-frame as shown in Figure 13.
Starting from this geometry, the delayers were then designed and engineered using a shock absorbing material between the actuators and C-frame. Before rigidly transmitting motion from the actuator to the C-frame, the shock absorbing material deforms viscoelastically in such a way as to create the desired delay.
A neoprene rubber with good damping properties and elasticity was selected for this purpose [49].
As shown in Figures 14a and b, the delayers are coaxial with the actuators, linked in one side to the actuator and on the other side to the C-frame. They feature a split casing consisting of two interlocking sections containing the delaying system and the mechanical transmission from the actuators to the C-frame. To study the system’s dynamic behavior, the delayer is simplified into a discrete lumped parameter model, treated as a single degree-of-freedom mass-spring-damper system as shown in Figure 15a. Simulation was performed by perturbing the system using a ramp input signal, representing actuator displacement over time. By solving the differential equation, trunk displacement depends on system mass m and the neoprene rubber’s damping β and elastic k values (Figure 15b).

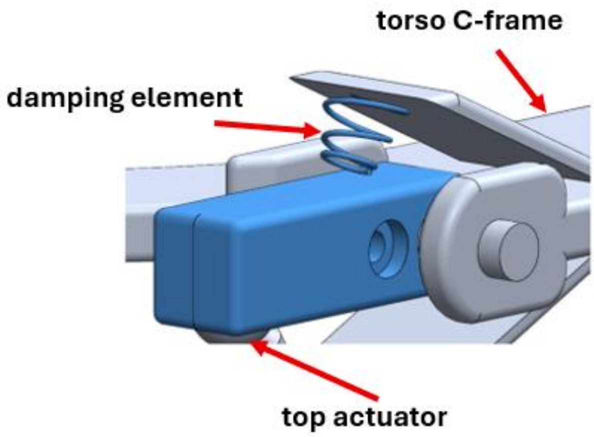

Figure 13 Preliminary delayer design.

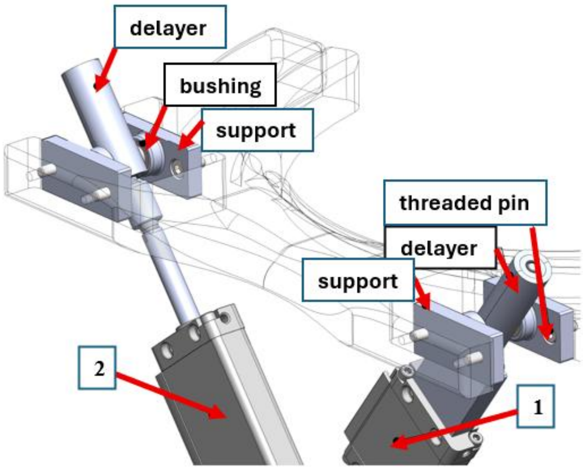

Figure 14a Main delayer assembly details.

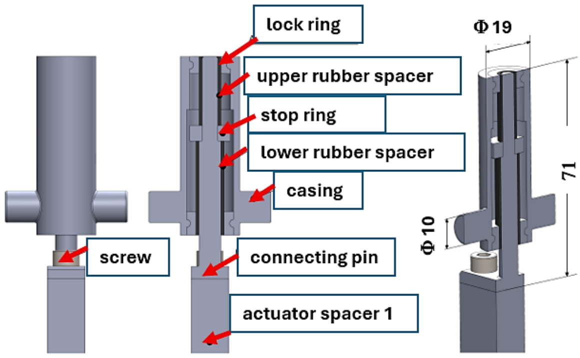

Figure 14b Delayer construction details.

Numerical simulation was performed with MATLAB Simulink software (version R2024a) and the following parameters; system mass, which depends on the mass of the human torso and the upper part of the exoskeleton, damping value, which is an intrinsic characteristic of the neoprene rubber, and the elastic propriety, which depends on the neoprene component’s geometry and shape. As can be seen from the simulation results in Figure 16, the C-frame tends to follow the actuator curve, initially with an oscillatory movement and slightly after the input signal, while at steady-state the two curves tend to coincide. The initial delay between the two signals matches the physiological delay between hip joint motion and spine joint motion, which is about 60 ms on average [14].

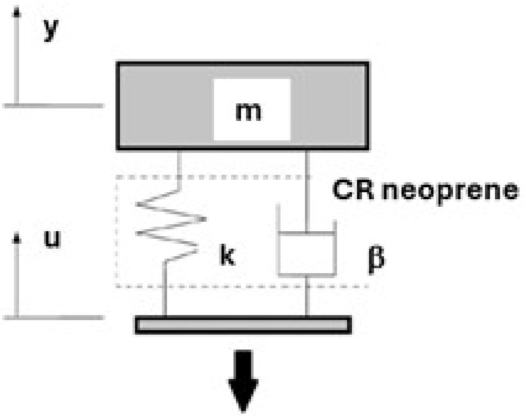

Figure 15a Delayer design model.

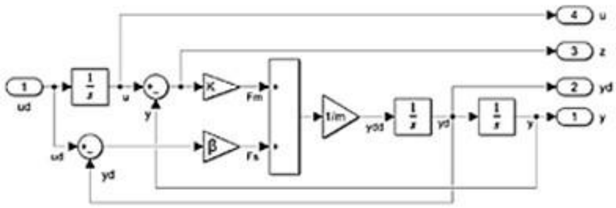

Figure 15b MATLAB Simulink model.

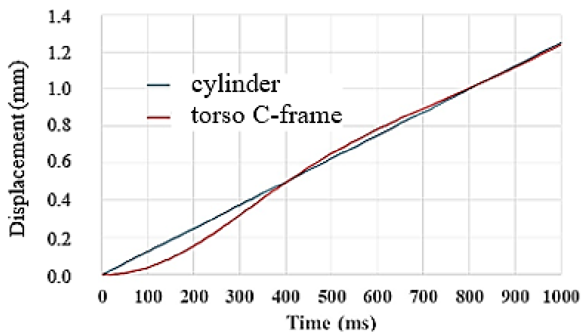

Figure 16 Selected simulation results.

Equation (1) clarifies the modelling process.

$$\ddot{y} = \frac{1}{m}[\beta(\dot{u} - \dot{y}) + k(u - y)] \rightarrow \int \rightarrow \dot{y} \rightarrow \int \rightarrow y \quad (1)$$

9 LOADS ON THE WEARER'S BODY

To better understand the interaction between the exoskeleton and the wearer, the forces exerted by the device on the wearer's body were studied under various trunk flexion angles and in the extreme and unrealistic condition in which the body acted on by the exoskeleton is considered to be inert. In reality, the body and exoskeleton are two autonomous active systems that must always move in perfect synchrony and never in opposition. Consequently, the forces exerted by the device on the body are actually lower than those calculated here. Figure 17 shows the action of each actuator (yellow) during exoskeleton operation, with their components (red) along the wearer's back and perpendicular to the wearer's body. The blue arrow indicates trunk movement. Analysis addressed only the actuator actions and their effects (difference or sum components) on the wearer's body, which was considered to be rigid and stationary.In reality, the body moves under its own muscle power in synchrony with the exoskeleton, which provides only an auxiliary torque. Again, the exoskeleton forces perceived by the wearer are actually much lower than the values obtained here.

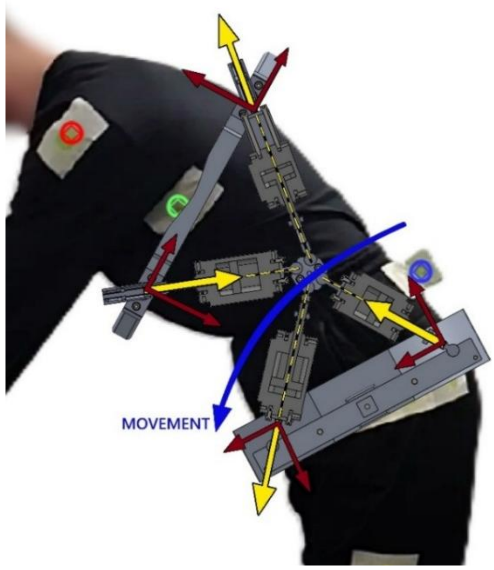

Figure 17 Details of the actuator forces along and perpendicular to the wearer's body.

Table III shows the forces exchanged between the exoskeleton and the wearer at supply pressures of 2 bar and 5 bar.

Table III - Exoskeleton forces on the wearer's body.

FORCES ON THE WEARER'S BODY		
Type	Supply pressure (bar)	Average maximum value (N)
Perpendicular pelvis (traction and compression)	5	560
	2	224
Perpendicular thoracic (traction and compression)	5	604
	2	242
Tangent to the spine (traction)	5	175
	2	70
Tangent to the abdomen (compression)	5	171
	2	68

Comparing these values with others from the literature [10,50], it was found that average forces on the wearer's body from a trunk exoskeleton vary in the literature from 120 to 150 N in traction, reducing disc compression by about 600 N during the flexion-extension cycle, with thoracic traction about 170 N and dorsal traction of 120 N. This analysis demonstrates that the prototype performance well under the conditions indicated above.

10 PRELIMINARY RISK ANALYSIS

To complete this stage of exoskeleton design, it is necessary to analyze the potential risks that may arise from the use of the exoskeleton before proceeding to address the purely technical aspects. Risk analysis for an industrial exoskeleton is carried out for several fundamental reasons, with the common goal of ensuring wearer safety and the device's effectiveness in an actual work setting [50]. These considerations are of paramount importance, as the exoskeleton is a machine that works in close contact with the wearer, meaning that safety standards must be particularly high to prevent problems that could jeopardize the wearer's health [51] [42].
Performing a risk analysis of the prototype at this stage of the design and with an eye to future design is advisable, as what the danger scenarios and their technical causes might be can be understood in advance.By identifying these critical aspects, it is possible to take action during the design phase, with the aim of arriving, at the end of prototyping and testing, at a product whose technical and functional characteristics are such as to minimize dangers for the wearer, other users and the surrounding environment [51] [42]. The method employed for the risk analysis involves identifying the prototype's operating and geometric characteristics (Table IV), defining risk scenarios for exoskeleton use (Table V) and objectively assessing the most dangerous scenarios in order to limit and/or eliminate them though changes in the device's design. The Fine-Kinney method was used to assess these scenarios.

Table IV - Main exoskeleton characteristics.

EXOSKELETON	
Type	Active, pneumatically actuated
Components	Torso C-frame Hip bars Center plates Pneumatic actuators Delayers
Total mass	9.9 kg
Dimensions [mm]	400 x 175 x 351
Adaptability	> 5 pct man > 10 pct woman
Range of movement	Forward trunk flexion 0° - 70°
Max. torque assist	18.31 Nm - top actuators 13.08 Nm - bottom actuators

Table V - Main risk analysis considerations

Hazard Classes	**Type**
Mechanical hazard	Hazards resulting from moving components, pinch points and connections between components
Thermal Hazards	Hazards resulting from component overheating, friction between parts
Noise Hazards	Hazards resulting from harmful levels of noise
Vibration Hazards	Hazards resulting from vibrations transmitted to the wearer
Ergonomic Hazards	Hazards resulting from component misalignment and non-optimal design
Max. torque assist	18.31 Nm - top actuators 13.08 Nm - bottom actuators

The Fine-Kinney method [52] is a risk assessment methodology based on mathematical calculation whereby a numerical score is assigned to a hazardous situation so that all analyzed risk scenarios can be objectively ranked.
The method uses three dimensionless parameters: likelihood, or the probability that risk scenario will occur; exposure, or the frequency with which the wearer may be exposed to the hazardous situation; and the possible consequences of the risk scenario in question. The scenario's risk score is the product of these three independent parameters [52]. As shown in Figure 18, the results show that potential hazards chiefly arise from the physical and functional interaction between the device and the wearer. Future design work will thus center on providing protective bellows around the delayers and actuators to prevent injury, crushing, or pinching of clothing or skin. Further studies will also address the materials that can be used, structural optimization to improve the components' mechanical resistance/weight ratio, and improving ergonomics by eliminating sharp edges and protrusions.

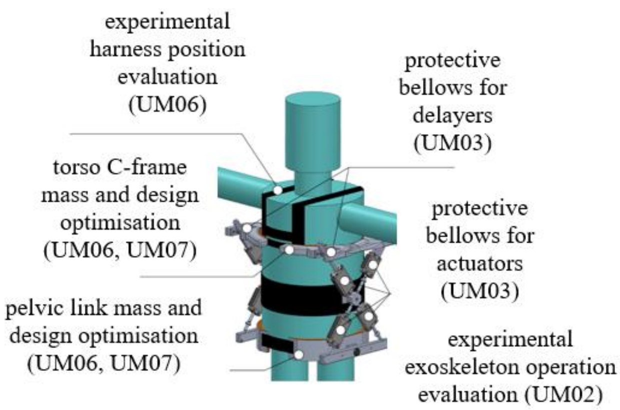

Figure 18 Summary of the risk analysis.

For a full evaluation of exoskeleton operation, moreover, a prototype must be constructed to test actual movement assistance.

11 WEARABILITY, WEIGHT AND SIZE

The analyses presented here indicate that the new trunk support exoskeleton is very versatile compared to earlier DIMEAS designs [31,32,36] or exoskeletons described in the literature [6,21], and offers good fit, low weight and compact dimensions Like earlier DIMEAS prototypes [36], it features multifunctional actuation units. To maintain the advantages of the first prototype, the exoskeleton's "X" configuration and the type and mounting direction of the actuators have been retained. Although the geometry remains unchanged, the overall height of the exoskeleton has been reduced from the first prototype's 360 mm to ensure that the device will fit a wide range of users (Figure 19a). Figures 19b and 19c illustrate the main dimensions and masses of two earlier industrial trunk exoskeleton prototypes designed at DIMEAS [31,36].

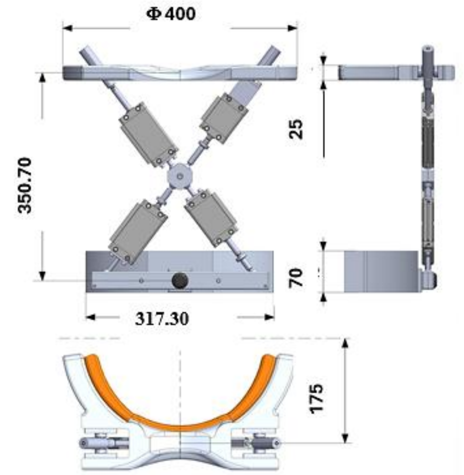

Figure 19a Main dimensions of the new exoskeleton structure (in mm).

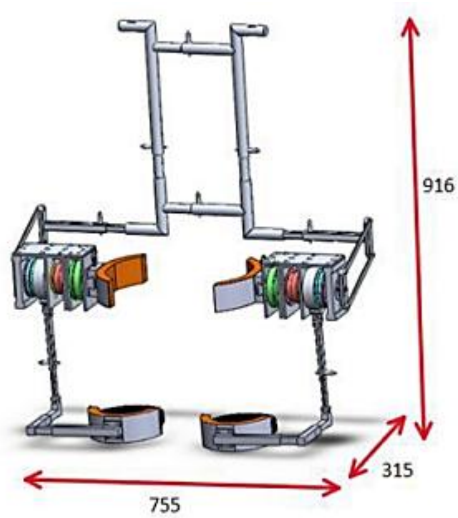

Figure 19b An earlier DIMEAS prototype with active multifunctional actuator units (dimensions in mm).

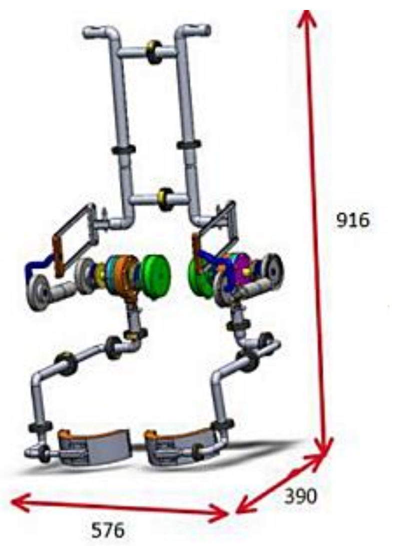

Figure 19c Optimization of the earlier DIMEAS prototype (dimensions in mm).

The advantages of the new prototype presented here are clear from a comparison with these data.

The fact that new prototype has no leg links is a particularly important advantage, as it reduces stress on the wearer, especially on the thigh, which is now free. It also permits a new geometry for the actuation units (which are always self-balancing thanks to their X-shaped arrangement and use of identical actuators), automatically ensures "legs-free" mode, and improves wearer comfort and fit. The masses of the earlier DIMEAS prototypes are respectively 5.6 kg (Figure 19b) and 5.3 kg (Figure 19c) for each actuation unit, while total mass is 9.2 kg (Figure 19b) and 8.9 kg (Figure 19c), including leg links and backframe.

Table VI shows the main materials currently constituting the prototype, which are still optimizable.

Figures 20a and 20b show the new version of the exoskeleton on a CAD model of a 95th percentile Italian male and on a volunteer.

Table VI – Main characteristics of the new prototype

Component	Material	Mass (kg)
Torso C-frame	Ergal 7075 - T6	1.90
Hip support	Ergal 7075 - T6	1.50
Hip bar	Ergal 7075 - T6	0.46
Center plate	Ergal 7075 - T6	0.06
Delayer	Delrin POM - C	0.11
Ball joint	Delrin POM - C	0.02
Spacer	Delrin POM - C	0.02
Screws	Titanium alloy	0.01
Standard pneumatic actuator	Aluminum alloy / high-alloy steel	0.87
Total mass, single actuation unit		4.95

In the future, it will be necessary to further optimize the overall weight, choosing similar technopolymer actuators and constructing the hip bar and torso C-frame using strong but lightweight polymer materials.

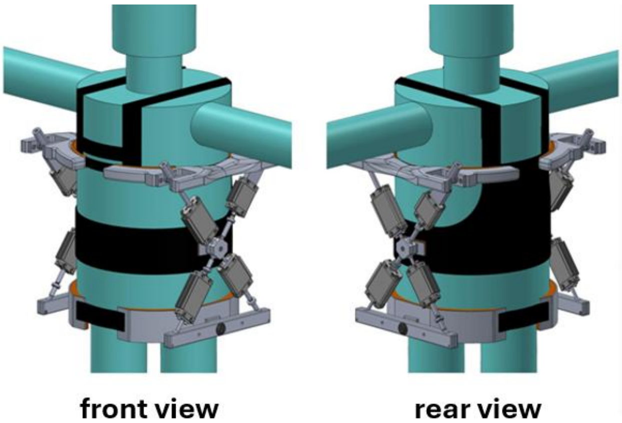

Figure 20a An example of the new exoskeleton worn by a 95%ile male.


Figure 20b CAD visualization of exoskeleton worn by a 50%ile Italian male volunteer.

11.1 MASSES AND BULK IN COMPARISON WITH THE LITERATURE

The study was then completed with a weight and size analysis of the entire exoskeleton. Comparing it with others (Table VII and Table VIII), this exoskeleton shows a good level of optimization. As shown in Table VIII, the main characteristics of the prototype presented here were compared with other exoskeletons now in production. The prototype's masses and dimensions compare very favorably, taking its great versatility into account (it assists trunk movement, supports the trunk when bent forward; can aid in lifting a load from floor level or elsewhere, etc.). In addition, the multifunctional actuation unit is designed for several exoskeleton operating modes (legs-free mode, percentage muscle torque delivery, peak muscle torque delivery, etc.). Obviously, in the future, some aspects of actuation unit and delayer design can be improved, and technopolymer actuators could be used. The exoskeleton's wearability could also be improved by reducing bulk and eliminating protruding angles. Furthermore, a textile vest will be designed to make the exoskeleton more comfortable to wear and assist its operation, for example by inserting flexible components whereby the stiffness of the vest/ exoskeleton interface can be adjusted as desired.

12 CONCLUSIONS

Based on experience gained in developing earlier exoskeletons, the study presented here led to the design of a trunk support exoskeleton with an non-conventional structure. Eliminating the leg links and backframe significantly simplifies the exoskeleton's structure without jeopardizing performance, and improves comfort and versatility while reducing weight and size as well as construction and maintenance costs.

The device was designed to fit wearers ranging from 5th percentile women to 95th percentile men without modifying the arrangement of the actuation units. This constitutes its innovative potential. Installing delayers between hip bar actuator movement and torso C-frame actuator movement reproduces the physiological hip joint and spine joint movement, greatly simplifying system geometry and avoiding the need for the additional components used in previous prototypes. The weight/dimensions of each actuation unit could be further optimized in the future, for example by using actuators of similar type but consisting of technopolymers. The analysis of the forces acting on the wearer's body, which is here assumed to be inert, provides the basis for the future development of human-machine interaction methods through instrumented experimental tests and simulation models. In any case, this preliminary analysis demonstrates the exoskeleton's effectiveness, while future analyses considering the motion of the wearer's body will show a further reduction in the forces applied to the body, a goal that will also be achieved by regulating the control pressure of each pneumatic cylinder. The study of the torque percentages during trunk flexion and the resulting pressure law will be fundamental in designing an appropriate control system. In the future, the authors plan to replace the pneumatic actuator with lightweight and space-saving electric actuation employing latest-generation electric actuators. The prototype provides multiple advantages. It has no leg links, which by definition means it is always in "leg-free" mode, and has fewer components, lower weight and costs, and is more compact. It is designed to fit a near-universal range of wearers, from 5th percentile women to 95th percentile men, while the actuation units' X-configuration makes them self-balancing when the wearer is standing upright. Minimal forces are exerted on the wearer's body during operation, which generally takes place at low pressures (2 or 3 bar) and can also be achieved with electric actuation.

Table VII – Comparison with similar devices

Ref.	Model	Producer	Main mechanical operation	Type of structure	Mass (kg)	Main points of contact with the body
[51]	Active trunk	RoboMate	DC electric actuation; motorized hip axis; leg link	Rigid	11.0	Thigh; shoulders; back; hip
[53]	ATOUN MODEL A	Panasonic	DC electric actuation; motorized hip axis; leg link	Rigid	7.4	Thigh; hip
[54]	ATOUN MODEL Y	Panasonic	DC electric actuation; motorized hip axis; leg link; small backframe	Rigid	4.4	Thigh; shoulders; back; hip
[18]	CRAY X	German Bionic	DC electric actuation; motorized hip axis; leg link; small backframe	Rigid	7.0	Thigh; shoulders; back; hip
[55]	VEX	Hyundai	DC electric actuation; motorized hip axis; leg link; small backframe	Rigid	4.5	Thigh; shoulders; back; hip
[9,10]	JAPET W	Japet	DC electric actuation	Flexible	< 2.0	Lower back
	This DIMEAS exoskeleton	DIMEAS Politecnico of Turin	Pneumatic actuation	Flexible/rigid	9.9 (improvable in the future)	Hip; crotch; chest; shoulders

Table VIII – Main characteristics of the new DIMEAS trunk support exoskeleton

Type	Pneumatically actuated active trunk support exoskeleton
Characteristics	Structure with no leg links or backframe, respecting the physiological structure of the pelvis and spine
Range of Movement	Trunk flexion from 0° to 70°
Mass	4.95 kg per side; 9.9 kg overall
Dimensions	400 x 175 x 351 mm
Wearability	Fits wearers from 5%ile women to 95%ile men
Harness	Vest consisting of polymer fabric and foam with shoulder, chest, lower back and crotch straps
Main materials	Ergal 7075 – T6 and Delrin POM - C
Maximum hip torque assist	18.31 Nm (70% maximum muscle torque)
Maximum force perpendicular to the body	Pelvic area: 5 bar 560 N; 2 bar 224 N Torso area: 5 bar 604 N; 2 bar 242 N
Maximum traction/compression force on wearer	Along spine: 5 bar 175 N; 2 bar 70 N Abdomen: 5 bar 171 N; 2 bar 68 N
Future design changes to avoid danger scenarios	Design and mass optimization; design of protective casings for moving parts; possible experimental evaluation of exoskeleton operation and fit; further study of the textile vest and exoskeleton/wearer

Lastly, the exoskeleton is multifunctional, as it provides trunk support, assists in lifting loads, reduces effort when holding demanding postures, etc. The authors are already conducting experimental studies on pose estimation using AI tools on various healthy subjects, as well as optimizing the exoskeleton itself. Specifically, its design and fit have been improved, and a possible solution using small, latest-generation electric actuators is being evaluated. This will determine the best final geometry to minimize the prototype's weight and size. In the future a strategy useful to have a potential indicator of the mechanical efficiency of the device will be set by the authors and all these indications with some more optimizations and studies on this human body movement will be taken in consideration before the device final construction. In particular the effectiveness of a torso exoskeleton can be assessed in various ways, such as: muscle activity analysis (EMG) to measure lumbar support, postural biomechanics (flexion angles), subjective perception of comfort, and ergonomic risk indices (such as NIOSH or EAWS). Specifically, a kinematic and postural analysis, including simulations, could be performed on a healthy subject wearing the exoskeleton. This allows for range of motion (ROM) assessments, as a good device reduces lumbar torque without interfering with natural gait, flexion, or the execution of daily maneuvers in the workplace. A subjective assessment of comfort, fit, size, and weight of the device itself, as well as any constraints during specific movements, can also be performed, also using ergonomic risk indices

ACKNOWLEDGEMENTS

The authors would like to thank I. Pappada', C. Vigenti, A.C.A. Borello, L. Carchia, P.D Cairella, M. Autino, F. Gorraz and S. Biglia for their help during this study.

REFERENCES

[1] Fellag R., Guiatni M., Hamerlain M. and Achour N., Exoskeleton robust control using adaptive finite time homogeneous higher order sliding modes. *International Journal of Mechanics and Control*, Vol. 22, No. 2, pp. 95-106, 2021.

[2] Polygerinos P., Wang Z., Overvelde J.T.B., Galloway K.C., Wood R.J., Bertoldi K. and Walsh C.J., Modeling of soft fiber-reinforced bending actuators. *IEEE Transactions on Robotics*, Vol. 31, No. 3, pp. 778-789, 2015.

[3] Sanchez-Lopez C., Planning handwriting for a 2-dof planar robot arm. *International Journal of Mechanics and Control*, Vol. 25, No. 1, pp. 115-121, 2024.

[4] Petuya V., Macho E., Altuzarra O., Pinto C. and Hernández A., Educational software tools for the kinematic analysis of mechanisms. *Computer Applications in Engineering Education*, Vol. 22, No. 1, pp. 72-86, 2011.

[5] Abane, A., Guiatni, M., Ababou, N., Amine Alouane M. and Bouzid, Y., Mechatronics design and control of a transformed upper limb rehabilitation exoskeleton. *International Journal of Mechanics and Control*, Vol. 21, No. 1, pp. 75-90, 2020.

[6] Marcheschi S., Salsedo F., Fontana M. and Bergamasco M., Body extender: whole body exoskeleton for human power augmentation. *2011 IEEE International Conference on Robotics and Automation*, Shanghai China 9-13 May 2011, doi: 10.1109/ICRA.2011.598132, pp. 611-616, 2011.

[7] Toxiri S., Matthias B., Näf M.B., Lazzaroni M., Fernández J., Sposito M., Poliero T., Monica L., Anastasi S., Caldwell D.G. and Ortiz J., Back-Support Exoskeletons for Occupational Use: An Overview of Technological Advances and Trends. *IISE Transactions on Occupational Ergonomics and Human Factors*, Vol. 7, No. 3-4: Occupational Exoskeletons, pp. 237-249, 2019.

[8] Petrone G., D'Alessandro V. and Sanchez-Lopez C., Planning handwriting for a 2-dof planar robot arm. *International Journal of Mechanics and Control*, Vol. 25, No. 1, pp. 115-121, 2024.

[9] Moulart M., Olivier N., Giovanelli Y. and Marin F., Subjective assessment of a lumbar exoskeleton's impact on lower back pain in a real work situation. *Heliyon*, Vol. 8, e11420, 2022.

[10] Reimeir B., Calisti M., Mittermeier R., Ralfs L. and Weidner R., Effects of back-support exoskeletons with different functional mechanisms on trunk muscle activity and kinematics. *Wearable Technologies*, Vol. 4, e12-1-e12-18, 2023

[11] Yang X., Huang TH., Hu S.Y.H., Zhang S., Zhou X., Carriero A., Yue G. and Su H., Spine-Inspired Continuum Soft Exoskeleton for Stoop Lifting Assistance. In: *IEEE Robotics and Automation Letters*, Vol. 4, No. 4, pp. 4547-4554, 2019.

[12] Legaye J., The Sagittal Pelvic Thickness: A Determining Parameter for the Regulation of the Sagittal Spinopelvic Balance. *ISRN Anatomy*, Vol. 2013, pp. 1-9, 2013.

[13] Tafazzol A., Arjmand N., Shirazi-Adl A. and Parnianpour M., Lumbopelvic rhythm during forward and backward sagittal trunk rotations: Combined in vivo measurement with inertial tracking device and biomechanical modeling. *Clin Biomech (Bristol) Elsevier*, Vol. 29, No. 1, pp. 1-13, 2014.

[14] Thomas, James S. and Gibson, Gary E., Coordination and timing of spine and hip joints during full body reaching tasks. *Hum Mov Sci Elsevier*, Vol. 26, No. 1, pp.124-140, 2007.

[15] Shin S. and Yoo W., The effect of sagittal hip angle on lumbar and hip coordination and pelvic posterior shift during forward bending. *European Spine Journal*, Vol. 29, No. 7, pp. 438–445, 2020.

[16] Vazirian M., Van Dillen L. and Bazrgari B., Lumbopelvic rhythm during trunk motion in the sagittal plane: A review of the kinematic measurement methods and characterization approaches. *Physical Therapy and Rehabilitation*, Vol. 3, No. 1, pp. 1-5, 2016.

[17] Eula G., Gorraz F., Mazza L. and Raparelli T., An engineering study of the human pelvis using models and data from the literature. *International Journal of Mechanics and Control*, Vol. 26, pp. 43-54.
[18] https://www.germanbionic.com/.
[19] Kelly R.E., *Back Brace*, Patent No. 1,202,851, United States Patent Office, 1916.
[20] Ferguson D.L. and Batton L.M.N., *Torso assist Orthotic device*, US Patent No. 8,568,344 B2, 2013.
[21] Babcock M.A., *Personal upper body support device for lower back muscle assist*, US Patent No. 7,744,552 B1, 2010.
[22] https://www.ulsrobotics.com/en/h-col-130.html.
[23] https://www.hyundainews.com/en-us/releases/230.
[24] https://www.laevo-exoskeletons.com/en/flex,
[25] https://germanbionic.com/en/press-and-download-area/.
[26] https://www.auxivo.com/omnisuit.
[27] https:// www.wirobotics.com/ product/ productDetail/ avMTG3bD.
[28] https://as.virgo.co.jp/pro3-en.html.
[29] https://www.skelex.com/products.
[30] Toxiri S., *An active back-support exoskeleton to reduce spinal loads: actuation and control strategies*. Dissertation, IIT and University of Genova (Italy), Department of Advanced Robotics, January 2018, pp. 1-100, 2018.
[31] Raparelli T., Eula G., Mazza L., Ivanov A., Pietrafesa F., Mala R. and Pontin M., A preliminary prototype of an industrial exoskeleton for the operator's trunk support. *International Journal of Mechanics and Control*, Vol. 23, No. 2, pp. 37-52, 2022.
[32] Raparelli T., Eula G., Mazza L., Ivanov A., Pietrafesa F., Mala R. and Pontin M., The design of an innovative active exoskeleton prototype for industrial application with a pneumatic actuation. *International Journal of Mechanics and Control*, Vol. 23, No. 2, pp. 61-72, 2022.
[33] Belforte G. and Eula G., Design of an active-passive device for human ankle movement during functional magnetic resonance imaging analysis. *Proc. IMechE, Part H: Journal of Engineering in Medicine*, Vol. 226, No. 1, pp. 21-32, 2011.
[34] Belforte G., Eula G., Appendino S., Geminiani G.C., Zettin M. and Sacco K., Active orthosis for the motion neurological rehabilitation lower limbs, system comprising such Orthosis and process for operating such system. *EP 2 825 146 B1*, Patent of POLITECNICO DI TORINO, 2012.
[35] Belforte G., Raparelli T., Eula G., Sirolli S., Appendino S., Geminiani G.C., Geda E., Zettin M., Virgilio R. and Sacco K., Study and realisation of a preliminary control system for the active exoskeleton called P.I.G.R.O., suitable for unloaded robotic neurorehabilitation treatments, *International Journal of Mechanics and Control*, Vol. 22, No. 1, pp. 125-142, 2021.
[36] Raparelli T., Mazza L. and Eula G., Study concerning design and optimization of a multifunction actuation group for an industrial exoskeleton. *IFIT 2024 September 2024* Politecnico di Torino, Torino Italy, IFToMM Italy 2024, Volume II, MMS 164, Chapter 1, pp. 3-10, 2024.
[37] Belforte G., Eula G., Ivanov A., Raparelli T. and Sirolli S., Presentation of textile pneumatic muscle prototypes applied in an upper limb active suit experimental model. *The Journal of The Textile Institute*, Vol. 109, No. 6, pp. 757-766, 2018.
[38] Eula G., Modeling a subject wearing an industrial trunk support exoskeleton. *International Journal of Mechanics and Control*, Vol. 26, No. 1, pp. 103-118, 2025.
[39] Flat cylinders EZH/DZF/DZH - data sheet. Festo S.p.A
[40] UNI EN ISO 7250-1: Basic human body measurements for technological design - Part 1: Body measurement definitions and landmarks. Geneva, CH: International Organization for Standardization ISO, 2017
[41] UNI CEN ISO/TR 7250-2: Basic human body measurements for technological design - Part 2: Statistical summaries of body measurements from national population. Geneva, CH: International Organization for Standardization ISO, 2024
[42] UNI/TR 11959:2024-2: Sicurezza e salute nell'uso degli esoscheletri occupazionali orientati ad agevolare le attività lavorative. Milano, IT: Ente Nazionale Italiano di Unificazione, UNI, 2024.
[43] Herman I.P., *Physics of the Human Body*. 2nd Edition, Springer Verlag, pp. 1-980, 2016.
[44] https://opensourcephysics.github.io/tracker-website/ "Tracker Video Analysis and Modeling Tool."
[45] Node-Red, OpenJS Foundation & Contributors. url: https://nodered.org
[46] Teachable Machine, Google. url: https://teachablemachine.withgoogle.com/
[47] Winter D.A., *Biomechanics and motor control of human movement*, 4th edition. Waterloo, CA: Wiley, pp. 1-370, 2009.
[48] Davidovits P., *Physics in Biology and Medicine*. Complementary Science Series Academic Press Elsevier, 3rd Edition, pp. 1-328, 2008.
[49] Chung D.D.L., Review: Material for vibration damping. *J. of Materials Science*, Vol. 36, pp. 5733-5737, 2001.
[50] Qi K., Yin Z., Li C., Zhang J. and Son J., Effects of a lumbar exoskeleton that provides two traction forces on spinal loading and muscles. *Frontiers in Bioengineering and Biotechnology*, Vol. 13, pp. 1-12, 2025.
[51] Van der Vorm J., de Looze M., Hadziselimovic M. and Heiligensetzer. P., *Risk assessment of Robo-Mate, an exoskeleton for workers*. White Paper www.robo-mate.eu, RoboMate, May 2016, pp. 2-19, 2016.
[52] Kinney G.F, and Wiruth A.D., *Practical Risk Analysis for Safety Management*. Naval Weapons Center California, pp. 1-21, 1976.
[53] https://news.panasonic.com/global/topics/5202.
[54] https://news.panasonic.com/global/topics/5214.
[55] https://robotics.hyundai.com/en/unveiled-robots/wearable/vex.do.

ISSN 1590-8844
International Journal of Mechanics and Control, Vol. 27, No. 01, 2026
https://doi.org/10.69076/jomac.2026.0001

UNCERTAINTY QUANTIFICATION IN RADIATIVE POWER SENSORS USING MONTE CARLO AND LATIN HYPERCUBE SAMPLING

Arash Safaei* Matteo Davide Lorenzo Dalla Vedova* Filippo Maggi**

* Department of Mechanical and Aerospace Engineering, Politecnico di Torino, Italy
** Department of Aerospace Science and Technology, Politecnico di Milano, Italy

ABSTRACT

This study introduces an experimental rig developed around a radiative heat flux sensor, designed to estimate the power emitted by a combustion flame over time. The system is built around a radiative heat flux sensor composed of a thermally responsive metallic disk, directly exposed to the flame's radiation and instrumented with a surface-mounted thermocouple. The temporal evolution of the disk's temperature, recorded during exposure, allows for the indirect estimation of key thermophysical properties of the source, such as radiative power density and its variation over time. This approach aims to provide a fast, minimally intrusive, and repeatable method for quantifying heat release in harsh thermal environments. To assess the reliability of the measurement chain and understand how input uncertainties propagate through the system, a probabilistic analysis is carried out using both Monte Carlo and Latin Hypercube Sampling (LHS) methods. These techniques were applied to account for variability in key parameters, such as disk's thermal properties and the boundary conditions of the system. The comparison between Monte Carlo and LHS highlights not only the sensitivity of the system to each input, but also the advantages of stratified sampling in terms of computational efficiency and convergence behaviour. The integration of this experimental rig with a robust uncertainty quantification approach results in a practical and scalable framework for the thermal characterization of radiative sources. This can be particularly valuable in aerospace applications involving solid propulsion systems [1], where flame behaviour and thermal loads play a central role in both performance and structural design considerations.

Keywords: Radiative Heat Flux Sensor, Uncertainty, Latin Hypercube Sampling, Monte Carlo Simulation, Sensitivity Analysis

1 INTRODUCTION

The Monte Carlo Method (MCM) is a numerical approach that estimates the probability distribution of a quantity of interest when one or more of the inputs governing it are affected by randomness. Its rationale stems from the fact that, when several uncertain inputs interact, the resulting distribution of the output can rarely be obtained in closed form. The method therefore proceeds by repeated random sampling: each uncertain input is assigned a value drawn at random from its probability distribution, the model is evaluated, and the corresponding output is stored.

Contact author: Arash Safaei[1]

[1] C.so Duca degli Abruzzi 24, 10129, Turin, Italy.
E-mail: arash.safaei@polito.it

By iterating this operation many times, a population of output values is progressively built, from which statistical descriptors such as the mean and the standard deviation can be estimated. The continuous growth of the computational resources available, even on ordinary personal computers, has made it practical to propagate uncertainty directly through Monte Carlo simulation, also when the output depends on many variables. The technique is by no means restricted to simple analytical expressions, since it applies equally well to involved data-reduction formulas or to the numerical solution of complex simulation models [2-4]. A closely related technique, frequently employed alongside Monte Carlo simulations, is Latin Hypercube Sampling (LHS) [5]. LHS pursues the same goal of propagating input uncertainty to the output, but it organises the sampling differently. Rather than drawing values in a fully random fashion, the domain of every uncertain input is partitioned into intervals of equal probability, and exactly one sample is extracted from each of them following a stratified scheme [6]. In this way the whole range of each variable is covered more evenly, which typically translates into quicker convergence and a lower computational cost for an equal number of model evaluations [7]. The method proves especially convenient whenever the number of runs must remain small because of time or resource limitations, while still yielding accuracy comparable to standard Monte Carlo in the estimation of statistical indicators such as the mean and the variance. In the following sections, the general approach for the MCM and LHS will be presented for uncertainty propagation along with the illustration technique. The whole discussion is adapted to the experimental tests carried out in the laboratory, in particular on the variables involved and on the output function.

2 DESCRIPTION OF THE METHOD

The objective of the presented experimental setup is to provide a non-intrusive and efficient technique for the measurement of the power flow emitted by the flame and temperature distribution along its length. This is not possible simply by using a thermocouple inserted inside the propellant or even inserted at different heights inside the body of the flame itself. The high temperatures reached by the flame released (up to orders of 2700 ÷ 3300 °C and more for certain propellant compositions) do not allow the direct use of thermocouples, since the most resistant existing type of thermocouple (based on Tungsten and Rhenium, type W3) detects temperatures up to 2310 °C [8], therefore subject to possible breakage if directly inserted in the flame, which would lead to misleading measurements. Not even the direct use of an optical pyrometer pointed against the surface of the flame can allow the detection of its temperature, since even the most sophisticated pyrometer on the available market does not exceed the ceiling of 2000 ÷ 2200 °C of measured temperature. These limitations are overcome thanks to the introduction of a sensitive element, through which the power flow and flame temperature are measured indirectly, by means of energy balances and heat exchanges, as reported schematically in Figure 1.

This sensitive disc is sized based on the imposed physics of the problem and the instrumental limitations of the experimental setup presented. this sensitive element represents a key point in the detection of the main variables measured under examination. Despite its importance and specific sizing in the presented rig, this disc can be adapted and resized in any situation and configuration other than that treated in the companion experimental work [9-10], thus making this method adaptable and valid, guaranteeing a robust system.

2.1 PROBLEM SETUP

In this section are presented the physical and mathematical considerations adopted for the setup of the problem. With reference to Fig. 1, the temperatures shown are to be considered as referring to the section of the component under examination, which is the sensitive disc. The $T_{thermo,disc}$ refers to the temperature detected by the thermocouple, in correspondence with the section of the disc, which is not facing the flame, while the $T_{element}$ is the average temperature of the sensitive disc. Since the disc has two faces, one facing the flame and one facing the thermocouple, these have different temperatures, therefore they are calculated on each face. The $T_{thermo,alumina}$ represents the temperature measured by a further thermocouple resting on the circular crown of the section of the alumina tube facing the flame. This temperature measurement appears necessary since it is not possible to calculate a priori the heat losses along the alumina tube, since the T_{flame} is an unknown of the problem. It is necessary therefore to know the temperature at the ends of the alumina tube to assess the losses along this path. As far as concerns the T_{flame}, this value is not to be considered as an average or indicative temperature of the entire flame. Since the designed observation system measures the amount of heat released by the lower portion of the flame (which starts from the surface of the propellant), up to the highest portion (the maximum height reached by the flame), this T_{flame} is to be considered as a real temperature distribution along the entire body of the flame, therefore as a local temperature measured along the entire height of the flame over time, constituting a spatial mapping of the flame temperature.

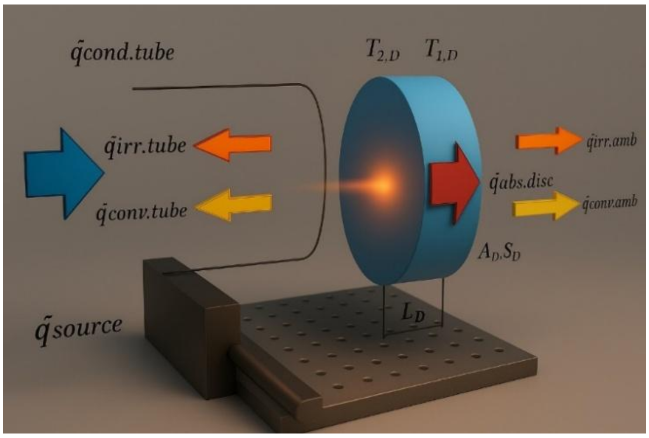

Figure 1 Energy balance of the sensitive disc during the heating process.

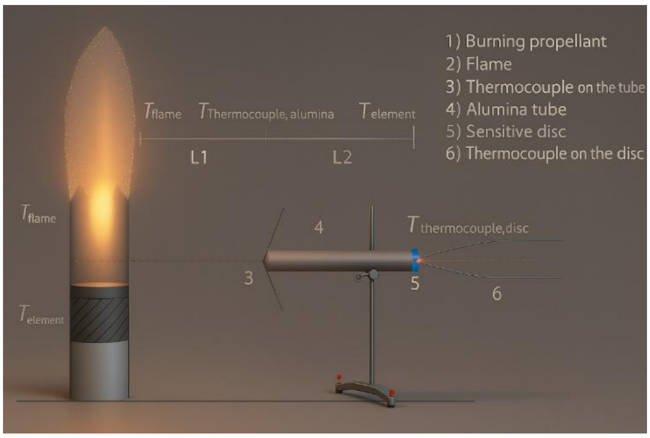

Figure 2 Schematic representation of the experimental implemented rig.

2.2 THERMAL BALANCE EQUATION

To apply the Monte Carlo and the Latin Hypercube Method to the global system that represents the physics of the sensitive disc during heating process, it is advisable to rewrite the equations that participate in achieving the desired output, to understand which and how many variables are affecting this output. The system of equation to be solved iteratively is summarized below:

$$
\begin{cases}
T_j^{i+1} = T_j^i + k_x \, \Delta t \, \dfrac{\left(T_{j+1}^i - 2T_j^i + T_{j-1}^i\right)}{\Delta x^2} \\
T_1^{i+1} = T_2^{i+1} + \Delta x \dfrac{\dot{q}_{tot,Disc}}{\lambda_D} \\
T_n^{i+1} = T_{n-1}^{i+1} - \Delta x \dfrac{\dot{q}_{irr,amb} + \dot{q}_{conv,amb}}{\lambda_D} \\
T_j^1 = T_{amb} \\
k_x = \dfrac{\lambda_D}{\rho_D c_{p,D}} \\
\dot{q}_{tot,disc}(t) = \dot{q}_{irr,amb}(t) + \dot{q}_{irr,tube}(t) + \dot{q}_{conv,amb}(t) \\
\dot{q}_{irr,amb}(t) = \varepsilon_D \sigma_0 \left|T_{1,D}^4(t) - T_{amb}^4\right| \\
\dot{q}_{irr,tube}(t) = \varepsilon_D \sigma_0 \left|T_{2,D}^4(t) - T_{amb}^4\right| \\
\dot{q}_{conv,amb}(t) = h_{conv,amb}(t)\left(T_{1,D}(t) - T_{amb}\right) \\
\dot{q}_{conv,tube}(t) = h_{conv,tube}(t)\left(T_{2,D}(t) - T_{fluid}\right) \\
h(t) = \dfrac{Nu(t) \cdot \lambda_{air}}{D_D} \\
Nu(t) = 0.59 \cdot Gr(t)^{0,25} \cdot Pr_{air}{}^{0,25} \\
Gr(t) = g \cdot \dfrac{1}{T_m(t)} \cdot D_D{}^3 \cdot \Delta T(t) \cdot \dfrac{1}{\nu_{air}{}^2} \\
T_D(t) = \dfrac{T_2^{i+1} + T_{n-1}^{i+1}}{2} \\
T_m(t) = \dfrac{T_D(t) + T_{amb}}{2} \\
\Delta T(t) = T_D(t) - T_{amb}
\end{cases}
\qquad (1)
$$

The system is made up of 16 equations, 11 of which are linearly independent (the equations containing on the left side the k_x, $\dot{q}_{tot,disc}$, $h(t)$, $T_D(t)$ and $\Delta T(t)$ depend on the others), and 11 unknowns, so it represents a closed system. The convective heat exchange between the disc and the surrounding air is described through a free-convection correlation, in which the Nusselt number is expressed as a function of the Grashof and Prandtl numbers [11-12].

The variables contributing to the variation of the disc temperature T_j^{i+1} are 11, the following ones: T_{amb}, T_{fluid}, λ_{air}, ε_D, ν_{air}, λ_D, Pr_{air}, r_D, ρ_D, $c_{p,D}$, Δx. The thermophysical and radiative properties involved, such as the thermal conductivity, the kinematic viscosity and the Prandtl number of air, together with the emissivity of the disc, are evaluated from reference data available in the literature [13]. Taking into consideration the following assumptions:

- $T_{amb} = T_{fluid}$; since the sensitive disc is supported by a tweezer a few centimeters away from the end of the alumina tube, therefore the temperature of the air around the hot face of the disc has to be considered as the ambient temperature.
- Due to stability reasons in the explicit finite-difference (Euler) scheme adopted to solve the governing PDEs [12], the term k_x does not participate in the first equation of the system of T_j^{i+1}, therefore the contribution of the variation of the variables ρ_D and $c_{p,D}$ is zero on the final variation of the output (the variable λ_D, although it appears in the equation of k_x, it participates in the variation of the output since this term appears in the denominator of the equations representing the boundary conditions T_1^{i+1} and T_n^{i+1}, while the terms ρ_D and $c_{p,D}$ appear only in the equation of k_x);
- $\Delta x = \frac{L_D}{N-1}$, where Δx is the spatial discretization of the disc thickness domain, depends on the number of nodes N chosen a priori and disc thickness L_D;

The number of variables is then reduced from 11 to 8, therefore the MCM and LHS analysis can be carried out on the remaining variables T_{amb}, λ_{air}, ε_D, ν_{air}, λ_D, Pr_{air}, r_D, L_D, to establish which of them contributes most to the variation of the final value.

3 PARETO ANALYSIS

Before applying the more computationally demanding sampling techniques, a preliminary Pareto Analysis is carried out to rank the input variables according to their actual influence on the output. The approach relies on the empirical 80/20 principle: when transposed to the present problem, it states that only a small subset of the input variables is responsible for the largest share of the output variability, whereas the remaining ones contribute marginally. By assessing how the perturbation of each variable propagates to the result, it is therefore possible to isolate the few dominant parameters and to discard those whose effect is negligible. This preliminary screening reduces the dimensionality of the problem and, as a direct consequence, the computational effort required by the subsequent Monte Carlo and Latin Hypercube analyses, which can then be focused only on the parameters that genuinely drive the uncertainty of the measurement chain [9]. The relative weight of each variable is quantified by means of the same governing system already reported in Eq. (1). Each of the eight retained variables T_{amb}, λ_{air}, ε_D and ν_{air}, among the others, is first perturbed individually by a fixed percentage, and the corresponding variation of the output, namely the power absorbed by the sensitive disc, is recorded. A final run is then performed in which all the variables are perturbed simultaneously by the same amount. The ratio between the variation induced by each single variable and the total variation produced in the combined run provides the contribution of that variable to the output. Sorting these contributions in descending order and accumulating them yields the Pareto diagram reported in Fig. 3. As shown in Fig. 3, the ambient temperature T_{amb} is by far the most influential parameter, accounting for about 27.3 % of the output variation, followed by the air thermal conductivity λ_{air} (24.3 %), the disc emissivity ε_D (18.8 %) and the air kinematic viscosity ν_{air} (12.4 %).

ISSN 1590-8844
International Journal of Mechanics and Control, Vol. 27, No. 01, 2026

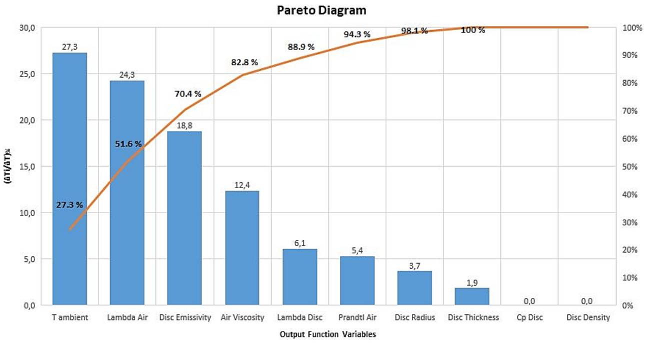

Figure 3 Pareto diagram for the sensitive disc heating problem.

Taken together, these four variables are responsible for roughly 82.8 % of the overall variability, thus exceeding the 80 % threshold associated with the Pareto principle. The remaining parameters λ_D, Pr_{air}, r_D and L_D contribute only a few percent each, while the disc specific heat $c_{p,D}$ and density ρ_D have a negligible effect, consistently with the assumptions introduced in the previous section. This outcome justifies restricting the subsequent uncertainty quantification to the four dominant variables T_{amb}, λ_{air}, ε_D and ν_{air}, achieving a substantial reduction of the computational cost without any appreciable loss of accuracy. This strategy is consistent with engineering modelling practices that prioritize the variables with the greatest impact on system performance [14].

4 MONTE CARLO METHOD

With reference to Fig. 4, the presented flowchart shows the steps involved in the uncertainty analysis carried out by the MCM. The sampling technique for a two variables function is displayed, but the methodology is general for functions of multiple variables, such as in the case of the system of equations reported before. By using the schematized approach for MCM propagation as the basis for the presented study, the assumed true value of each variable in the output result is taken as input. An appropriate probability distribution function is assumed for each error source. The random errors are usually assumed to come from a Gaussian distribution, but in case s comes from a very small sample, the t distribution with the appropriate degrees of freedom υ_s could be more appropriate. For the sake of simplicity, in Fig. 4 it is assumed that the random standard uncertainties for X and Y come from Gaussian distributions and that each variable has three elemental systematic standard uncertainties, one Gaussian, one triangular, and one rectangular. By means of an appropriate random number generator for each variable, random values in correspondence of random errors and elemental systematic errors are found. These individual error contributions are then summed and added to the true values of the variables to obtain the “measured” values. The result is then calculated thanks to these measured values, which corresponds to running the simulation once. This sampling process is repeated M times so as to obtain a distribution for the possible result values. It is important to point out that the primary goal of the MCM propagation technique is to find an estimation of the converged value for the standard deviation, s_{MCM}, of the distribution under examination.

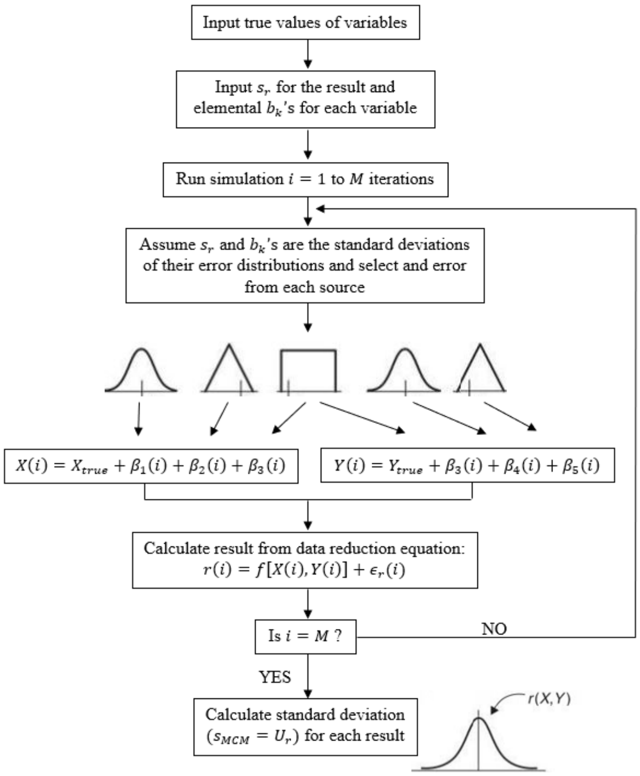

Figure 4 Schematic representation of MCM for uncertainty propagation.

A suitable value for M is found by periodically computing s_{MCM} during the MCM process and stopping the simulation as soon as a converged value of s_{MCM} is obtained. Keeping in mind that s_{MCM} is an estimation of the combined standard uncertainty of the result, u_r, it is not needed to have a perfectly converged value of s_{MCM} to have a reasonable estimate of u_r. It is sufficient to have a converged value of s_{MCM} within 1-5% to reach a good approximation. The level of convergence is a matter of judgment based on the cost of the sampling process and the application for u_r. As soon as a converged value of u_r is determined and assuming that the central limit theorem applies, the expanded uncertainty for the result at 95%, represented by the function $r(X,Y)$, corresponds to $U_r = 2\,u_r$. To reach a reasonable estimate of the converged value of s_{MCM}, the number of iterations required in the MCM can be reduced significantly by using special sampling techniques, such as Latin Hypercube Sampling Method, which will be described later. The systematic error β_3 for X and Y is the same, as it can be noted in Fig. 4, assuming that both the variables have a common and correlated systematic error. Furthermore, the random errors may be correlated because time-varying effects can affect the variables in the same manner, with their contributions to the error distribution represented by β_1, β_2, β_4 and β_5.

4.1 MCM UNCERTAINTY PROPAGATION

Considering the case of the sensible disc during the heating process and the Pareto Analysis presented in the previous section, the main variables contributing to the output (the power absorbed by the disc or its surface temperature) are,

from the most critical to the least: T_{amb}, λ_{air}, ε_D, ν_{air}, λ_D, Pr_{air}, r_D, L_D. As shown in Fig. 5, the nominal values of all these variables are to be taken as input to the MCM process. However, a function of 8 variables is extremely complicated to be managed and processed with a method such as that of Monte Carlo, given the high cost and computational time involved. The number of cycles necessary to calculate the distribution of the population of the output function is given by the product of the populations of the variables: therefore, in the examined case, since there are 8 variables, the number of cycles necessary for the calculation of output distribution is x^w, where x represents the population of the variables, decided by the user, and w the number of variables, 8 in this case. Furthermore, MCM converges only if the mean and standard deviation of the result reach a constant value after M iterations [15]. To calculate the convergence value of the mean and standard deviation of the output, it is necessary to make an average between the progressive values of the population of the function, to understand if enough samples have been used to arrive at a correct convergence.
The number of iterations required for the convergence clearly depends on the number of variables and their population, and it can be expressed, from the computational cost point of view, as a number of operations equal to the following expression:

$$n_{operations} = 2 \sum_{i=1}^{x^w} mean\ (z_1 : z_i) \tag{2}$$

Where z_i represents each element of the population and z represents the population of the output, whose size is given by the product of the populations of the variables on which the result depends on, as it follows:

$$size(z) = x_1 * \ldots * x_w \tag{3}$$

The multiplier 2 in front of the summation operator of Eq. 2 is because the convergence operation is performed on both the mean and the standard deviation of the output population z. Since performing the MCM for too many variables is demanding, thanks to the Pareto analysis performed on all the variables involved, it is convenient to reduce the number of variables from 8 to 4, by considering only the most critical variables on the output, thus reducing the computational cost and efficiency of the algorithm.
These variables are T_{amb}, λ_{air}, ε_D, ν_{air}, whose variation contributes for more than 80 % of the output variation, as a result of Pareto analysis; the variables λ_D, Pr_{air}, r_D, and L_D are therefore not considered in the MCM, since their influence on the output is negligible compared to the others. Standard uncertainties and associated error distributions are assumed for each variable. Error values can be randomly chosen from the distributions and added to the nominal values to get the measurement values for each variable.
To simplify the presentation, only statistical measurements error is considered for each variable distribution, neglecting the other possible source of error. The iteration process is continued until converged values of $u_{q_{abs,disc}}$ and $q_{abs,disc}$ are obtained.

If a Gaussian distribution is assumed for all the variables distribution, then the standard uncertainty inputs of the MCM for expanded uncertainties at a 95% level of confidence is expressed in the following way:

$$\left(u_{q_{abs,disc}}\right)_{MCM} = \sigma_{q_{abs,disc}} \tag{4}$$

or

$$\left(\frac{U_{q_{abs,disc}}}{q_{abs,disc}}\right)_{MCM} = \left(\frac{2u_{q_{abs,disc}}}{q_{abs,disc}}\right)_{MCM} \tag{5}$$

Where $\sigma_{q_{source}}$ represents the standard deviation of the output $q_{abs,disc}$, while the multiplier coefficient 2 refers to the 95% level of confidence of the Gaussian distribution ($\mu \pm 2\sigma$ represents the 95% of the Gaussian distribution population of mean value μ and standard deviation σ).

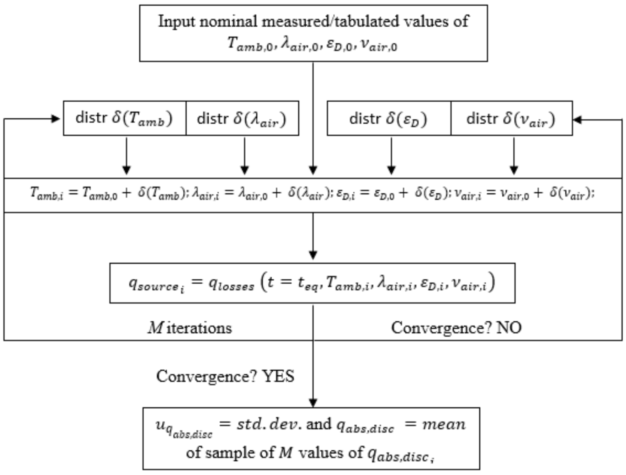

Figure 5 Schematic flowchart of MCM for the sensible disc heating problem.

The fully converged values of power absorbed by the sensitive disc and its standard deviation are reported below along with their corresponding plots, in relation to the different power levels set in the laser beam during the experimental tests, by means of MCM.

4.1.1 Incident Laser Power: 2.40 W

$$\left(q_{abs,disc}\right)_{MCM} = 0.0124\ W \tag{6}$$

$$\left(u_{q_{abs,disc}}\right)_{MCM} = 0.00112\ W \tag{7}$$

$$\left(\frac{U_{q_{source}}}{q_{abs,disc}}\right)_{MCM} = \left(\frac{2u_{q_{source}}}{q_{abs,disc}}\right)_{MCM} = 18.06\ \% \tag{8}$$

The convergence of the mean value of the power absorbed $q_{abs,disc}$ and of the combined standard uncertainty $u_{q_{abs,disc}}$ in this MCM case is shown in Eqs. 7 and 8. The converged value of $u_{q_{abs,disc}}$ is reached after approximately 500.000 cycles.

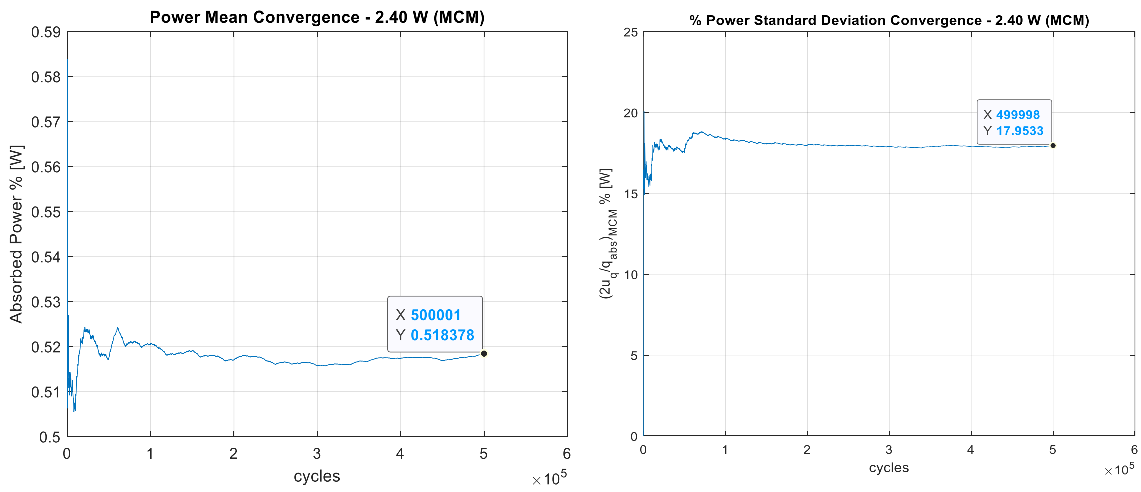

Figure 6 Convergence study of Power Mean absorbed (on the left) and Standard Deviation (on the right) in case of 2.40 W nominal laser power with MCM.

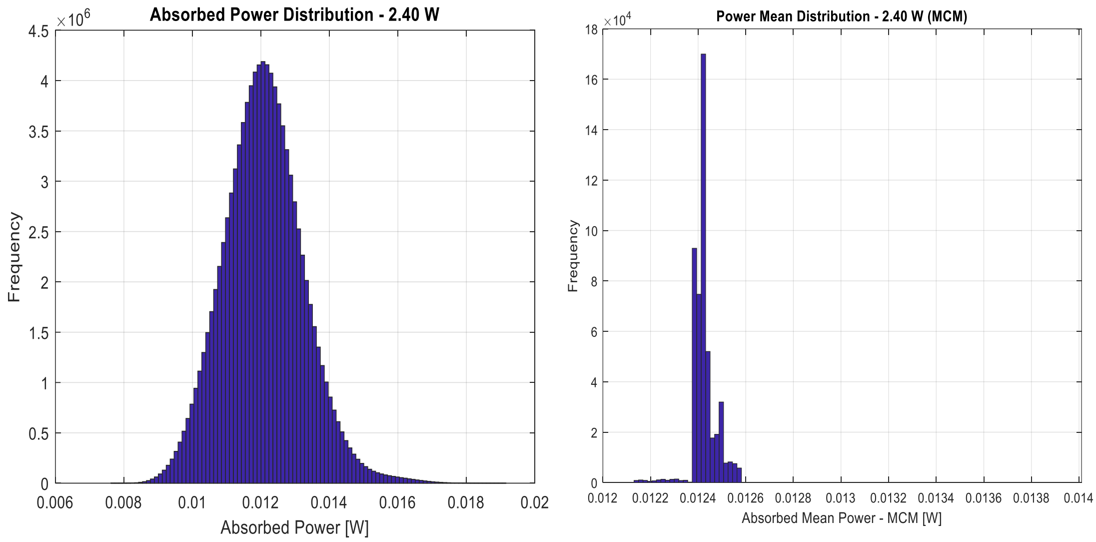

Figure 6 Output population distribution before (on the left) and after (on the right) convergence.

It can be proved that after 100.000 cycles this value has converged to within about 5% and by 500.000 iterations to withing less than 1% of the fully converged value.

By comparing the fully converged value of the absorbed power flow in Eq. 6 with the one calculated during the calibration test ($q_{abs,disc} = 0.0122\ W$), the difference in percentage between the two mean values amounts to 1.6%, thus showing a high estimate accuracy in the MCM.

In Fig. 7 it is shown the population distribution of the output $\left(q_{abs,disc}\right)_{MCM}$, given by the product of the populations of the 4 critical variables chosen for the MCM. A population of 100 samples is chosen for each of the 4 variables; therefore, the population of the output is represented by 100^4 samples, a sufficiently large population on which the progressive average has been performed needed for the convergence study.

4.1.2 Incident Laser Power: 3.75 W

$$\left(q_{abs,disc}\right)_{MCM} = 0.0173\ W \tag{9}$$

$$\left(u_{q_{abs,disc}}\right)_{MCM} = 0.00134\ W \tag{10}$$

$$\left(\frac{U_{q_{source}}}{q_{abs,disc}}\right)_{MCM} = \left(\frac{2u_{q_{source}}}{q_{abs,disc}}\right)_{MCM} = 15.49\ \% \tag{11}$$

In this second case, the convergence of the mean value of the power absorbed $q_{abs,disc}$ and of the combined standard uncertainty $u_{q_{abs,disc}}$ is shown in Eq. 9 and 10. The converged value of $u_{q_{abs,disc}}$ is reached after approximately 500.000 iterations.

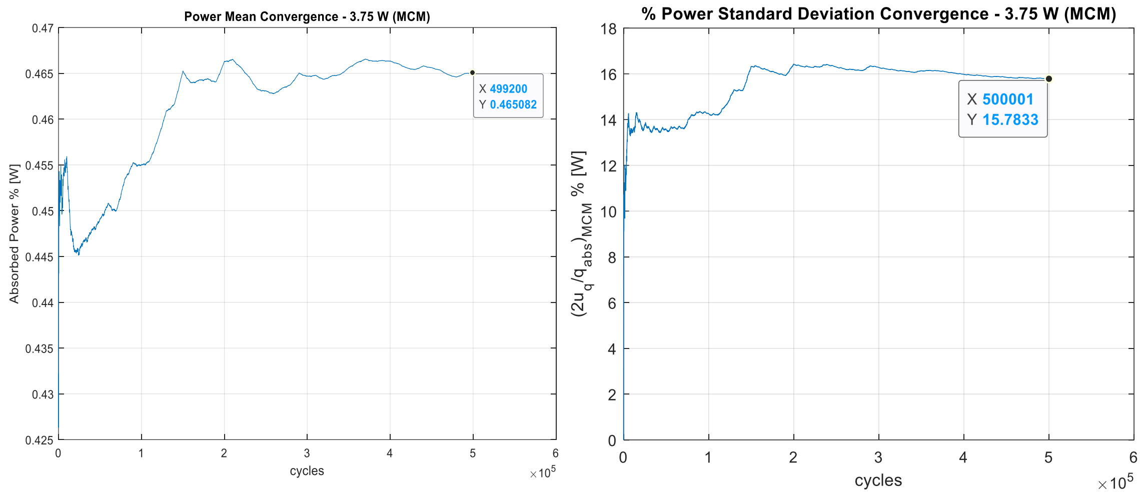

Figure 8 Convergence study of Power Mean absorbed (on the left) and Standard Deviation (on the right) in case of 3.75 W nominal laser power with MCM.

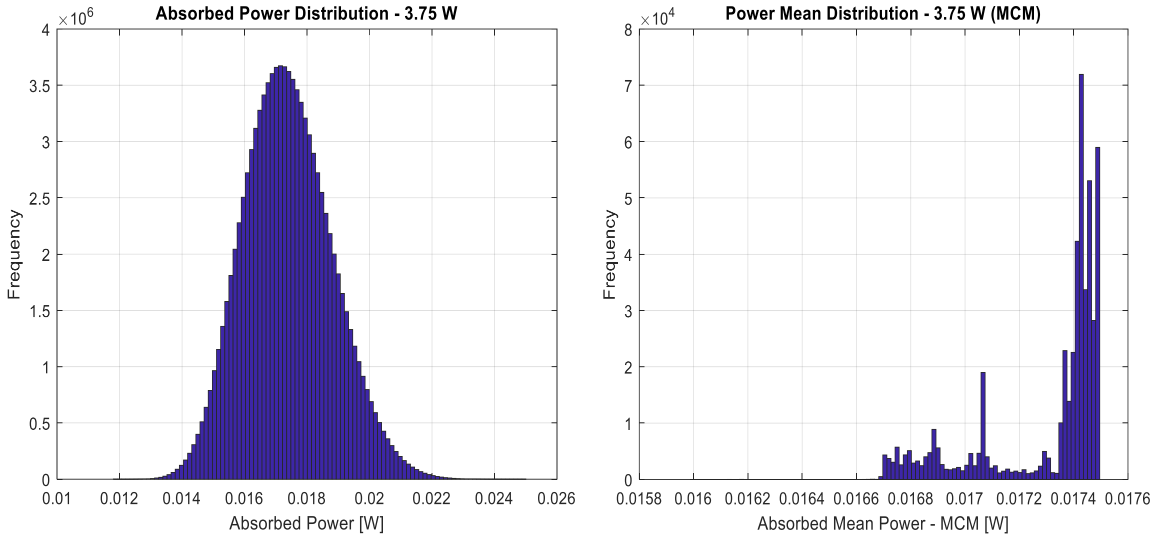

Figure 9 Output population distribution before (on the left) and after (on the right) convergence.

As far as concerns the convergence of the absorbed power shown in Eq. 11, it is visible that after 500.000 cycles, the value reached is not that corresponding to a full convergence, justified by the oscillation of the curve in the final part of the curve. This means that to achieve complete convergence, a larger population as regards the starting variables would have been necessary (going from 100 samples to 150 for example).
This value is considered acceptable due to the high computational costs, also because the value of power absorbed by the disc reached with 500.000 cycles is in line with the values measured during the experimental tests.
By comparing this converged value of the absorbed power in Eq. 9 with the one calculated during the calibration test ($q_{abs,disc} = 0.0160\ W$), the difference in percentage between the two mean values amounts to 7.5 %, showing a modest accuracy in the MCM. From the computational point of view, referring to Eq. 2, it appears that the number of operations necessary to reach convergence in the case of a population of 100^4 samples, is equal to about 10^{16} arithmetic mean operation calculations, an order of magnitude that is obtained by summing the numbers from 1 to 100^4, multiplied by 2.
Such several operations would require computing power that goes far beyond the power of an ordinary computer.
For this reason, to reduce the number of calculations, the progressive average operation is carried out only on a fraction of the available population.
Due to this computational simplification, the histogram representing the population distribution of the output at the end of convergence with MCM is notched and not fully bell-shaped like the Gaussian curve which represents the same population distribution before carrying out the MCM, as can be seen in Fig. 9.

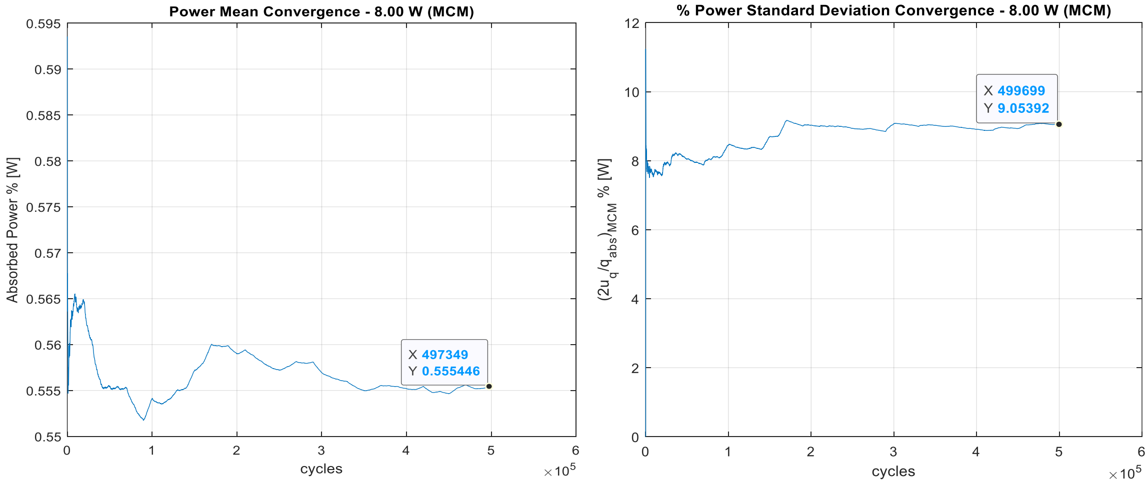

Figure 10 Convergence study of Power Mean absorbed (on the left) and Standard Deviation (on the right) in case of 8.00 W nominal laser power with MCM.

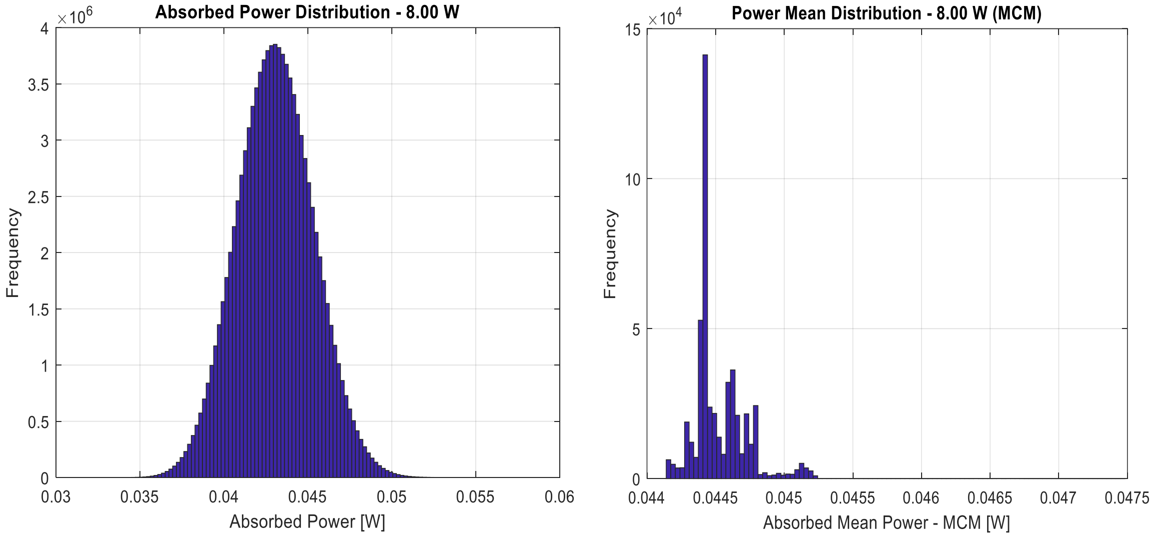

Figure 11 Output population distribution before (on the left) and after (on the right) convergence.

4.1.3 Incident Laser Power: 8.00 W

$$\left(q_{abs,disc}\right)_{MCM} = 0.0445\ W \tag{12}$$

$$\left(u_{q_{abs,disc}}\right)_{MCM} = 0.00194\ W \tag{13}$$

$$\left(\frac{U_{q_{source}}}{q_{abs,disc}}\right)_{MCM} = \left(\frac{2u_{q_{source}}}{q_{abs,disc}}\right)_{MCM} = 8.72\ \% \tag{14}$$

The convergence of the mean value of the power flow absorbed $q_{abs,disc}$ and of the combined standard uncertainty $u_{q_{abs,disc}}$ in this MCM case is shown in Eq. 12 and 13. The converged value of $u_{\dot{q}_{abs,disc}}$ is reached after approximately 500.000 iterations.

Also in this case the curve of the absorbed power has not perfectly reached convergence but presents some oscillations around the final cycles. This indicates once again how a larger population can improve the speed and quality of convergence, with the drawback of increasing the number of calculations needed and the computational cost. By comparing the fully converged value of the absorbed power flow in Eq. 12 with the one calculated during the calibration test ($q_{abs,disc} = 0.0439\ W$), the difference in percentage between the two values amounts to 1.12 %, showing high accuracy in MCM with respect to the experimental measured value. Since the progressive average necessary to reach convergence is carried out on a fraction of the population and not overall, a certain number of cycles are necessary for the average to get closer to that characteristic of the entire population.

This is evident in the initial part of the curve of Fig. 10, which presents peaks and irregularities in the first 200.000 cycles, due to the dispersion of the data of that fraction of the population from which the iterations are started. Despite this dispersion of data and the reduced population for the study of convergence, the curve oscillates in the range of absorbed power of 0.550 ÷ 0.565 in terms of percentage, which already shows in the first cycles an excellent precision within which the value reached at full convergence falls. The converged value shown in Eq. 12 represents 0.555 % of the mean absorbed power, therefore even if the MCM iterations stop within the initial cycles in which the progressive curve oscillates, the error made in estimating the final converged value is only 2.70 %, showing an excellent accuracy with a reduction of population and computations. The convergence study by means of MCM in the cases examined during the experimental tests, at different power levels, is presented. If the uncertainties of the variables are relatively large or the physics of the problem is highly non-linear, as in this case, the distribution of Monte Carlo results can be asymmetric, as can be barely seen in the converged distribution of Fig. 7. This implies that the result calculated using the nominal values of all the input variables will not coincide with the peak or mode (the most probable value), of the distribution of the MCM result. For these cases, calculating the standard deviation and assuming that the central limit theorem applies to obtain the expanded uncertainty will not necessarily be appropriate depending on the degree of asymmetry.

5 LATIN HYPERCUBE METHOD

Latin Hypercube Sampling (LHS) is commonly adopted to reduce the computational time when running Monte Carlo simulations. Previous investigations [16-18] have reported that a properly designed LHS can lower the processing time by as much as 50 percent with respect to a conventional Monte Carlo importance sampling. LHS is therefore more important when working with slow operating systems and software than when doing analysis on faster devices. Some have gone so far as to suggest that the modern computers available to almost any researcher have made LHS obsolete, but it is still widely used. Although it does not make as big a difference in analysis as it did in the days of slowly working on a computer system [19], it still leads to marginally more accurate results, in terms of true variability, given any amount of processing time. It is useful to understand how LHS can be applied to the problem studied in this work, and how this method can reduce the computation cost resulting from the numerous iterations with the MCM. To this end, LHS must be first classified about the dimension of the cumulative density function used:

- One-dimensional LHS involves dividing the cumulative density function into n equal partitions; then it must be chosen a random data point in each partition. For instance, let's consider a random sample with 100 data points. First, the cumulative density function is divided into 100 equal intervals. If the distribution starts at 0 and ends with k, the first data point would be selected from the interval between 0 and $k/100$. The second data point would then be selected from the interval $(k/100\,,2k/100)$, the third one from $(2k/100\,,3k/100)$, and so on. In each interval, one point is selected randomly, giving the user 100 different points.
- Two-dimensional LHS is not much more complicated and is usually performed with software. Assuming two variables, x_1 and x_2 are independent, the user follows the one-dimensional method to come up with one-dimensional sample for x_1 and x_2 separately. Once the two lists of samples are ready, they are combined randomly into two-dimensional pairs.
- For n-dimensional LHS the same method is adopted, by extending it to $x_1 \dots x_n$ variables.

Regarding the Monte Carlo method, it has mainly two disadvantages. First, it usually needs a very high number of simulations [20]. If the output quantity must be obtained by time-consuming numerical computations, the simulations can last a very long time, and the response surface method is not always usable. Second, it can happen that the generated random numbers of distribution function F, which serves for the creation of random numbers with nonstandard distributions, are not distributed sufficiently and regularly in the definition interval (0; 1). Sometimes, more numbers are generated in one region than in others, and the generated quantity has thus somewhat different distribution than demanded. This problem can appear especially if the output function depends on many input variables. LHS overcomes this drawback. The key difference is that LHS generates the values of F not by scattering random numbers in a disordered manner over the interval (0;1), but by assigning them prescribed values. The interval (0;1) is divided into several layers of equal width, and the x values are calculated via the inverse transformation F^{-1} for the F values corresponding to the center of each layer. With reasonably high number of layers (tens or hundreds), the created quantity x will have the proper probability distribution. This approach is called stratified sampling. If the output variable y depends on several input quantities $x_1 \dots x_n$, it is necessary that each quantity is assigned values of all layers and that the quantities and layers of individual variables are randomly combined, as previously described. This is done by randomly assigning the order numbers of layers to the individual input quantities, as shown in Fig. 12.

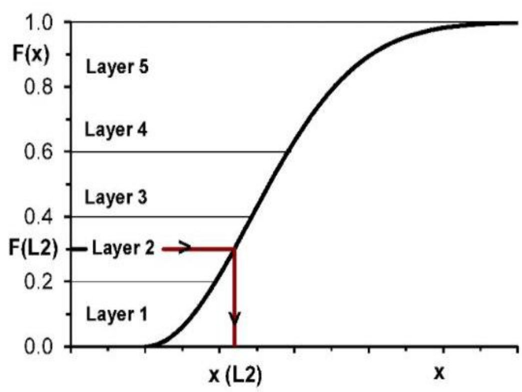

Figure 12 LHS randomly assign values to each layer.

Random numbers (RN)

Variable / Trial	X_1 RN	X_2 RN	X_3 RN	X_4 RN
1	0.56	0.12	0.72	0.13
2	0.25	0.40	0.84	0.60
3	0.83	0.05	0.21	0.55
4	0.17	0.62	0.03	0.99
5	0.30	0.70	0.61	0.73

Layer numbers for individual trials

Variable / Trial	X_1 layer	X_2 layer	X_3 layer	X_4 layer
1	2	4	2	5
2	4	3	1	3
3	1	5	4	4
4	5	2	5	1
5	3	1	3	2

Figure 13 LHS assignment of layers to individual variables and trials.

The application of LHS is illustrated on a case with four random quantities x_1, x_2, x_3 and x_4, as in the case of the four critical variables used for MCM (T_{amb}, λ_{air}, ε_D, v_{air}), and the definition interval of F divided into five layers, as shown in Fig. 13. Only five layers are used here for simplicity; usually, several tens of layers are used. In this case, the output variable y will be calculated for five combinations of the four input quantities. Thus, 5 × 4 = 20 random numbers with uniform distribution in interval (0; 1) are generated, as can be seen in the table on the left part of Fig. 13. Then, the layer numbers for variable x_1 for individual trials are assigned with respect to the order of random values related to x_1 ranked by size from the maximum to minimum. That is, layer no. 3, whose highest number is 0.83, for the first trial, layer no. 1 for the second, no. 5 for the third, no. 2 for the fourth, and no. 4 for the fifth, corresponding to the numbers 0.56 - 0.25 - 0.83 - 0.17 and 0.30 in the column for x_1. Similar operations are done for each variable. Thus, in the first trial, variables x_1, x_2, x_3 and x_4 are assigned the values corresponding to the second, fourth, second, and fifth layer of their distribution functions, respectively. Inverse probabilistic transformation F^{-1} is then used to determinate x_1 from $F_{1,1}$ and so on for the other variables, as can be seen in the table on the right part of Fig. 13. After these steps, the investigated quantity $y = y(x_1, x_2, x_3, x_4)$ is calculated five times. The obtained values y_1, y_2, y_3, y_4 and y_5 can be used for the determination of statistical properties of the output distribution, such as the mean and standard deviation [21].

In order to be able to implement the LHS method in the MATLAB simulation built for the analysis of experimental data, the $x = lhsnorm(mean, std.dev., n)$ command is used, which takes as input data the mean, standard deviation and the number of samples used to represent the population of the variable under consideration, the same values used in the case of the MCM method. Sampling and random operations performed on the cumulative density function of the distribution are therefore managed by this command.

The output distribution x is similar to a random sample from the multivariate normal distribution, but the marginal distribution of each column is adjusted so that its sample marginal distribution is close to its theoretical normal distribution.

5.1 LHS EXPERIMENTAL TESTS

The fully converged values of power absorbed by the sensitive disc and its standard deviation are the reported below along with their corresponding plots, in relation to the different power levels set in the laser beam during the experimental tests, by means of LHS.

5.1.1 Incident Laser Power: 2.40 W

$$(q_{abs,disc})_{LHS} = 0.0120\ W \tag{15}$$

$$\left(u_{q_{abs,disc}}\right)_{LHS} = 0.00110\ W \tag{16}$$

$$\left(\frac{U_{q_{source}}}{q_{abs,disc}}\right)_{LHS} = \left(\frac{2u_{q_{source}}}{q_{abs,disc}}\right)_{LHS} = 18.33\ \% \tag{17}$$

5.1.2 Incident Laser Power: 3.75 W

$$(q_{abs,disc})_{LHS} = 0.0175\ W \tag{18}$$

$$\left(u_{q_{abs,disc}}\right)_{LHS} = 0.00131\ W \tag{19}$$

$$\left(\frac{U_{q_{source}}}{q_{abs,disc}}\right)_{LHS} = \left(\frac{2u_{q_{source}}}{q_{abs,disc}}\right)_{LHS} = 14.97\ \% \tag{20}$$

5.1.3 Incident Laser Power: 8.00 W

$$(q_{abs,disc})_{LHS} = 0.0428\ W \tag{21}$$

$$\left(u_{q_{abs,disc}}\right)_{LHS} = 0.00201\ W \tag{22}$$

$$\left(\frac{U_{q_{source}}}{q_{abs,disc}}\right)_{LHS} = \left(\frac{2u_{q_{source}}}{q_{abs,disc}}\right)_{LHS} = 9.39\ \% \tag{23}$$

As can be seen by directly comparing the convergence graphs with the MCM and LHS method for all power levels analysed, convergence is much faster in the case of the LHS. With respect to the more than 500,000 cycles required by the MCM to get close to the convergence range, with LHS it only takes a few thousand cycles to achieve full convergence.

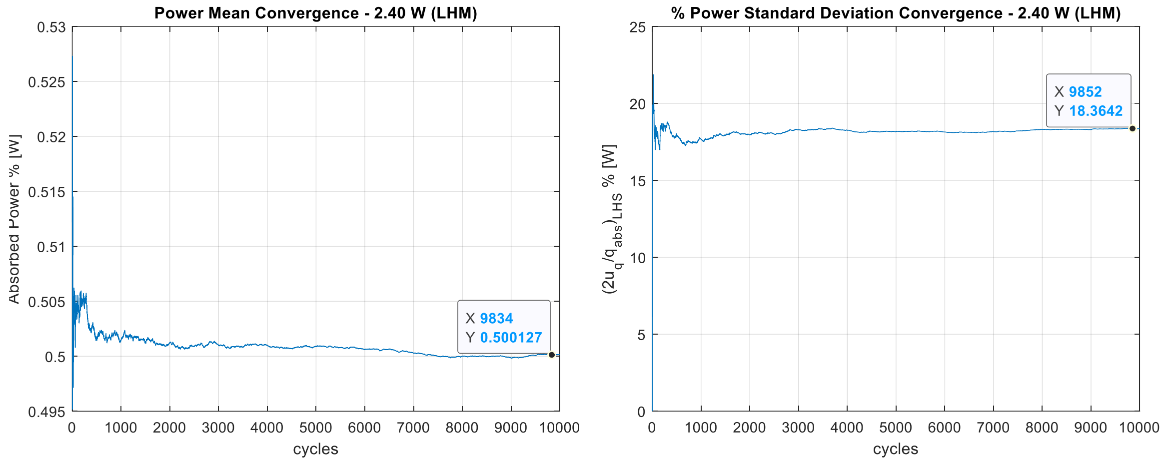

Figure 14 Convergence study of Power Mean absorbed (left) and Standard Deviation (right) in case of 2.40 W nominal laser power with LHS.

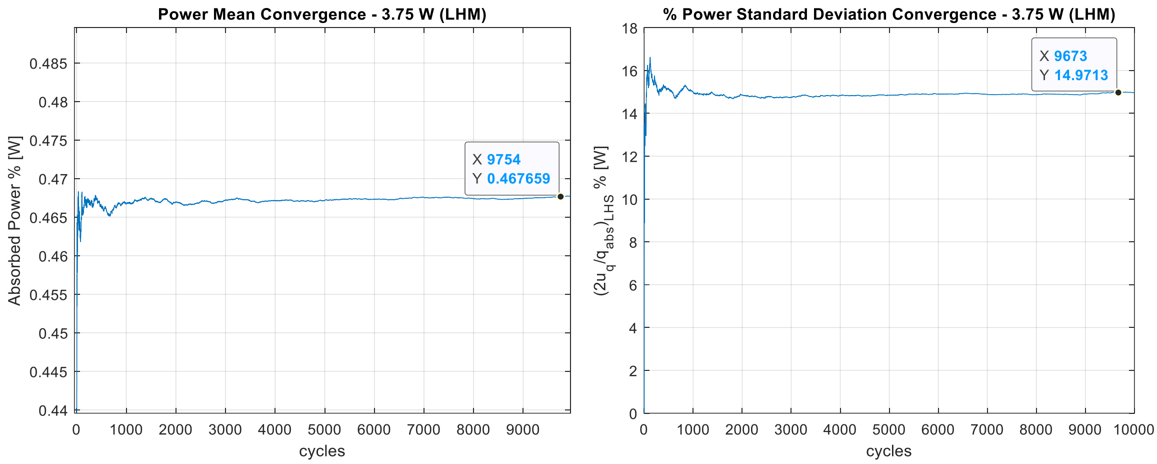

Figure 15 Convergence study of Power Mean absorbed (left) and Standard Deviation (right) in case of 3.75 W nominal laser power with LHS.

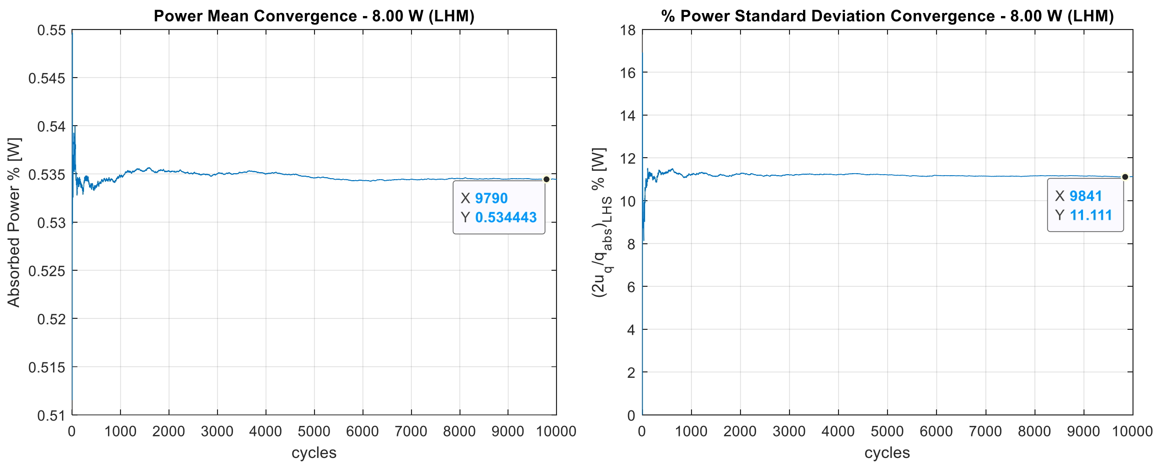

Figure 16 Convergence study of Power Mean absorbed (left) and Standard Deviation (right) in case of 8.00 W nominal laser power with LHS.

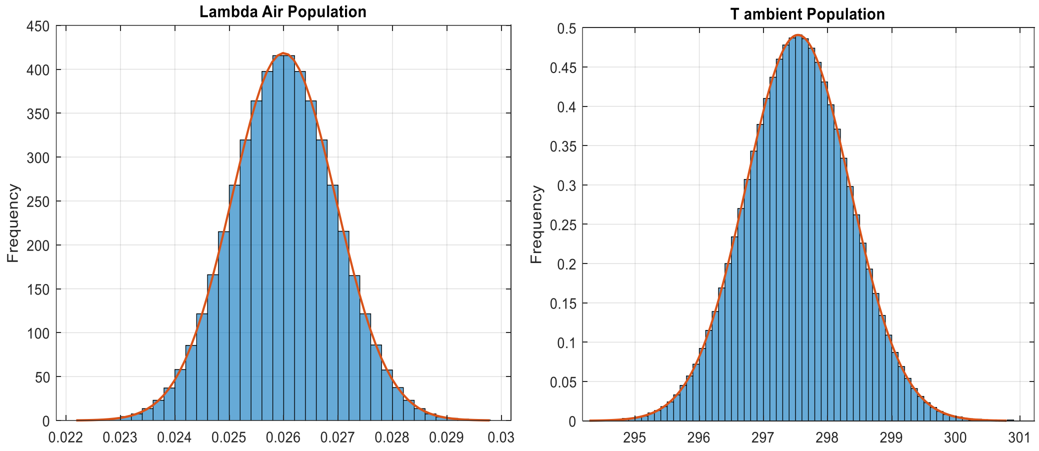

Figure 17 Population distribution of $\boldsymbol{\lambda_{air}}$ and $\boldsymbol{T_{amb}}$ made of 10.000 samples.

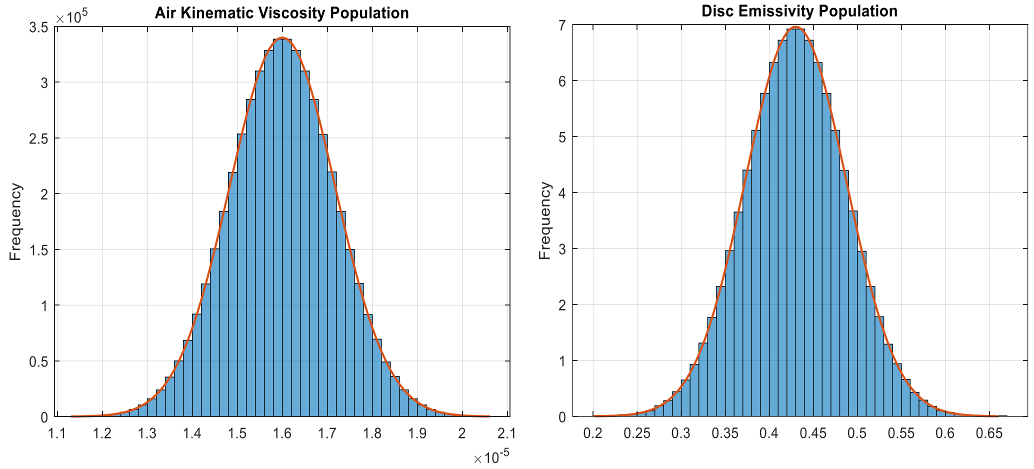

Figure 18 Population distribution of $\boldsymbol{\nu_{air}}$ and $\boldsymbol{\varepsilon_D}$ made of 10.000 samples.

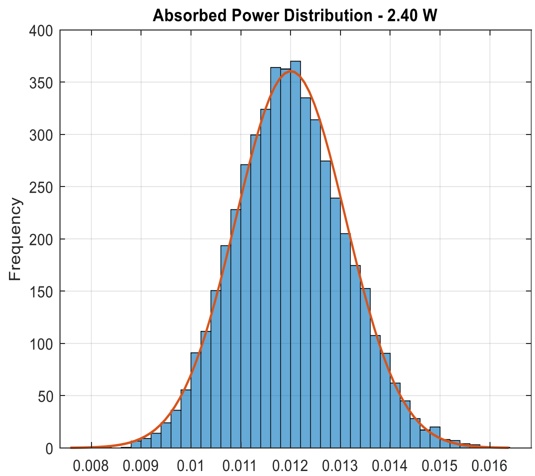

Figure 19 Population distribution of output made of 10.000 samples.

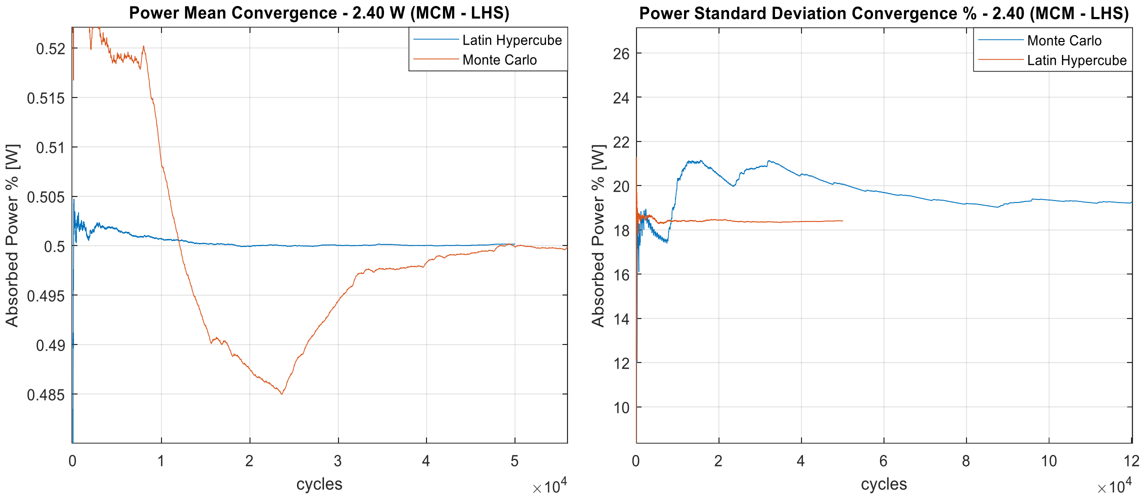

Figure 20 Convergence comparison of Power Mean absorbed (left) and Standard Deviation (right) in case of 2.40 W nominal laser power between MCM and LHS.

Table I - Comparison between MCM and LHS results

	$(q_{abs,disc})_{MCM}$	$(u_{q_{abs,disc}})_{MCM}$	$(q_{abs,disc})_{LHS}$	$(u_{q_{abs,disc}})_{LHS}$	Er_q %	Er_u %
2.40 W	0.0124 W	0.00112 W	0.0120 W	0.00110 W	3.22	1.78
3.75 W	0.0173 W	0.00134 W	0.0175 W	0.00131 W	1.14	2.23
8.00 W	0.0445 W	0.00194 W	0.0428 W	0.00201 W	3.82	3.48

From the plots it is clearly visible that after 2000 cycles the fully convergence value is almost reached, obtaining a value below 1% of the full output convergence. The power and low computational cost of the LHS is clearly remarkable compared to the MCM. Another positive point in favour of this last method used can be sort out in the high number of samples used to describe the population distribution of the input variables, 10.000 samples in the case of the LHS compared to only 100 of the MCM, ensuring greater homogeneity and regularity in the distribution of data in the respective variation domain. Finally, it is useful to point out the difference in the values obtained at convergence both as regards the average and standard deviation of the output, in the case of the MCM and LHS. The relative percentage error between the two methods is lower than 5 % regarding both the estimate of the mean and of the standard deviation of the power absorbed, guaranteeing an excellent match between MCM and LHS, as shown in Table I.

6 CONCLUSIONS

Thanks to the Monte Carlo and Latin Hypercube Method, the model provided a satisfying response regarding both the stability and the convergence of the output. Although the studied physical problem constituted a complicated multi-variable dependence system, it has been possible to reduce the complexity of the physics to a few sensitive parameters, by means of Pareto Analysis. In this way, it has been possible to separate the important and most influencing variables on the output, minimizing the computational cost. The results are compatible with literature data. The presented setup can be readily assembled and used to perform other tests with various power input and different sensitive disc samples. Thanks to the experimental confirmation and validation of the model, it is possible to extend the validity of the implemented line for the observation and study of a heat source other than that of the laser beam used during the experimental tests, such as the flame of a burning solid propellant. The ability and robustness of the presented implemented model to process the thermal response of the sensitive element with accuracy, particularly its power losses due to heating, can lead to a direct analysis of the heat flux emitted by a flame in space and time, providing a numerical power flux map never achieved in the past.

REFERENCES

[1] Favre S., Di Fede F., Brusa E., Delprete C., Innovative thermal management systems for fuel cell electric aircraft. *International Journal of Mechanics and Control*, Vol. 26, No. 01, pp. 159-183, 2025. https://dx.doi.org/10.69076/jomac.2025.0014

[2] International Organization for Standardization (ISO), *Guide to the Expression of Uncertainty in Measurement*. ISO, Geneva, Switzerland, 1993.

[3] Joint Committee for Guides in Metrology (JCGM), *Evaluation of Measurement Data – Supplement 1 to the Guide to the Expression of Uncertainty in Measurement – Propagation of Distributions Using a Monte Carlo Method*. JCGM 101:2008, Paris, France, 2008.

[4] Safaei A., Dalla Vedova M.D.L., Maggiore P., CFD-based design and optimization of a cryogenic piston valve for liquid hydrogen flow control. *International Journal of Mechanics and Control*, Vol. 26, No. 02, pp. 69-82, 2025. https://dx.doi.org/10.69076/jomac.2025.0026

[5] Helton J.C. and Davis F.J., Latin Hypercube Sampling and the Propagation of Uncertainty in Analysis of Complex Systems. *Reliability Engineering & System Safety*, Vol. 81, No. 1, pp. 23–69, 2003.

[6] Carnell R., *Latin Hypercube Sampling*. R Package Version 0.10, 2012.

[7] Stein M., Large Sample Properties of Simulations Using Latin Hypercube Sampling. *Technometrics*, Vol. 29, No. 2, pp. 143–151, 1987.

[8] Gayesco-WIKA, *Thermocouple Reference Guide*. Pasadena, CA, USA.

[9] Safaei A., Dalla Vedova M.D.L. and Maggi F., Power Flow Measurement Through a New Rig Based on a Sensitive Element and Irradiation. *16th Int. Conf. on Vibration Measurements by Laser and Noncontact Techniques. (AIVELA 2025)*. Ancona, Italy. Journal of Physics: Conference Series, Vol. 3179, No. 012004, 2026. DOI 10.1088/1742-6596/3179/1/012004

[10] Gjeta A., Hoxha A., Alcani M., Dorri A., Development of enhanced MATLAB-based thermodynamic cycle software: comprehensive analysis of gas cycles with polynomial specific heat dependence. *International Journal of Mechanics and Control*, Vol. 26, No. 02, pp. 3-10, 2025. https://doi.org/10.69076/jomac.2025.0019

[11] Churchill S.W. and Churchill R.U., A Comprehensive Correlating Equation for Heat and Component Transfer by Free Convection. *AIChE Journal*, Vol. 21, No. 3, pp. 604–606, 1975.

[12] Causon D.M. and Mingham C.G., *Introductory Finite Difference Methods for PDEs*. Ventus Publishing, 2010.

[13] Fluke Corporation, *Emissivity Values for Common Materials*. Process Instruments, Technical Reference Guide.

[14] Korytov M.S., Shcherbakov V.S., Kashapova I.E., Vibration protection system of constant acceleration of the operator's seat. *International Journal of Mechanics and Control*, Vol. 26, No. 01, pp. 213-219, 2025. https://doi.org/10.69076/jomac.2025.0016

[15] Glasserman P., Heidelberger P., Shahabuddin P. and Zajic T., Asymptotic Efficiency of Monte Carlo Estimators: Relative Error Versus Absolute Error. *Journal of Risk and Financial Management*, Vol. 8, No. 2, pp. 136–152, 2015.

[16] Olsson A., Sandberg G. and Dahlblom O., On Latin Hypercube Sampling for Structural Reliability Analysis. *Structural Safety*, Vol. 25, No. 1, pp. 47–68, 2003.

[17] Keramat M. and Kielbasa R., Modified Latin Hypercube Sampling Monte Carlo (MLHSMC) Estimation for Average Quality Index. *Analog Integrated Circuits and Signal Processing*, Vol. 19, No. 1, pp. 51–62, 1999.

[18] Kucherenko S., Albrecht D., Saltelli A. and Sobol' I.M., Exploring Multi-Dimensional Spaces: A Comparison of Latin Hypercube and Quasi Monte Carlo Sampling Techniques. *arXiv Preprint*, arXiv:1505.02350, 2015.

[19] Xin L., Numerical Methods for Engineering Design and Optimization: Latin Hypercube Sampling (LHS). *Technical Report*, January 2014.

[20] Papageorgiou A. and Traub J.F., Weak Convergence for Monte Carlo vs. Quasi Monte Carlo Methods in High Dimension. *Journal of Complexity*, Vol. 19, No. 3, pp. 332–351, 2003.

[21] Mencik J., Latin Hypercube Sampling. In: *Concise Reliability for Engineers*. Department of Mechanics, University of Pardubice, Czech Republic, 2016.

ISSN 1590-8844
International Journal of Mechanics and Control, Vol. 27, No. 01, 2026
https://doi.org/10.69076/jomac.2026.0002

INFLUENCE OF INFILL PATTERN ON THE MECHANICAL AND THERMAL PROPERTIES OF 3D-PRINTED PLA SAMPLES

Pawel Madejski* Isyna Izzal Muna* Tomasz Machniewicz**

*Department of Power Systems and Environmental Protection Facilities,
Faculty of Mechanical Engineering and Robotics, AGH University of Krakow, Krakow, Poland

**Department of Machine Design and Operation,
Faculty of Mechanical Engineering and Robotics, AGH University of Krakow, Krakow, Poland

ABSTRACT

Additive manufacturing (AM) technologies are increasingly applied in modern industry due to their capability to fabricate complex geometries while reducing material waste and production costs. Among these techniques, Fused Deposition Modelling (FDM) is widely used for producing polymer components with customized internal architectures. Such structures are employed in functional prototypes, lightweight load-bearing elements, and thermally exposed components where both mechanical strength and thermal performance are essential. This study presents an experimental investigation of the thermo-mechanical behaviour of 3D-printed polylactic acid (PLA) specimens manufactured using FDM. The influence of internal geometry was evaluated by comparing five infill patterns: cubic, line, triangular, octet, and quarter-cubic. Uniaxial tensile tests were performed to determine stress–strain characteristics, Young’s modulus, Poisson’s ratio, ultimate tensile strength, and strain at failure. The novelty of this work lies in the simultaneous analysis of mechanical response and temperature evolution using infrared thermography during tensile loading. Temperature distribution was continuously monitored, enabling identification of gradual thermal changes during elastic and plastic deformation, as well as rapid temperature increases preceding fracture. Additionally, thermal conductivity and thermal effusivity were measured for each infill configuration to better characterize the relationship between the internal architecture and the thermomechanical response.

Keywords: Fused Deposition Modelling; biodegradable PLA; tensile testing; thermal conductivity, thermal effusivity

1 INTRODUCTION

It is commonly assumed that maximizing the tensile strength of a 3D-printed part is key to improving its mechanical performance. However, this study presents a counterintuitive finding: a PLA specimen with lower tensile strength can offer superior energy absorption and delayed failure entirely due to its internal infill geometry.

Contact author: Pawel Madejski

Dept. of Power Systems and Environmental Protection Facilities, Faculty of Mechanical Engineering and Robotics, AGH University of Krakow, Al. Mickiewicza 30, 30-059 Krakow, Poland
E-mail: madejski@agh.edu.pl

Specifically, while exhibiting lower ultimate tensile strength than the Octet structure, showed significantly higher ductility and strain tolerance.
This result challenges conventional assumptions about that strength alone defines mechanical quality in additively manufactured parts and highlight the important role of internal structure in overall performance [1-3].
As additive manufacturing technologies, particularly Fused Deposition Modelling (FDM), gain traction for structural and thermomechanical applications, optimizing the internal architecture of printed parts has become increasingly important. Polylactic acid (PLA), a biodegradable thermoplastic favored for its processability and environmental compatibility, is widely used in FDM but is inherently semi-brittle. Its limited ductility often below 10% elongation at break, makes it sensitive to structural design parameters such as crystallinity, molecular orientation, and infill pattern [4, 5]. FDM is widely

recognized for its design flexibility, low cost, and ability to produce complex geometries. However, challenges such as weak interlayer bonding, anisotropic mechanical properties, and limited material selection hinder its adoption for functional end-use parts [6-10].

Studies highlight the impact of infill density, pattern, and orientation on mechanical properties and weight reduction. For instance, triangular infill patterns with optimized densities have demonstrated superior stiffness and reduced stress in UAV components [1, 2, 10]. Similarly, hexagonal infill patterns are effective for balancing strength and dimensional accuracy [11-14].

This study investigates the tensile performance of PLA specimens with five distinct infill topologies: Cubic, Quarter-Cubic, Lines, Octet, and Triangles. A total of 25 samples were printed on a MakerBot Sketch FDM printer, maintaining consistent process parameters: 100% infill density, 0.4 mm nozzle diameter, and 220°C extrusion temperature. The specimens adhered to ISO 257-2-A tensile test geometry. The infill types were chosen to represent a spectrum of mechanical behaviours, ranging from stretch-dominated (e.g., Octet) to bending-dominated (e.g., Lines) configurations.

Tensile tests were conducted using an MTS 810 universal testing machine at a constant displacement rate of 1 mm/min. Measured parameters included axial and transverse strain, stress, displacement, and surface temperature distribution via thermal imaging (FLIR camera) [13-15].

The Octet pattern demonstrated the highest ultimate tensile strength of 30.43 MPa due to its efficient axial load transfer. However, the Lines pattern exhibited the highest elongation and the greatest strain range c.a. 0.1, with the highest constriction percentage of 8.73%, indicating superior energy dissipation and a more gradual failure mechanism.

These findings underscore the critical influence of internal geometry on the mechanical behaviour of PLA parts and highlight the limitations of evaluating structural performance based solely on peak strength. While engineering stress–strain data are typically sufficient for small-strain analysis, their accuracy diminishes beyond the yield point, particularly in cases involving necking or localized deformation. The relevance of true stress–strain models in such regimes has been well established in prior work [16, 17].

This study demonstrates that infill topology can be strategically employed to tailor the tensile response of 3D printed PLA, offering valuable design flexibility for applications that demand both strength and resilience, such as thermal sensor housings and energy storage enclosures.

2 TENSILE TEST BACKGROUND

In analysing the tensile behaviour of lattice structures, it is essential to distinguish between engineering stress–strain and true stress–strain formulations. These differences are non-trivial in structures undergoing large deformations or where necking and geometric nonlinearity dominate, as is often the case with architected materials [3]. Engineering stress (σ_e) and engineering strain (ε_e) are defined with respect to the initial dimensions of the specimen:

$$\sigma_e = \frac{F}{A_O} \tag{1}$$

$$\varepsilon_e = \frac{L - L_O}{L_O} = \frac{\Delta L}{L_O} \tag{2}$$

where:

- σ_e engineering stress, Pa
- F applied load, N
- A_O original cross-sectional area, m^2
- ε_e engineering strain, -
- L sample length, m
- L_O original gauge length, m
- ΔL change in sample length, m

These formulations assume a constant cross-section and are valid for small deformations. However. in the load–displacement plot. we observe significant displacement values (up to 1.8 mm for the Lines structure). at which point the assumption of a constant area is no longer accurate.

Particularly for the Octet structure. which experiences a rapid load drop after peaking. This suggests localized necking or failure—a behaviour not well captured by engineering stress analysis. To better understand the actual material response true stress (σ_t) and true strain (ε_t) are used. accounting for the continuously changing cross-section and length:

$$\sigma_t = \frac{F}{A_i} = \sigma_e(1 + \varepsilon_e) \tag{3}$$

$$\varepsilon_t = \ln(1 + \varepsilon_e) \tag{4}$$

where:

- σ_t true stress, Pa
- A_i instantaneous cross-sectional area, m^2
- ε_t true strain, -

Although true stress and strain provide a more physically accurate description of material deformation, engineering stress and engineering strain remain the primary descriptors in standard tensile testing, particularly for semi-brittle polymers like polylactic acid (PLA). Engineering stress (σ_e) and engineering strain (ε_e) are defined based on the original geometry of the specimen.

While the expression (1) and (2) assume uniform deformation and constant cross-section, such assumptions hold reasonably well in brittle and semi-brittle materials like PLA, where plastic flow is limited and deformation localizes rapidly after yield [18]. Mechanical properties depend strongly on the selected PLA filament and can vary, as shown in Table I.

Table I - Mechanical properties of PLA filament

Properties	Value
Tensile modulus (GPa)	2.34 [18]
	3.3 [19]
Ultimate tensile strength (MPa)	54 [18]
	57.7 [19]
Maximum elongation (%)	2.2 [18]
	6.8 [19]
Yield stress (MPa)	50.51 [18]
	48.2 [20]

Table II - 3D printing parameters for fabricating PLA samples

Printing settings	Value
Layer height	0.2 mm
Line width	0.4 mm
Wall thickness	0.4 mm
Top/bottom thickness	0.4 mm
Printing speed	80 mm/s
Extruder temperature	220°C
Build plate temperature	50°C
Nozzle diameter	0.4 mm
Infill density	100 %
Infill patterns	Cubic; Quarter-cubic; Lines; Octet; Triangles

3 MATERIALS AND METHODS

3.1 ADDITIVE MANUFACTURING OF BIODEGRADABLE PLA SAMPLES

The specimens were fabricated using a Fused Deposition Method (FDM) printer, MakerBot Sketch Large, utilizing biodegradable PLA filament (CadXpert, Poland) as the printing material.

The printing process was prepared using Cura slicing software, which enabled precise control over print settings and infill structures. Five distinct infill geometries were selected for comparative analysis: Cubic, Quarter-cubic, Lines, Octet, and Triangles (Figure 1).

Each infill type was applied uniformly throughout the volume of the specimen, while maintaining consistent outer shell and layer parameters.

Cura was used to configure all slicing parameters, including layer height, wall thickness, infill percentage, and print speed, ensuring consistent fabrication conditions across all specimens.

The 3D printing parameters used for bio-PLA printing are shown in Table II. All samples were printed in the WiMIR Laboratory, with careful monitoring to ensure dimensional accuracy and material integrity. After printing, each specimen was manually inspected and post-processed to remove any residual printing artifacts.

The geometrical design of the samples conformed to the ISO 257-2-A standard, as shown in Figure 2, and uniform sample orientation on the build plate was maintained to minimize variability due to print direction.

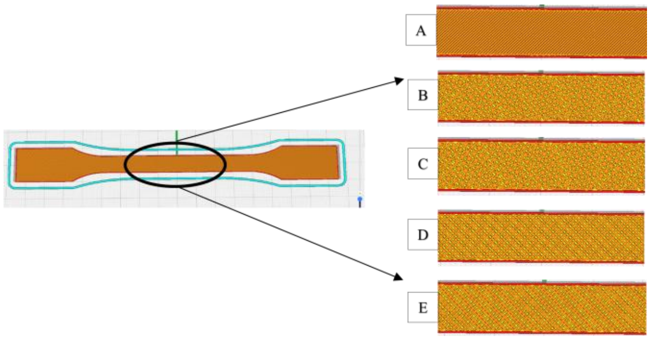

Figure 1 Infill pattern of samples used for tensile tests: a) Cubic; b) Lines; c) Triangle; d) Octet; e) Quarter-Cubic.

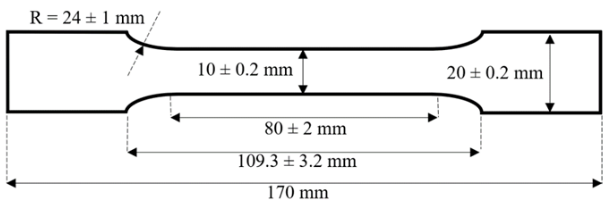

Figure 2 Tensile test sample configuration according to ISO 257-2-A standard.

3.2 TENSILE TEST AND THERMAL MONITORING METHOD

Static tensile tests were carried out using an MTS 810 servo-hydraulic testing machine with a maximum load capacity of 100 kN, as illustrated in Figure 3a. The testing system was controlled via an MTS FlexTest SE controller and operated via TestWorks 4 software, enabling precise control of loading parameters and real-time data acquisition. Test specimens (Figure 4) were firmly secured in the machine's hydraulic grips to prevent misalignment or slippage during testing, as shown in Figure 5. The total number of tested samples was 25 samples consisting of 5 different infill groups (Cubic, Lines, Triangle, Octet, Quarter-Cubic). Each infill pattern was examined 5 times (5 different samples), and the results presented in Figure 8 represent one selected test for each infill. Ultimate tensile strength, Elastic modulus, and Poisson's ratio for different infill patterns, and variability, presented in Figure 9, were calculated for each kind of infill as mean value from 5 tests.

The tensile tests were conducted under displacement control at a constant actuator speed of 1 mm/min, ensuring deformation remained within the material's elastic range.

Throughout each test, the following parameters were continuously recorded: actuator displacement $S(t)$ (mm), tensile force $P(t)$ (N), longitudinal strain $\varepsilon(t)$ (mm), and transverse strain $\varepsilon_{tr}(t)$ (mm).

The actuator displacement signal $S(t)$ was obtained from an integrated Linear Variable Displacement Transformer (LVDT), which measures the actuator's relative movement with high accuracy.

This displacement data directly corresponds to the applied load, providing insight into the specimen's global stiffness and mechanical response.

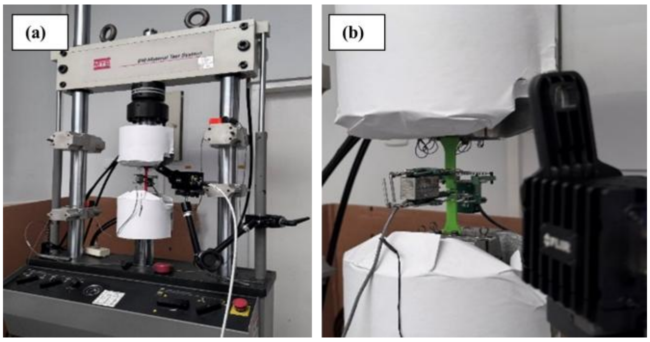

Figure 3 Tensile set up with thermal camera (a), Thermal camera monitoring (b).

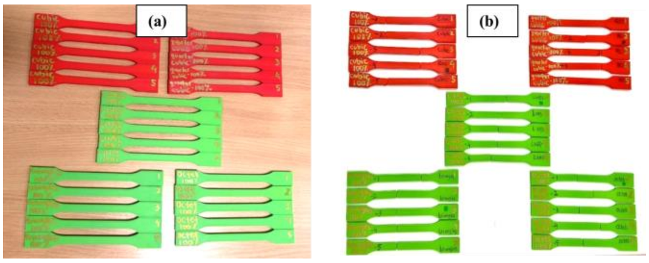

Figure 4 The samples with different infill pattern group after 3D printing (a) and after tensile testing (b).

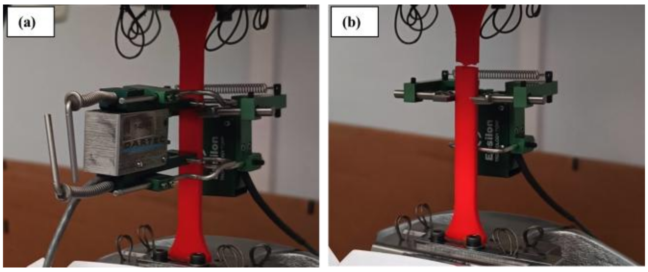

Figure 5 Sample before (a) and after (b) damage.

To accurately capture local strain behaviour, a clip-on extensometer (Epsilon 3542-025M-025-ST) was used to measure longitudinal strain over a 25 mm gauge length, with a ±6.25 mm measurement range. Transverse strain was simultaneously measured using an extensometer, featuring a ±2.5 mm range. Both extensometers were directly attached to the test specimen to ensure precise tracking of deformation. In addition to mechanical measurements, a FLIR thermal imaging camera was employed to monitor the thermal response of the PLA specimen during tensile loading. This enabled visualization of any localized heating effects, which could indicate the onset of plastic deformation, strain localization, or dissipative mechanisms [13, 14, 21]. The thermal monitoring setup is depicted in Figure 3b.

3.3 THERMAL CONDUCTIVITY AND EFFUSIVITY

Typically, thermoplastic materials exhibit relatively low thermal conductivity, which falls within the range of 0.1 to 0.25 W/(m·K), depending on factors such as crystallinity, molecular orientation, and the presence of fillers or reinforcements [22-27]. The inherently low thermal conductivity of PLA limits its ability to dissipate heat efficiently which can influence its performance in thermal management applications and affect cooling rates during processing.

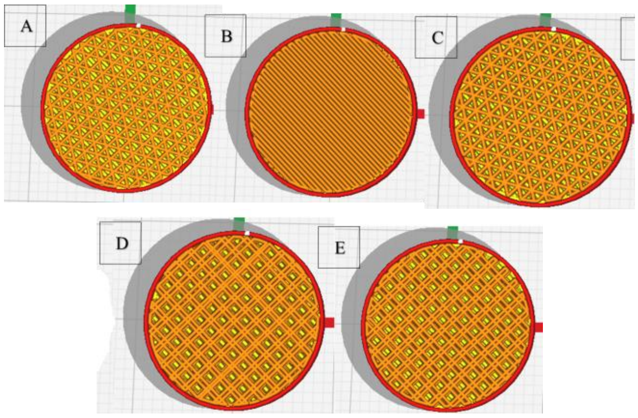

Figure 6 Infill patterns used during thermal conductivity tests: a) Cubic; b) Lines; c) Triangle; d) Octet; e) Quarter-Cubic.

Figure 7 Experimental setup for thermal conductivity measurement of PLA sample printed with different infill geometries using the C-Therm Trident thermal analyser with MTPS sensor.

However, this property can be advantageous in applications requiring thermal insulation. Modifications, such as the incorporation of conductive fillers (e.g., carbon fibres, graphene), are often employed to enhance PLA's thermal conductivity when needed. The thermal conductivity and thermal effusivity of PLA samples with varying infill geometries were measured using a C-Therm Trident thermal analyser equipped with a Modified Transient Plane Source (MTPS) sensor. This technique utilizes a transient method, enabling rapid, non-destructive analysis with minimal sample preparation. For testing thermal conductivity and effusivity, PLA samples were 3D-printed as 18 mm diameter, 8 mm thick discs. The design of infill patterns used during thermal conductivity tests is presented in Figure 6. The dimensions selected to ensure full contact with the sensor surface and meet the instrument's minimum size requirements. Different internal infill geometries were implemented during printing to study their effects on thermal transport behaviour. The setup for measuring the thermal conductivity and effusivity of PLA samples with different infill geometries is shown in Figure 7.

4 RESULTS AND DISCUSSION

4.1 LOAD-DISPLACEMENT AND STRESS-STRAIN

The mechanical behaviour of five distinct infill structures such as Lines, Octet, Cubic, Quarter-Cubic, and Triangles was investigated under uniaxial tensile loading using a universal testing machine.

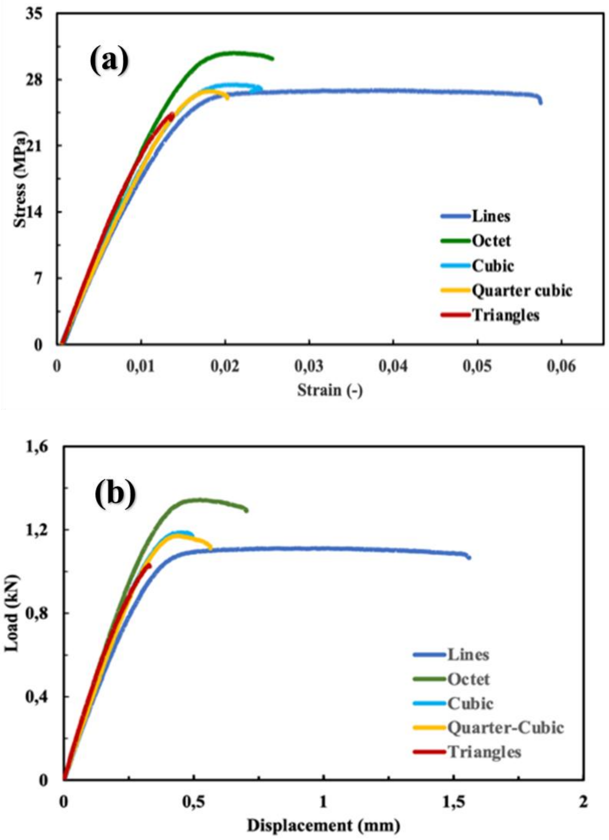

Figure 8 Stress-strain (a) and Load-displacement (b) curves for different infill patterns.

The displacement was applied through a hydraulically driven crosshead, and the tensile strength was determined based on the applied load at the fracture point. Yield strength was recorded for each infill configuration, offering insight into the influence of internal geometry on structural performance.

The stress–strain and load–displacement responses of the specimens are illustrated in Figure 8. These results demonstrate the critical role of infill architecture on both global and local mechanical behaviour. Although engineering stress and strain metrics were used in the analysis, it is important to acknowledge their limitations—particularly in the post-yield regime—due to the emergence of geometric and material nonlinearities. Consequently, these measures provide only an approximate representation of the actual mechanical state of the material.

Among the tested structures, the Octet lattice exhibited the highest peak load of 1.38 kN at 0.56 mm displacement), indicating superior stiffness and load-bearing capability attributed to its stretch-dominated topology. However, the sharp decline following the peak suggests a brittle failure mode, likely resulting from localized instability or nodal collapse.

The Cubic and Quarter-Cubic lattices followed similar trends, reaching peak loads of 1.25 kN and 1.22 kN, respectively; with abrupt failure occurring shortly after their load maxima near 0.5 mm displacement.

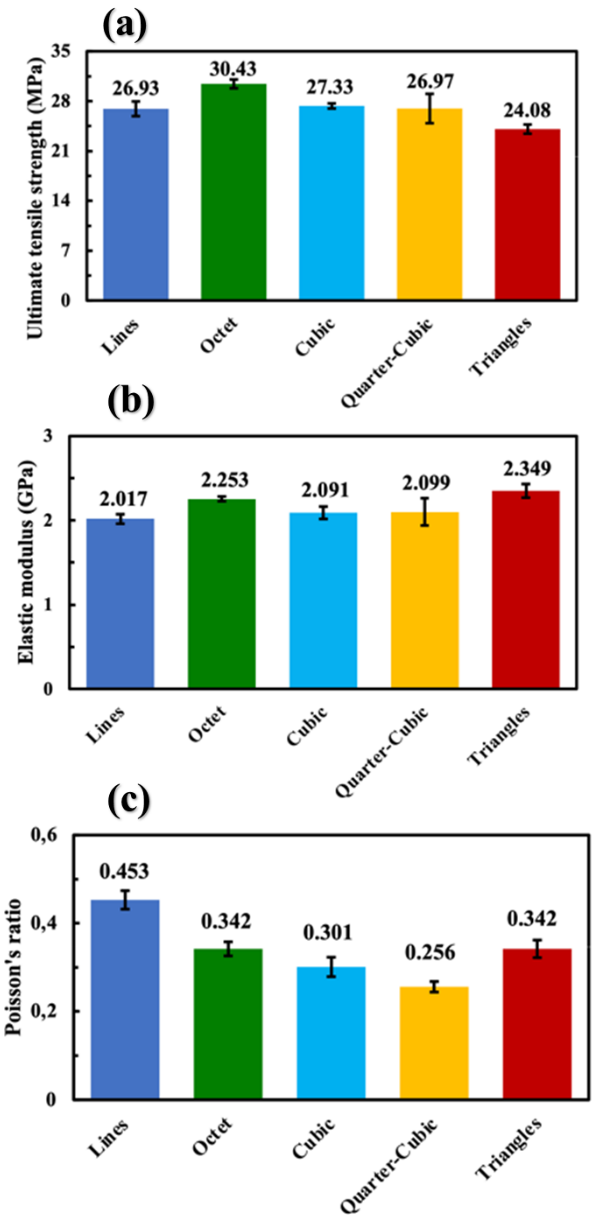

Figure 9 Ultimate tensile strength, Elastic modulus, and Poisson's ratio for different infill patterns.

In contrast, the Lines infill structure demonstrated a more gradual post-peak response, attaining a lower maximum load of 1.1 kN, yet sustaining it over a significantly broader displacement range of 1.8 mm. This behaviour implies enhanced energy absorption and greater deformation tolerance, typical of bending-dominated systems. The Triangles structure followed a comparable pattern, reaching a peak load of 1.18 kN at 0.48 mm, before transitioning into a more ductile failure regime.

The corresponding engineering stress–strain curves further support these findings. The Octet lattice achieved the highest peak engineering stress of 30 MPa, closely followed by the Cubic (28.5 MPa) and Quarter-Cubic (28 MPa) structures. All three exhibited immediate post-peak softening, indicative of limited strain capacity and early onset of localized damage. In contrast, the Lines and Triangles structures showed lower peak stresses of 26 MPa and 25 MPa, respectively; but maintained deformation across extended strain intervals suggesting improved ductility and strain redistribution.

It is critical to highlight the divergence between engineering and true stress–strain representations in the post-yield regime. True stress, defined as the stress at the instantaneous cross-sectional area, continues to rise even as engineering stress declines, particularly during phenomena such as necking or internal structural collapse. True strain, being logarithmic and incremental, provides a more accurate account of material behaviour under non-uniform deformation conditions, as observed in the Lines configuration.

These differences have significant implications for evaluating post-yield mechanical performance. While stretch-dominated lattices like Octet show superior peak strength, they may lack the capacity for sustained deformation and energy dissipation. Conversely, structures such as Lines, despite lower peak stresses, exhibit superior ductility and resilience, potentially outperforming higher-stress configurations in terms of energy absorption and toughness when evaluated using true stress–strain metrics. This behaviour aligns with trends observed in compliant and bioinspired lattice architectures, where distributed yielding and structural adaptability are critical to mechanical efficiency.

4.2 ULTIMATE TENSILE STRENGTH, ELASTIC MODULUS, AND POISSON'S RATIO

The mechanical characterization of five bioinspired lattice structures—Lines, Octet, Cubic, Quarter-Cubic, and Triangles—provides important insights into the design of next-generation biomaterials. Among the evaluated geometries, the Octet lattice demonstrated the highest ultimate tensile strength (UTS) at 30.43 MPa, highlighting its potential for load-bearing biomedical applications such as bone scaffolds or orthopaedic implants (Figure 9a). This superior strength is attributed to the Octet's highly interconnected nodal network, which effectively distributes stress under tensile loads. The Cubic and Quarter-Cubic structures also showed competitive strength values of 27.33 MPa and 26.97 MPa, respectively, suggesting their viability in moderate load-bearing applications.

In contrast, the Triangles structure recorded the lowest UTS at 24.08 MPa, which may limit its utility in high-stress environments but still positions it as a candidate for low-load, lightweight tissue scaffolding.

In terms of stiffness, as measured by elastic modulus, the Triangles structure led with a value of 2.349 GPa, followed closely by the Octet (2.253 GPa), indicating their suitability in applications requiring rigid structural integrity, such as dental or cranial implants (Figure 9b). The Lines structure, though lowest in stiffness (2.017 GPa), may offer value in applications where flexibility and compliance are more critical, such as soft tissue integration or bioresorbable scaffolds. The relatively high stiffness of the Octet, combined with its tensile strength, reinforces its promise as a multifunctional lattice for bone-mimetic materials.

Poisson's ratio further differentiates these lattices in terms of deformation behaviour.

The Lines structure exhibited the highest Poisson's ratio at 0.453, indicative of greater lateral expansion under axial strain—an attribute that may mimic the behaviour of certain soft biological tissues (Figure 9c).

Conversely, the Quarter-Cubic structure exhibited the lowest Poisson's ratio (0.256), suggesting enhanced dimensional stability, which is desirable for load-transmitting implants or bioresorbable meshes. The Octet and Triangles structures shared an intermediate Poisson's ratio of 0.342, balancing ductility and stability.

4.3 THERMO-MECHANICAL PROPERTIES

During the tensile tests, the temperature field on the specimen surface was continuously recorded using an infrared thermal imaging camera before and until the failure of the specimen occurred. Subsequently, the recorded thermographic data were analysed using FLIR software. The temperature analysis was performed within a predefined rectangular measurement area indicated in Figure 12.

For each recorded frame, the software automatically determined the minimum, maximum, and average temperature values within the selected region of interest. These temperature parameters were then correlated with the simultaneously recorded mechanical data, including tensile force and specimen elongation.

The combined thermomechanical characteristics were presented in Figures 13–15 to illustrate the relationship between the mechanical response of the specimens and the evolution of temperature during the deformation and fracture process.

Thermal imaging during the tensile test for the cubic pattern group, as a representative sample, shows a gradual temperature rise in the region of impending damage, peaking just before fracture (Figures 10–12, as described).

The maximum temperature recorded near the damage site increases steadily with time, coinciding with the period of plastic deformation and stress concentration. This localized heating is due to internal friction and microstructural rearrangements as the sample undergoes strain, a phenomenon known as the thermoelastic effect. The observed temperature plateau just prior to failure (visible on the time–temperature chart) aligns with the onset of maximum stress, after which both stress and temperature decrease sharply following material rupture.

The Figures 13-15 display the recorded temperature distribution of the sample (e.g., the cubic group) over time while a mechanical load is applied axially during tensile testing. Initial temperatures were recorded at approximately 28°C (max), 27°C (min), and 25°C (avg).

Throughout most of the test, both minimum and maximum temperatures gradually decreased, while the average remained stable around 24–25°C, indicating negligible heat generation during the early stages of deformation.

The applied load increased steadily from 0 N to approximately 1.2 N by 140 seconds, then decreased slightly as failure approached.

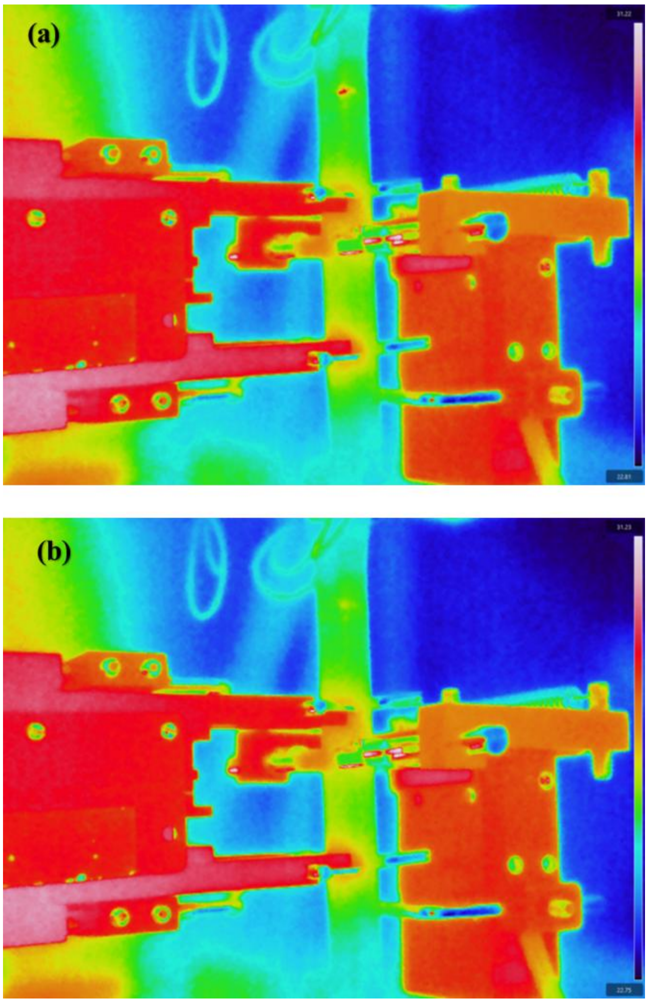

Figure 10 Temperature distribution during the tensile test with marked point of damage before damage (a) and just before damage (b).

Extension progressed nearly linearly, reaching approximately 0.45 mm before test completion, reflecting typical elastic and plastic deformation phases prior to material rupture, with no abrupt changes until the final stage.

A sharp temperature spike was observed during the last 10–15 seconds of testing, coinciding with a slight drop in load and a continued increase in extension. This localized thermal surge is likely due to rapid deformation, frictional effects, or microstructural failure mechanisms, such as polymer chain slippage or crack initiation [21, 28].

The correlation between mechanical and thermal behaviour in the cubic infill group is clearly demonstrated through both the property measurements and thermal imaging analyses. The cubic infill structure demonstrated moderate mechanical properties, with an ultimate tensile strength of 27.33 MPa and an elastic modulus of 2.09 GPa, allowing it to sustain and distribute stress uniformly under load. Its intermediate thermal conductivity (0.495 W/m·K, Table IV) enabled efficient heat dissipation throughout deformation, preventing excessive global temperature rise while permitting localized heating at regions of concentrated stress.

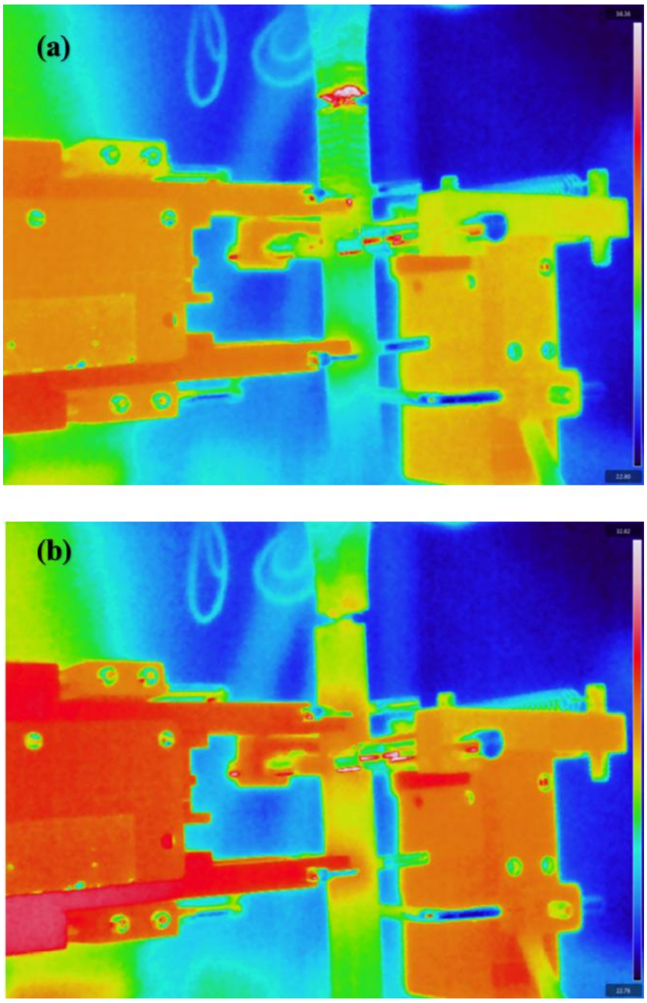

Figure 11 Temperature distribution during the tensile test (just after damage) with place of damage (a), and temperature distribution during the tensile test (after damage) with place of damage after cooling down (b).

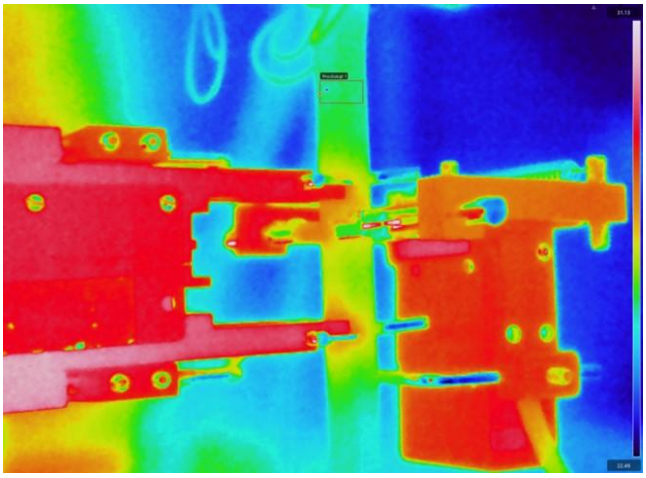

Figure 12 Sample with marked region when the temperature change was monitored and presented in Figure 13.

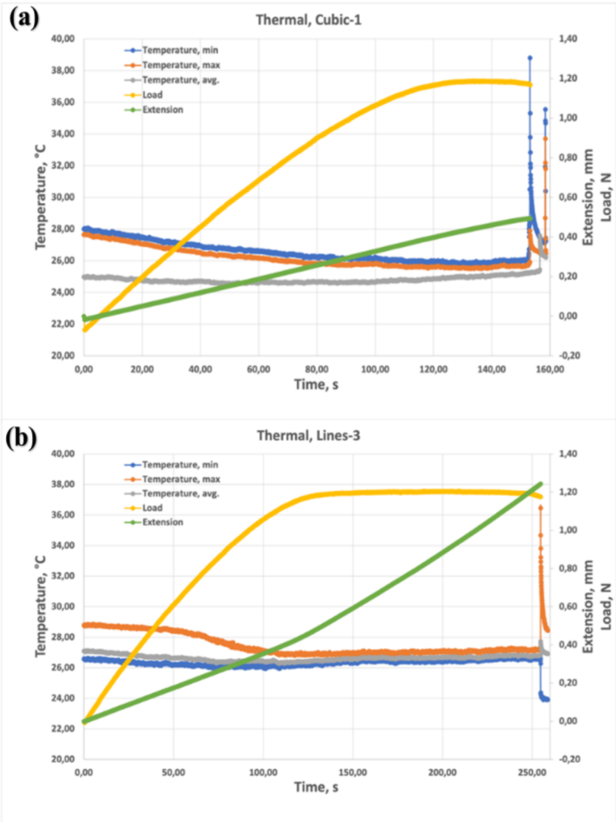

Figure 13 Minimum (blue), maximum (orange) and mean temperature (grey) close to the damaged region registered by thermal camera and stress as a function of time during tensile tests: Cubic sample (a) and Lines sample (b).

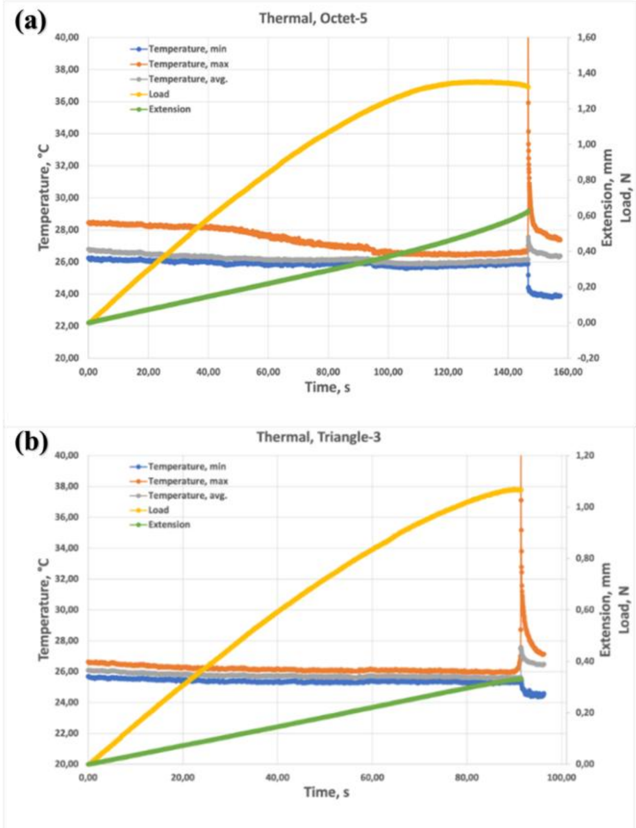

Figure 14 Minimum (blue), maximum (orange) and mean temperature (grey) close to the damaged region registered by thermal camera and stress as a function of time during tensile tests: Octet (a) and Triangle (b).

This behaviour was evident in the thermal imaging sequence, where uniform temperatures dominated the early elastic phase. As flaws developed and local stress intensified, a sharp, localized thermal spike appeared at critical points, reaching approximately 33–35°C in the last 10–15 seconds of testing, coinciding with a slight load drop. This spike is attributed to rapid deformation, internal friction, and microstructural failure processes such as polymer chain slippage or crack propagation. Immediately after fracture, the region exhibited rapid cooling, corresponding to the mechanical release of stored energy and structural relaxation. The thermal imaging sequence acquired during tensile testing vividly tracks these events. Initially, the temperature remains uniform and stable across the specimen, reflecting the early elastic regime where deformation is well distributed. As the test progresses and stress concentrates at emerging flaws, a sharp, localized temperature rise appears at the anticipated damage area, corresponding to intense internal friction and microstructural activity as the cubic sample approaches failure. Immediately after fracture, a rapid cooling of the region is observed, aligning with the mechanical event of energy release and structural relaxation. These observations highlight that, for the cubic infill, the interplay among its moderate strength, modulus, and thermal conductivity effectively confines significant thermal events to small regions, thereby determining significant failure through thermal spikes.

Thus, the temperature evolution during mechanical loading mirrors the progression of damage, providing useful markers for monitoring structural health and anticipating material failure in real-time.

4.4 PERCENTAGE ELONGATION

The elongation data reveals distinct patterns across different measurement stages and infill geometries. A_t the cross-section (Z), the Lines infill demonstrates the highest elongation capacity (8.73%), closely followed by Quarter-Cubic (8.29%), while triangles show the lowest (4.10%). This suggests that the Lines pattern's bending-dominated structure and Quarter-Cubic's partial connectivity facilitate greater local deformation. At length after rupture (A), a dramatic shift occurs where Lines exhibits exceptional elongation (0.954%), significantly exceeding all other patterns. This finding corroborates the previous mechanical testing results, confirming Lines' superior ductility and post-yield deformation capacity. The other infill patterns show minimal elongation values (0.026-0.129%), indicating more brittle failure modes. At maximum force (A_{max}), the Octet and Lines structures exhibit the highest elongations (0.08836% and 0.12924%, respectively), consistent with their superior mechanical performance. The convergence of Cubic and Quarter-Cubic values (0.07256% and 0.07352%) suggests similar deformation mechanisms at peak load, while Triangles maintains the lowest elongation (0.05488%), reflecting its inherently stiff and brittle nature.

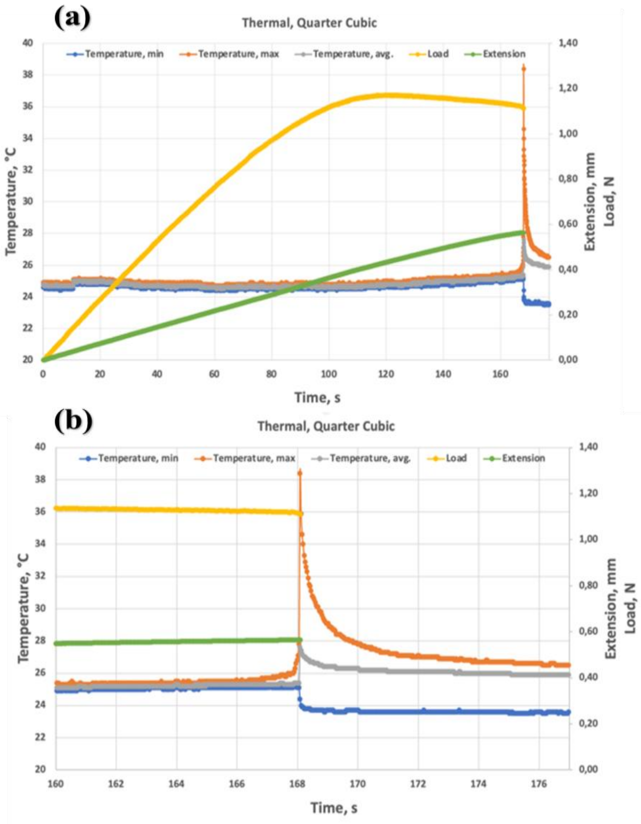

Figure 15 Minimum (blue), maximum (orange) and mean temperature (grey) close to the damaged region registered by thermal camera and stress as a function of time during tensile tests: Quarter-Cubic (a) and zoom for the test period around time of damage (b).

4.5. YIELD, ULTIMATE TENSILE AND FAILURE STRENGTH

The tensile behaviour of PLA specimens produced with different 3D printing infill patterns was systematically evaluated. Some mechanical properties, such as yield strength, ultimate tensile strength, failure strength, and strain at maximum load, were obtained from stress–strain analyses (Figure 16). The comparative evaluation of the infill patterns reveals that mechanical performance is highly influenced by infill geometry. The octet and quarter-cubic structures enhance both strength and ductility relative to the more conventional cubic and triangular designs. In contrast, line infill, despite its lower yield strength, offers the greatest ductility, which can be advantageous for parts subjected to intermittent or impact loads. The observed trends reflect how infill geometry alters the deformation and failure mechanisms of PLA under tensile loading. Structures with interconnected pathways (e.g., octet) better distribute stress and delay failure, while simpler patterns (e.g., triangles) localize strain, resulting in less ductility. It suggests that the selection of an infill pattern can be tailored to specific performance requirements, with octet for high-strength/ductility applications, lines for flexibility, and cubic or quarter-cubic for optimal weight/strength balance. The results align with typical PLA behaviours, modulated by infill architectures, highlighting the potential for design optimization in 3D printed functional components.

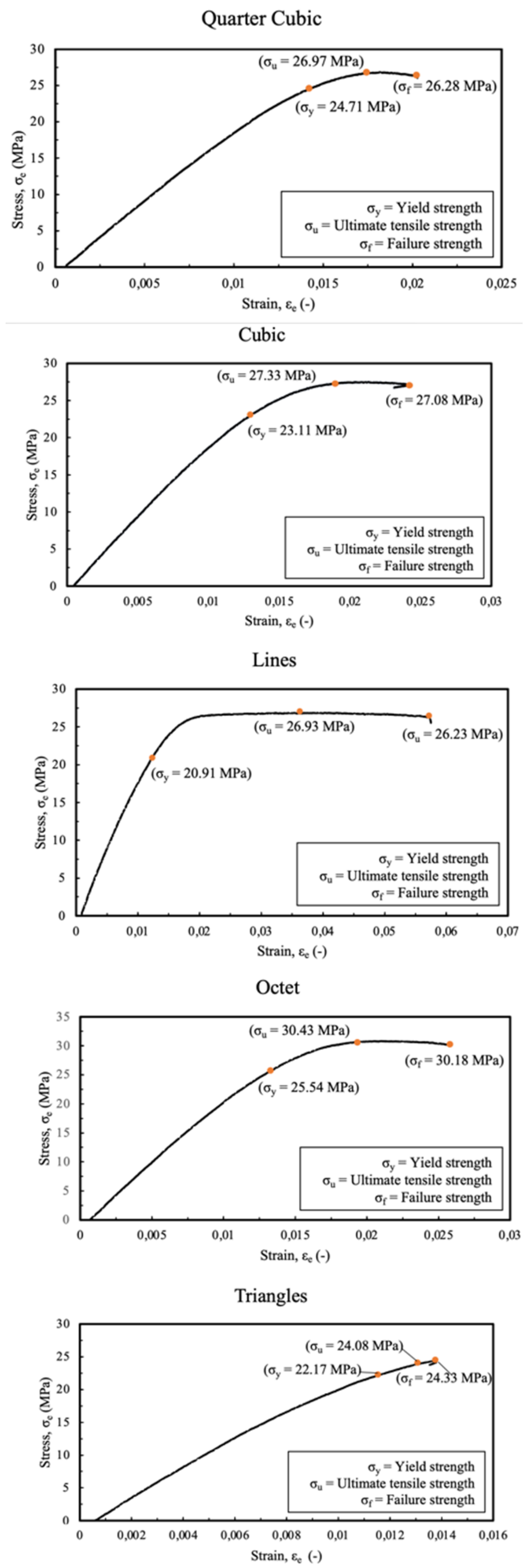

Figure 16 Yield, Ultimate Tensile and Failure Strength points of different infill geometries.

4.6 THERMAL CONDUCTIVITY AND EFFUSIVITY

The thermal characterization of 3D printed PLA specimens reveals significant variations in thermal properties across different infill geometries. The thermal conductivity and effusivity values were obtained using a Trident device with a Modified Transient Plane Source (MTPS) sensor, while density was calculated from the diameter, thickness, and mass of the disc samples used for thermal conductivity measurement. The obtained density values were subsequently used to calculate the specific heat capacity. The obtained thermal conductivity and effusivity values are presented in Table IV. The calculated density and specific heat of the disc samples used for thermal conductivity measurement are presented in Table V.

Thermal analysis reveals that the Quarter-Cubic exhibits the highest thermal conductivity (0.868 W/m·K) and effusivity (1203.6 W·s1/21/2/m22·K), while also having the lowest density (1188.91 kg/m33) and the highest specific heat capacity (1403.77 J/kg·K). This suggests that the Triangle infill provides efficient heat-transfer paths despite its reduced material content, owing to its geometric configuration. In contrast, the Quarter-Cubic and Lines infills show the lowest thermal conductivities (0.340–0.344 W/m·K) and effusivities (702.8 W·$s^{1/2}$/m^2·K), making them more suitable for thermal insulation applications.

Table III - Percentage elongation at cross-section (Z), at length after rupture (A), and at maximum force (A_{max})

Group	Elongation Z (%)	Elongation A (%)	Elongation A_{max} (%)
Quarter-Cubic	8.29	0.031	0.07256
Cubic	5.46	0.026	0.07352
Octet	4.53	0.129	0.08836
Lines	8.73	0.954	0.12924
Triangles	4.10	0.026	0.05488

Table IV - Measured mean value of thermal conductivity and effusivity of PLA samples with different infill geometries

Group	Thermal Conductivity (k) [W/m·K]	Thermal Effusivity (e) [W·$s^{1/2}$/m^2·K]
Quarter-Cubic	0.8680	1203.6
Cubic	0.4951	855.2
Octet	0.3400	702.8
Lines	0.3445	702.8
Triangles	0.3832	742.6

Table V - Calculated density and specific heat of disc samples used for thermal conductivity measurement

Group	Density (kg/m^3)	Specific heat (J/kg·K)
Quarter-Cubic	1224.98	1185.92
Cubic	1231.82	1199.21
Octet	1226.25	1173.55
Lines	1252.11	1145.07
Triangles	1188.91	1403.77

5 CONCLUSIONS

This experimental study demonstrates that infill geometry significantly governs the tensile performance of 3D printed PLA. The Octet lattice exhibited the highest strength (30.43 MPa) and notable ductility, due to its stretch-dominated architecture.

Meanwhile, the Lines pattern offered superior elongation at break and energy absorption, making it advantageous for toughness-critical applications. Cubic and Triangles infills achieved greater stiffness but lower ductility, while Quarter-Cubic provided balanced yet variable properties.

This study reveals that infill patterns that promote high thermal conductivity, such as the Triangle pattern, tend to have lower tensile strength but greater stiffness, making them ideal for applications that demand efficient heat dissipation with minimal structural loads, such as electronic enclosures or heat sinks. In contrast, designs like Quarter-Cubic and Lines offer lower thermal transfer but improved energy absorption and ductility, making them well suited for applications where thermal insulation and impact resistance are prioritized.

The Octet structure uniquely offers a balance of strong mechanical properties and intermediate thermal performance, representing a versatile choice for multifunctional applications that require both strength and moderate thermal management.

The time-dependant analysis of temperature and stress during tensile testing for the cubic infill group reveals that the temperature remains relatively stable during the elastic regime and rises just before reaching the peak stress.

This localized temperature increase corresponds to the onset of material plasticity and imminent damage, providing a clear thermal signature of failure in real-time.

The temperature then drops sharply as the specimen fractures and stress is released, affirming the link between mechanical events and heat generation.

The strong correlation among stress concentrations, temperature changes, and failure also underscores the utility of thermal monitoring as a diagnostic tool for structural health assessment of additively manufactured parts.

These results establish that targeted mechanical properties in PLA components can be achieved through appropriate infill selection, informing optimized design for applications such as thermomechanical housings and energy devices.

Future studies should extend this work to cyclic loading and advanced simulations to further validate the practical performance of these architectures.

ACKNOWLEDGEMENTS

The research project is supported by the program Excellence Initiative – Research University" for AGH University.

REFERENCES

[1] Deshpande V.S., Ashby M.F. and Fleck N.A., Foam topology: bending versus stretching dominated architectures. *Acta Materialia*, Vol. 49, No. 6, pp. 1035-1040, 2001.

[2] Gibson L.J. and Ashby M.F., *Cellular Solids: Structure and Properties*. Cambridge University Press, 1997.

[3] Zheng X. et al., Ultralight, ultrastiff mechanical metamaterials. *Science*, Vol. 344, No. 6190, pp. 1373-1377, 2014.

[4] Farah S., Anderson D.G. and Langer R., Physical and mechanical properties of PLA, and their functions in widespread applications - A comprehensive review. *Advanced Drug Delivery Reviews*, Vol. 107, pp. 367-392, 2016.

[5] Garlotta D., A literature review of poly(lactic acid). *Journal of Polymers and the Environment*, Vol. 9, No. 2, pp. 63-84, 2001.

[6] Gopalakrishnan S., Senthilkumar N., Deepanraj B., Asad M. and Perumal G., Fused deposition modelling in additive manufacturing: A comprehensive review of polymer-based processes, properties, and applications. *Advanced Engineering Letters*, Vol. 5, No. 1, pp. 12-25, 2026.

[7] Cano-Vicent A. et al., Fused deposition modelling: Current status, methodology, applications and future prospects. *Additive Manufacturing*, Vol. 47, 102378, 2021.

[8] Lanzotti A., Grasso M., Staiano G. and Martorelli M., The impact of process parameters on mechanical properties of parts fabricated in PLA with an open-source 3-D printer. *Rapid Prototyping Journal*, Vol. 21, No. 5, pp. 604-617, 2015.

[9] Spoerk M., Gonzalez-Gutierrez J., Sapkota J., Schuschnigg S. and Holzer C., Effect of the printing bed temperature on the adhesion of parts produced by fused filament fabrication. *Plastics, Rubber and Composites*, Vol. 47, No. 1, pp. 17-24, 2018.

[10] Morettini G., Palmieri M., Capponi L. and Landi L., Comprehensive characterization of mechanical and physical properties of PLA structures printed by FFF-3D-printing process in different directions. *Progress in Additive Manufacturing*, Vol. 7, No. 5, pp. 1111-1122, 2022.

[11] Kayacan M.Y., Mechanical investigation of compositing by resin filling in lattice structures manufactured with fused deposition modelling. *Journal of Reinforced Plastics and Composites*, Vol. 43, No. 17-18, pp. 1-15, 2024.

[12] Nale A. and Chiozzi A., Multiscale topology optimization with embedded TPMS architected materials. International *Journal of Mechanical Sciences*, Vol. 295, 110204, 2025.

[13] Feng Y. et al., A lattice-solid hybrid structure topology optimization method for support-free additive manufacturing. *Journal of Graphics*, Vol. 44, No. 5, pp. 1013-1020, 2023.

[14] Ben Hariz N., Boulila A. and Ayadi M., The influence of 3D printing process parameters in the dimension accuracy, roughness, and weight. *International Journal of Mechanics and Control*, Vol. 25, No. 2, pp. 47-52, 2024.

[15] de Camargo J.C., da Silva Neto A.J., Knupp D.C., da Silva Abreu L.A. and de Andrade G.M., Theoretical and experimental approach with inverse problems for the thermal characterization of parts printed by FDM. *International Journal of Advanced Manufacturing Technology*, Vol. 136, No. 3, pp. 1741-1755, 2025.

[16] Bridgman P.W., *Studies in large plastic flow and fracture*. McGraw-Hill, New York, 1952.

[17] Callister W.D. and Rethwisch D.G., *Materials Science and Engineering: An Introduction*. John Wiley & Sons, 2020.

[18] Wittbrodt B. and Pearce J.M., The effects of PLA color on material properties of 3-D printed components. *Additive Manufacturing*, Vol. 8, pp. 110-116, 2015.

[19] Suryanegara L., Nakagaito A.N. and Yano H., The effect of crystallization of PLA on the thermal and mechanical properties of microfibrillated cellulose-reinforced PLA composites. *Composites Science and Technology*, Vol. 69, No. 7-8, pp. 1187-1192, 2009.

[20] Kowalczyk M., Piorkowska E., Kulpinski P. and Pracella M., Mechanical and thermal properties of PLA composites with cellulose nanofibers and standard size fibers. *Composites Part A: Applied Science and Manufacturing*, Vol. 42, No. 10, pp. 1509-1514, 2011.

[21] Cuadri A.A. and Martín-Alfonso J.E., Thermal, thermo-oxidative and thermomechanical degradation of PLA: A comparative study based on rheological, chemical and thermal properties. *Polymer Degradation and Stability*, Vol. 150, pp. 37-45, 2018.

[22] Bute I., Tarasovs S., Vidinejevs S., Vevere L., Sevcenko J. and Aniskevich A., Thermal properties of 3D printed products from the most common polymers. International *Journal of Advanced Manufacturing Technology*, Vol. 124, No. 7-8, pp. 2739-2753, 2023.

[23] Huang X., Jiang P. and Tanaka T., A review of dielectric polymer composites with high thermal conductivity. *IEEE Electrical Insulation Magazine*, Vol. 27, No. 4, pp. 8-16, 2011.

[24] Kumar S., Singh R., Singh T.P. and Batish A., On investigations of thermal conductivity, circumferential compressive strength, and surface characterization of 3D-printed hybrid blended magnetostrictive PLA composite. *Journal of Thermoplastic Composite Materials*, Vol. 35, No. 5, pp. 631-650, 2022.

[25] Spinelli G. et al., Thermal and dielectric properties of 3D printed parts based on polylactic acid filled with carbon nanostructures. *Macromolecular Symposia*, Vol. 405, No. 1, 2100244, 2022.

[26] Blanco I., Cicala G., Recca G. and Tosto C., Specific heat capacity and thermal conductivity measurements of PLA-based 3D-printed parts with milled carbon fiber reinforcement. *Entropy*, Vol. 24, No. 5, 654, 2022.

[27] Shi S., Dai M., Tao X., Wu F., Sun J. and Chen Y., 3D printed polylactic acid/graphene nanocomposites with tailored multifunctionality towards superior thermal management and high-efficient electromagnetic interference shielding. *Chemical Engineering Journal*, Vol. 450, 138248, 2022.

[28] Yang S.L., Wu Z.H., Yang W. and Yang M.B., Thermal and mechanical properties of chemical crosslinked polylactide (PLA). *Polymer Testing*, Vol. 27, No. 8, pp. 957-963, 2008.

ISSN 1590-8844
International Journal of Mechanics and Control, Vol. 27, No. 01, 2026
https://doi.org/10.69076/jomac.2026.0003

POTENTIAL BIAS OF FORMULAS BASED ON BOTH CRITICAL POWER AND W-PRIME TO EVALUATE MAXIMUM OXYGEN CONSUMPTION IN WELL TRAINED CYCLISTS: A PILOT STUDY

Antonio Héctor Dell'Osa[1], Andrea Manuello Bertetto[2], Alessandro Roux[2], Stefano Rosadelli[2], Andrea Fois[3], Ricardo Marcello[4], Alberto Concu[4,6], Fernanda Velluzzi[5], Salvatore Melis[5,6], Myosotis Massidda[5], Filippo Tocco[5,6]

[1]Laboratorio de Electrónica Aplicada y Biomedicina, Universidad Nacional de Tierra del Fuego, Ushuaia, Argentina
[2]Department of Mechanical and Aerospace Engineering, Politecnico di Torino,Turin, Italy
[3]Nomadyca Ltd, Mulago Hospital, Kampala, Uganda
[4]AC Technologies Ltd, Bioimpedance Devices Manufacturing, Cagliari, Italy
[5]Department of Medical Sciences and Public Health, University of Cagliari, Cagliari, Italy
[6]Sporting Life&Medicine Lab, Sardegna Ricerche, Agency for Research, Innovation and Technology Development, Italy

ABSTRACT

In road cycling, the evaluation of both mechanical performance and metabolic energy expenditure is fundamental to characterizing athletes' efficiency during training and competition. In practice, cyclists often rely on mechatronic power meters combined with empirical models to indirectly estimate oxygen consumption and mechanical efficiency. However, the reliability of these indirect approaches remains insufficiently validated, particularly in well-trained athletes. In this study, maximal oxygen consumption ($VO_{2\text{-}max}$) was evaluated in skilled road cyclists by applying the Fick equation, using cardiac output measured beat-by-beat through a wearable device based on electrical impedance cardiography. The resulting metabolic power estimates were compared with those obtained from a critical power (CP) and anaerobic capacity W'-based empirical model derived from mechanical measurements. The findings demonstrated that the mechanical efficiency calculated using the empirical model was approximately 21% lower than that obtained using the Fick-based physiological estimation at maximal mechanical power output. These results indicate that CP–W'-based indirect estimations may introduce systematic bias when applied outside their original calibration framework, highlighting the necessity for experimental validation of empirical metabolic models, especially in high-performance cycling contexts.

Keywords: road cycling, oxygen consumption, impedance cardiography, Fick equation, mechanical efficiency index.

1 INTRODUCTION

Within the realm of competitive cycling, a primary objective involves quantifying the power generated on-bicycle throughout training or competition. The "SRM spider" system [1], engineered by Ulrich Schoberer, was integrated into bicycles to enable the acquisition of mechanical power output during cycling performances (W_{cycl}) with exceptionally high levels of precision [2].

Contact authors: [1]Antonio Héctor Dell'Osa, [2]Filippo Tocco

[1]UNTDF, Usuhaia, Argentina; [2]Dept of Medical Sciences and Public Health, UNICA, Cagliari, Italy
E-mail: [1]ahdellosa@untdf.edu.ar; [2]filippo.tocco@tiscali.it

However, to derive indicators of athletes' mechanical efficiency (η_{cycl}) as the ratio between W_{cycl} and energy cost (E_{cycl}), applying indirect calorimetry methods is essential. These variables are expressed in calories (cal); Equation (1) illustrates this transformation, where the constant 4.18 represents the mechanical equivalent of heat for the calories.

$$W = cal \cdot 4.18 \qquad (1)$$

Unfortunately, although wearable devices capable of measuring non-invasively the oxygen consumption now exist, this custom is still not very usable while cycling due to both the ergonomic complexity of wearing these devices and their still too high cost [3, 4].

Nonetheless, via mathematical models utilizing mechanical parameters detectable during cycling performance, it is possible to derive indirect indicators of strictly metabolic variables—such as anaerobic threshold, anaerobic capacity and, from the "SRM spider" mechanical device, the maximal oxygen consumption, $VO_{2\text{-max(M)}}$ [5].
However, it is established that utilizing the Fick equation regarding oxygen consumption, $VO_{2\text{-max(F)}}$ is derived by multiplying the arteriovenous oxygen difference in blood concentration (a-$vO_2D = CaO_2 - CvO_2$) by cardiac output (CO) according to Equation (2) [6].

$$VO_{2\text{-max}}(F) = CO \cdot (CaO_2 - CvO_2) \quad (2)$$

where (CaO_2) is the arterial blood oxygen content and (CvO_2) is the mixed venous blood oxygen content.
In this study, the E-Physio Tool [7–9] facilitated beat-to-beat non-invasive assessment of CO. Elite road cyclists performed a laboratory-based incremental exhaustive test using their personal bicycles. Utilizing Equation (2), $VO_{2max(F)}$ was derived as a physiologically-grounded estimate via the Fick principle, corresponding to the maximal mechanical workload (W_{max}). This parameter was subsequently compared against the $VO_{2\text{-max(M)}}$ calculated from the CP–W′-based empirical framework by the sitko's mechanical model. This investigation aims to evaluate the concordance between Fick's formulation and Sitko's model, utilizing physiological variables measured during our experimental trials. Consequently, this research underscores the necessity of validating empirical models through novel experiments incorporating non-invasive, cost-effective instrumentation that has been substantiated in earlier literature [6].

2 METHODS

A. *Subjects*

Seven competitive road cyclists were recruited, and their characteristics are presented in Table I. Every athlete was informed of the experimental procedures, and all participants provided written informed consent.

Table I - Morphological and Training Data

Hb *g/dl*	Age *years*	BM *kg*	BH *cm*	BMI *kg/m²*	PC *years*	TW *h:min*
14.2 ±0.4	22.2 ±3.2	73.9 ±5.5	185.8 ±7.9	21.7 ±2.4	7.0 ±6.8	6:15 ±0:21

Hb: arterial blood hemoglobin concentration; BM: body mass; BH: body height; BMI: body weight divided by the square of the height; PC: cycling practice; TW: weekly time spent in cycling training expressed in hours and minutes.

Prior to testing, hemoglobin concentration (Hb) was determined using a portable photometer (B-Hemoglobin, HemoCue, Angelholm, Sweden); this device enables reliable Hb measurement from a single capillary blood drop (10 μl) [10].

B. *Instrumentation and Mathematics*

Figure 1 Elite Direto XR-T was mounted on the cyclist's bicycle to perform the experiment.

The equipment utilized included: the Elite Direto XR-T power meter (Elite Ltd, Italy), the E-Physio Tool [11], and the SpO_2 device (Heartcare PVS LOX 100, China) for assessing arterial blood oxygen saturation percentages.
Mechanical apparatus: the Elite Direto XR-T power meter was selected, which replaces the bicycle's rear wheel by directly connecting the frame (Figure 1). A constant resistance torque mode was selected by cyclists, who self-regulated their cadence and gear ratios. This mechatronic device enables communication with smartphones via ANT+ protocols (ANT-Productions, Belgium), through which it monitored: achieved speed, pedalling cadence, and delivered mechanical power. Acquired data were stored on a Garmin cycle computer (Garmin, Lenexa, KS, USA) and analyzed using Strava software (Strava Inc., San Francisco, CA, USA). The mechatronic tool software calculated: the subject's critical power (CP) representing the anaerobic threshold, the anaerobic capacity for muscle contraction (W'), and the theoretical maximum oxygen consumption as $VO_{2\text{-max(M)}}$. To estimate the $VO_{2\text{-max(M)}}$ relative to body mass (BM), Equation (3) was employed [12].

$$VO_{2\text{-max(M)}} / kg = 16.6 + 8.87 \cdot (W_{max}5' / BM) \quad (3)$$

where $W_{max}5'$ represents the mean maximum power output during 300 s (5 minutes) of pedalling on a cycle ergometer and BM denotes the athlete's body mass; this variable was determined using Equation (4).

$$W_{max}5' = CP + W' / 300s \quad (4)$$

Absolute $VO_{2-max(M)}$ is derived by multiplying (4) by BM.
In this protocol, $W_{max}5'$ was not directly measured via a specific 5-minute constant-load test. Instead, it was calculated from the CP and W′ parameters automatically generated by the power meter software, which were derived from the same incremental ramp test performed by each cyclist. Consequently, the VO_{2-max} estimated through the Sitko model was based on mechanical parameters obtained under identical experimental conditions.

Bioimpedance apparatus: E-Physio Tool is a device developed to measure the electric potential difference between two physiological thoracic points (ΔVt). It operates by applying a low-intensity, high-frequency alternating electrical current I (1 mA, 64 KHz powered independently via a power bank supplying 2 mA max at 5 V) along planes where the neck muscle roots and the xiphoid process lie, respectively. This enables calculating the real component value of thoracic impedance (Zt) through Equation (5):

$$Zt = \Delta Vt / It \tag{5}$$

E-Physio also releases an electrocardiogram track (ECG). The bioimpedance signals are monitored using the LabCart Reader (Analog Devices, USA) beat-to-beat from the deriving electrodes on the athlete's thorax and visualized on a PC screen. From the LabCart software were acquired the following conditioning variables of the left ventricle stroke volume (SV): the thoracic fluid index (TFI, inverse of Zt) as electrical equivalent of the left ventricle pre-load, the electrical equivalent of left ventricular ejection velocity peak (EVI) and the ventricular ejection time (VET). Sramec-Bernstein equation –Equation (6)– consents to indirectly calculate the SV [11].

$$SV[cm^3] = TFI[\Omega^{-1}] \cdot EVI[\Omega\ s^{-1}] \cdot VET[s] \cdot VEPT[cm^3] \tag{6}$$

Equation (6), in addition to the three multipliers of purely bioimpedance origin, also contains a fourth multiplier: the volume of electrically participating tissues in thoracic impedance (VEPT), which is derived from nomograms based on anthropometric characteristics (weight and height) and gender (male or female) of the subject under examination. Based on the SV calculation, it is possible to obtain CO according to Equation (7).

$$CO\ [ml/min] = SV\ [ml] \cdot HR\ [beats/min] \tag{7}$$

The a-vO_2D assessment requires catheter placement, which is potentially hazardous and causes discomfort. Thus, direct measurement of a-vO_2D is not advisable in subjects not requiring invasive procedures for therapeutic or diagnostic purposes. However, several findings suggest that this parameter increases almost linearly and predictably with respect to workload [13-16]. Therefore, it would be possible to determine a-vO_2D and consequently VO_{2-max} with sufficient precision during an incremental exercise test.

Starting from the above observations, a model was constructed assuming that in healthy subjects the a-vO_2D at rest is on average 30% of total arterial O_2 content (CaO_2) and that it reaches 80% of CaO_2 at W_{max} during cycling exercise [13, 16 - 18].
Assuming that a-vO_2D increases linearly with workload [13-16], this variable expressed as a percentage of CaO_2 can be estimated using Equation (8).

$$a\text{-}vO_2D[\%\ of\ CaO_2] = 30\% + \{(80\%-30\%) / 100 \cdot \%W_{max}\} \tag{8}$$

In Equation (8), $\%W_{max}$ represents the workload percentage relative to the peak workload achieved. Then, to convert a-vO_2D into an absolute value, it is necessary to determine the CaO_2 quantity, which primarily results from the oxygen carried by hemoglobin, according to Equation (9) [16], where Hb is the blood hemoglobin concentration expressed in g dl^{-1} and HbO_{2-Sat} is the percentage of Hb saturated with O_2.

$$CaO_2 = 1.34 \cdot Hb \cdot HbO_{2-Sat} \tag{9}$$

C. *Experimental Protocol*
Each recruited cyclist underwent an incremental cardiopulmonary test (CPT), pedalling his bicycle connected posteriorly to the Elite Direto XR-T cycle-ergometer until exhaustion, thus reaching his peak workload (W_{max}) [19]. Each cyclist chose his pedalling frequency while the pedal load increased by 30W every two minutes starting from 0W. The load recorded during the final minute, measured in W, was considered his maximal load.
Immediately before the CPT and upon reaching W_{max}, the arterial blood oxygen saturation percentage was assessed via the finger device.
The data collected remotely via the E-Physio device required fundamental processing and selection to obtain accurate values for the studied variables. The impedance cardiography recording files were generated in '.txt' format. To visualize them as time-dependent analog traces, the 'LabChart Reader' software was utilized [20]. Once opened, the program enables longitudinal beat-to-beat observation of two primary variables: the ECG and the Zt. The LabChart software also allows monitoring of the heart rate per minute (HR) and first derivative thoracic impedance (dZt/dt) traces. Using the graphic cursor, EVI and VET were calculated beat-to-beat from the Zt trace. Along with the reciprocal Zt value, these represent the three impedance-based multipliers of the Sramek–Bernstein equation Equation (6) [21].

D. *Statistical Analysis*
Statistical analysis was performed using a two-tailed paired Student's *t*-test. Normality of the paired differences was assessed using the Kolmogorov–Smirnov test, which did not indicate deviation from normal distribution ($P > 0.1$) [22].

Methods agreement was evaluated by calculating the mean bias ($VO_2M - VO_2F$) and the relative percentage difference between methods.

3 RESULTS

Arterial oxygen saturation (S_aO_2) pracctically remained stable from W_0 (98.9 ± 0.3 %) to W_{max} (98.1 ± 0.4 %).
Table II presents mean values ± SD for all selected cardiometabolic variables across the seven cyclists, both at rest (W_0) and peak workload (W_{max}). Results clearly demonstrate statistically significant increases in heart rate (HR), stroke volume (SV), and CO at W_{max}. This table also indicates that the maximum oxygen consumption derived via the Fick equation (VO_2F) was nearly twelve times greater than the resting values measured before CPT. However, this value was statistically significantly lower—by approximately 22%—than the mean maximum oxygen consumption calculated for these athletes using the mathematical modeling of the Sitko empirical formula (VO_2M). Specifically, the VO_2F appears significantly underestimated when compared to the predictive accuracy typically associated with the alternative Sitko-based methodology within this cohort.

Table II – Mean ± SD values of cardiometabolic variables among seven tested athletes

Step	W *watt*	HR *b/min*	SV *ml*	CO *l/min*	VO_2F *ml/min*	VO_2M *ml/min*
W_0 ±SD	0	67 ±11	74.3 ±1.1	4.6 ±0.2	298 ±56	---
W_{max} ±SD	360 ±36	182* ±11	131.4* ±26	21.3* ±5.5	3543* ±498	4330** ±435
Δ%	---	+270	+178	+463	+1184	+22.2

W_0: rest; W_{max}: peak workload; HR: heart rate; SV: stroke volume; CO: cardiac output; VO_2F: oxygen consumption via Fick equation; VO_2M: oxygen consumption via Sitko empirical formula. *$p<0.05$ vs. resting conditions; **$p<0.05$ vs. VO_2F. Note that all variables were recorded during the incremental exercise test protocol.

$VO_{2\text{-}max}$ estimated via CP–W′-based modelling overestimated $VO_{2\text{-}max}$ based on Fick equation by approximately 22%, resulting in a significant underestimation of mechanical efficiency. In fact, the mean bias between VO_2M and VO_2F, shown in table II, reached +787 ml·min⁻¹, representing a relative overestimation of roughly 22%. Based on these data, metabolic power expenditure was determined assuming an energetic equivalent of 5 kcal per liter of oxygen and a mechanical equivalent of 4.18 W per cal. Consequently, peak metabolic power derived from Fick's approach ($W_{met\text{-}(F)}$) was computed using Equation (10), while peak metabolic power estimated through Sitko's model ($W_{met\text{-}(M)}$) was calculated using Equation (11).

$$W_{met\text{-}(F)} = VO_{2\text{-}max(F)}\ [ml/min] \cdot 5 \cdot 4.18 = 3543 \cdot 5 \cdot 4.18 = 74[kW/min] / 60[s] = 1234\ W \tag{10}$$

$$W_{met\text{-}(M)} = VO_{2\text{-}max(M)}\ [ml/min] \cdot 5 \cdot 4.18 = 4330 \cdot 5 \cdot 4.18 = 95\ [kW/min] / 60[s] = 1582\ W \tag{11}$$

Based on these results, considering that the peak mechanical power developed on average at the pedals by the athletes (W_{max}) was 360 W, we estimated the mean maximum cycling mechanical efficiency (η_{max}) using both Fick-based $W_{met\text{-}(F)}$ and CP–W′-based $W_{met\text{-}(M)}$ peak metabolic power calculations, as defined in Equations (12) and (13), respectively. This approach allows for a direct comparative assessment of efficiency across both distinct methodologies.

$$\eta_{max\text{-}F} = W_{max} / W_{met\text{-}(F)} = 360\ W / 1234\ W = 0.29 \quad (12)$$

$$\eta_{max\text{-}M} = W_{max} / W_{met\text{-}(M)} = 360\ W / 1582\ W = 0.20 \quad (13)$$

Consequently, cycling mechanical efficiency derived from the CP–W′-based empirical formulation was approximately 21% lower than that obtained via the Fick-based physiological estimation approach.

4 DISCUSSION

The here shown discrepancy concerning indirect metabolic power estimation based solely on mechanical parameters versus the direct physiological one based on the Fick principle may introduce bias when the former is applied to well-trained cyclists performing incremental exercise tests to exhaustion. These findings emphasize the necessity of experimentally validating CP–W′-based metabolic estimations when utilized outside their original calibration framework, particularly in high-performance athletes.
In this regard it should be state that the Fick principle, here utilized as the reference method to be compared with the CP–W′-based one for metabolic estimations, represents the physiological gold standard for measuring VO_2 [23, 24] since its validity is rooted in a fundamental physical law: the Law of Conservation of Mass. In simple terms, the amount of a substance taken up by an organ (or the entire body) is equal to the difference between the amount of that substance entering the organ and the amount exiting it, i.e. the O_2 entering in the body during breathing. So, as shown in equation (2), the direct Fick principle expresses $VO_{2\text{-}max}$ as the product of corresponding values of CO and the a-vO_2D where CO is the volume of blood pumped by the heart per minute, CaO_2 is the arterial oxygen content and the CvO_2 is the mixed venous oxygen content (sampled from the pulmonary artery). However, while the Fick method is considered highly accurate, more to the point, it is key that the following steps could be met during the measurement: a) sampling errors - even minor inaccuracies in measuring hemoglobin concentration or oxygen

saturation can lead to significant discrepancies in the final calculation of VO_2; b) steady state - the method is valid only when the subject is in a state of equilibrium or that both changes in CO and VO_2 show the same quickness; c) mixed venous blood content in O_2 - this represents the primary technical challenge since for absolute validity, venous blood must be sampled from the pulmonary artery (via a Swan-Ganz catheter) as the blood drawn from a peripheral vein is not representative of total body consumption because different organs extract oxygen at varying rates.

In agreement with the milestone experiment of Wasserman et al. [16], in the current one the condition (a) concerning the concentration of haemoglobin in the blood of each tested subject and the S_aO_2 at W_{max} were well within the physiological values. Concerning the condition (b), even if the steady state interval of the workload increase in the actual experiment was of 2 minutes, in a previous study the Wasserman's research team found that, in 8 healthy subjects who performed a cycle ergometer incremental test, the peak values of the parameters of aerobic function as VO_2, VO_2/W and others did not differ between exercise protocol in which the step increase duration was of 2 minutes or 3 minutes [25]. Concerning the condition (c), the actual experiment related with a previous one [26] from Crisafulli et al. in which a model for a-vO_2D estimation considers that this difference at rest was of 30% respect to the CaO_2 and that it increases linearly, during an incremental exercise on a cycle ergometer, reaching a value of 80% of CaO_2 at the peack workload, in agreement to what stated by Astrand and Rodahl in their classic textbook of work physiology [27]. It is important to note that in the experiment by Crisafulli et al. [26], the Fick equation was used to calculate the cardiac output while VO_2 was obtained with a clinical equipment using indirect calorimetry. The stroke volume (SV) values thus obtained practically overlapped with those obtained using an electrical impedance cardiometry device, a non invasive technique which consent to acquire beat-to-beat the left ventricle SV and which is now solidly validated by numerous comparative studies with other gold standard methods in healthy subjects and in cardiovascular patients [28, 29, 30, 31, 32]. Interesting, also in the above cited milestone paper of Wasserman et al. [16], in 5 aerobically well trained athletes performing a cycle ergometer exercise up to exhaustion, changes in CO were obtained by the equation (2) concerning the direct Fick method in which the VO_2 was assessed from a mass spectrometry device while the a-vO_2D was acquired respectively from a pulmonary artery catheter CvO_2 and a radial artery catheter CaO_2. However, data from this experiment show a statistically significant linear regression for the instrumentally measured VO_2 versus the catheters obtained a-vO_2D which means that in well trained subjects for aerobic exercise the volume of O_2 entering through lungs is linearly correlated with the cession volume of this gas to the working body tissues up to the maximum exercising work.

From all the above, it can be reasonably stated that the method based on the direct Fick principle used here to measure the maximum oxygen consumption in well-performing aerobic athletes such as our recruited cyclists is suitable to act as a reference method to evaluate the same metabolic variable acquired with another indirect system such as the CP–W′-based one.

As these results show, the CP–W′-based, mathematical method measured an athlete $VO_{2\text{-max}}$ which exceeded by 22% that measured with the Fick method. Since the Wmax was the same in both methods, it resulted, as show equations (12) and (13), that the maximum mechanical efficiency from the mathematical model was lower than 21%.

Since these findings indicate that mathematical model-based cardiometry overestimates maximal aerobic capacity, as it fails to account for the intrinsic constraints of oxygen transport, so the Fick method here adopted remains the essential benchmark for defining the actual physiological ceiling, whereas the CP-W' model describes the theoretical kinetics of a not realistic system characterized by progressive metabolic inefficiency which evolves asymptotically.

Practically, the mathematical model lead to an overestimation of $VO_{2\text{-max}}$ since it neglects the inherent limits of oxygen delivery. While the Fick method provides the necessary reference for the true physiological ceiling, the CP-W' model instead characterizes the theoretical kinetics of increasing metabolic inefficiency.

As a conclusion, data from this experiment demonstrate that $VO_{2\text{-max}}$ values derived from mathematical models are overestimated due to the omission of intrinsic oxygen transport limitations. On the contrary, unlike the CP-W' model which reflects the theoretical kinetics of metabolic decay, the Fick method serves as the gold standard for identifying the definitive physiological ceiling.

So, these results suggest that uncritical application of such empirical models may lead to potential bias in the interpretations of mechanical efficiency and energetic cost during cycling performance assessments, reinforcing the requirement for physiologically grounded measurement approaches supported by non-invasive instrumentation.

REFERENCES

[1] Gardner A.S., Stephens S., Martin D.T., Lawton E., Lee H. and Jenkins D., Accuracy of SRM and Power Tap power monitoring systems for bicycling. *Med. Sci. Sports Exerc.*, vol. 36, no. 7, pp. 1252–1258, 2004.

[2] Bouillod A., Soto-Romero G., Grappe F., Bertucci W., Brunet E. and Cassirame J., Caveats and recommendations to assess the validity and reliability of cycling power meters: A systematic scoping review. *Sensors*, Vol. 22, No. 1, pp. 386, 2022.

[3] VO_2 Master, "VO_2 Master Analyzer", Online Available: https://vo2master.com/product/analyzer/

[4] MedicalExpo, "Metabolic analyzer", Online Available: https://www.medicalexpo.com/ prod/mes/product 69379 - 690563.html

[5] Sitko S., Cirer-Sastre R., Corbi F. and López-Laval I., Five-minute power-based test to predict maximal oxygen consumption in road cycling. *Int. J. Sports Physiol. Perform.*, vol. 17, no. 1, pp. 9–15, 2022.

[6] Beck K.C., Randolph L.N, Bailey K.R., Wood C.M., Snyder E.M. and Johnson B.D., Relationship between cardiac output and oxygen consumption during upright cycle exercise in healthy humans. *J. Appl. Physiol*., vol. 101, pp. 1474–1480, 2006.

[7] Tocco F., Mattana D.V., Solinas R., Velluzzi F., Usai P., Fois A., Melis L., Bianco P., Serra C., Manuello Bertetto A., Dell'Osa A.H., Pereira A.F., Cerina A., Loviselli L., Marcello R., Melis S. and Concu A., Cardiometabolic benefits from a coastal sailing in a radical cystectomy patient remotely controlled by an Internet of Things mechatronic tool: A case study. *Int. J. Mech. Control*, vol. 24, no. 2, pp. 39–61, 2023.

[8] Tocco F., Solinas R., Velluzzi F., Massidda M., Mattana D.V., A. Fois, L. Melis, A. Manuello Bertetto, Bonisoli E.†, Venturini S., Bianco P., Dell'Osa A.H., Pereira A.H., Melis S., Cerina A., Loviselli L., Marcello R. and Concu A., A mechatronic tool for revealing inverse relationships among heart's stroke volume and head's linear acceleration induced by moored boats rolling in elderly sailors with unchanged body sizes: A non-drug anti-hypertensive advantage?. *Int. J. Mech. Control*, vol. 25, no. 1, pp. 133–142, 2024.

[9] Dell'Osa A.H., Fois A., Cerina A., Pili F., Manuello Bertetto A., Bellomi G., Palmas M., Ruggiu M., Melis S., Tocco F. and Concu A., Impedance cardiography assessment during body immersion in a high concentrated water solution of magnesium chloride simulating space microgravity: A pilot study. *J. Phys.: Conf. Ser.*, vol. 3014, p. 012006, 2025.

[10] Bridges N., Parvin R.M., and van Asseldeft O.W., Evaluation of a new system for hemoglobin measurement. *Am. Clin. Prod. Rev.*, vol. 6, pp. 22–25, 1987.

[11] Tocco, F., Crisafulli A.†, Marongiu E., Milia R., Kalb A., and Concu A., A portable device to assess underwater changes of cardiodynamic variables by impedance cardiography. *J. Phys.: Conf. Ser.*, vol. 407, p. 012026, 2012.

[12] Sitko S., Cirer-Sastre R. and López-Laval I., An update of the Allen & Coggan equation to predict 60-min power output in cyclists of different performance levels. *Int J Sports Med.*, Vol. 44, No. 13, pp. 983-987, 2023.

[13] Crisafulli A.†, Melis F., Tocco F., Santoboni U.M., Frongia F., Carta C., and Concu A., Anaerobic threshold and the oxygen consumption/cardiac output relationship during exercise. *Sport Sci. Health*, vol. 2, pp. 75–80, 2005.

[14] Crisafulli A.†, Tocco F., Pittau G., Caria M., Lorrai L., Melis F., and Concu A., Detection of lactate threshold by including haemodynamic and oxygen extraction data. *Physiol. Meas.*, vol. 27, pp. 85–97, 2006.

[15] Proctor D.N., Beck K.C., Shen P.H., Eickhoff T.J., Halliwill J.R. and Joyner M.J., Influence of age and gender on cardiac output–$\dot{V}O_2$ relationships during submaximal cycle ergometry. *J. Appl. Physiol.*, vol. 84, pp. 599–605, 1998.

[16] Stringer W., Hansen J.E. and Wasserman K., Cardiac output estimated noninvasively from oxygen uptake during exercise. *J. Appl. Physiol.*, vol. 82, pp. 908–912, 1997.

[17] Higginbotham M. B., Morris K.G., Williams R.S., McHale P.A., Coleman R.E. and Cobb F.R., Regulation of stroke volume during submaximal and maximal upright exercise in normal man. *Circ. Res.*, vol. 58, pp. 281–291, 1986.

[18] Lewis S.F., Taylor W.F., Graham R.M, Pettinger W.A., Schutte J.E. and Blomqvist C.G., Cardiovascular responses to exercise as functions of absolute and relative work load. *J. Appl. Physiol.*, vol. 54, pp. 1314–1323, 1983

[19] Tocco .F, Manuello Bertetto A., Velluzzi F., Roux A., Rosadelli S., Fois A., Deledda A., Cappai E.A., Melis S., Dell'Osa A.H., Cerina A., Marcello R. and Concu A., Remote assessment of cardiodynamic changes in competitive cyclists during an incremental cycle-ergometer test to exhaustion: a pilot study. *Int J of Mechanics and Control*, Vol. 26, No. 02, pp. 83-95. 2025.

[20] Manuello Bertetto A.,Tocco F., Bellomi G., Mulargia L., Ruggiu M., Palmas M., Massidda M., Ghiani G., Velluzzi F., Melis S., Fois A., Dell'Osa A.H., Cerina A., Bertelli U., Carta M.G., Bianco P.R. and Concu A., Cardiovascular and metabolic engagement after an endurance race in pilots driving motorboats electrically powered by green Energy. *Int J Mechanics and Control*. Vol. 26, No. 01, pp. 221-230, 2026.

[21] Tocco F., Ghiani G., Palmas M., Ruggiu M., Velluzzi F., Deledda A., Masala A., Fois A., Manuello Bertetto A., Dell'Osa A.H., Cerina A., Cappagli C., Melis S., Loi V., Marcello R. and Concu A., Remote monitoring of daily changes in cardiac mechanical efficiency and other cardiac parameters in a coastal kayaker over one-month of paddling. *Int J of Mechanics and Control*, Vol. 26, No. 2, pp. 97-111, 2025.

[22] Altman D.G., *Practical statistics for medical research*. Chapman and Hall, London, 1991.

[23] Fick, A., Über die Messung des Blutquantums in den Herzventrikeln. *Sitzungsber*. Phys-Med Ges Würzburg, 1870.

[24] Wasserman K., Hansen J.E., Sue D.J. and Whipp B.J., *Principles of Exercise Testing and Interpretation.* Lea & Febiger, Philadelphia. 1986.

[24] Y.Y, Johnson II M.C., Chow N. and Wasserman K., Effect of exercise testing protocol on parameters of aerobic function. *Med. Sci. Sports Exerc*., Vol. 23, No. 5, pp. 625-630, 1991.

[26] Crisafulli A.†, Piras F., Chiappori P., Vitelli S., Caria M.A., Lobina A., Milia R., Tocco F., Concu A. and Melis F., Estimating stroke volume from oxygen pulse during exercise. *Physiol. Meas*., Vol. 28, pp.1201-1212, 2007.

[27] Astrand P.O. and Rodahl K., (2003). *Textbook of Work Physiology.* McGraw-Hill, 2003.

[28] Handt A., Farber M.O. and Szwed J.J., Intradialytic measurement of cardiac output by thermodilution and impedance cardiography. *Clin. Nephrol*., Vol. 7, No. 2, pp. 61-64, 1977.

[29] Wilson M.F., Sung B.H., Pincomb G.A. and Lovallo W.R., Simultaneous measurement of stroke volume by impedance cardiography and nuclear ventriculo-graphy: comparisons at rest and exercise. *Ann. Biomed. Eng*., Vol. 17, No. 5, pp. 475-482, 1989.

[30] Concu A. and Marcello C., Stroke volume response to progressive exercise in athletes engaged in different training modes. *Eur. J. Appl. Physiol*., Vol. 66, pp. 11-17, 1993.

[31] Panagiotou M., Vogiatzis I., Jayasekera G., Louvaris Z., Mackenzie A., Mcglinchey N., Baker J.S., Church A.C., Peacock A.J. and Johnson M.K., Validation of impedance cardiography in pulmonary arterial hypertension. *Clin. Physiol. Funct. Imaging*, Vol. 38, No. 2, pp. 254-260, 2018.

[32] Filaire L., Perrault H., Dauphin C., Chalard A., Pereira B., Costes F. and Richard R., Agreement of concomitant cardiac output measurement by thoracic bio-impedance and inert gas rebreathing in healthy subjects. *Clin. Physiol. Funct Imaging*, Vol. 45, No. 3, pp. e70005, 2025.

ISSN 1590-8844
International Journal of Mechanics and Control, Vol. 27, No. 01, 2026
https://doi.org/10.69076/jomac.2026.0004

PRELIMINARY DESIGN OF A PASSIVE PRESSURE REDUCER WITH MULTIPLE ANNULAR CHAMBERS FOR AEROSPACE AND AERONAUTICAL SYSTEMS

Arash Safaei* Matteo Davide Lorenzo Dalla Vedova* Paolo Maggiore*

* Department of Mechanical and Aerospace Engineering, Politecnico di Torino, Italy

ABSTRACT

Both in the aeronautical and aerospace fields, the use of valves and active components along the fuel distribution system is fundamental. Most of these components are very complex, expensive and subject to failure. Redundancy in aerospace and aviation systems leads to a more reliable and robust system, but at the same time it allows potential optimization and implementation of dedicated components that can lighten and simplify the whole distribution fuel system, still guaranteeing the required performance. Clearly, due to the importance of fluid properties within the distribution line, the employed technology shall be very reliable and efficient, even while working in harsh environments. For this reason, the introduction of a passive component capable of reducing significantly the pressure of the working fluid has been studied. The Passive Pressure Reducer (PPR) analysed in this work does not require power, movable parts, springs, or other typical components installed inside the valves currently used in the aerospace and aeronautical systems. By integrating this component into specific locations within the fuel distribution line, it is possible to mitigate the action of certain components (valves, pumps, evaporators), and in some cases, pressure reducing valves can be excluded. As the fluid flows around and past the multiple annular chambers of the PPR, turbulent eddies will form. As a result of the interference of these chambers with the axial fluid flow, the fluid's pressure will decrease and energy will be lost. The PPR performance analysis is carried out through CFD simulations, to better understand the pressure drop through each chamber, and the global pressure jump through the component. The shape and size of the annular chambers affect the flow in terms of pressure and temperature, so it is crucial to design these chambers appropriately to achieve the desired output.

Keywords: Passive Pressure Reducer, Aerospace Fluid Systems, Annular Chambers, Lumped-Parameter Modelling, CFD Validation

1 INTRODUCTION

Pressure reducing valves play a crucial role in ensuring the safety, efficiency, and performance of several aerospace and aeronautical systems. In environments where precision and reliability are of the highest importance, these valves are used to control and regulate fluid pressure. Although pressure-reducing valves are essential components, they are not without complexities and challenges. Engineers and professionals in the aerospace and aeronautical industries must understand the vulnerabilities and limitations of these valves to design, maintain, and operate systems that meet the stringent requirements of these industries. In recent years, several studies have explored innovative approaches to valve design and modelling for aerospace fluid distribution systems. In particular, the increasing adoption of cryogenic fluids, such as liquid hydrogen (LH2), has motivated research efforts focused on the optimisation of piston-type valves capable of operating reliably under extreme thermal and mechanical loads [1]. Concurrently, the development of simplified fluid dynamic models for servo valves has provided efficient tools both for preliminary design activities and for diagnostic or prognostic strategies [2], while comprehensive numerical investigations have been carried out to assess the influence of temperature variations on pressure control valves [3] and to characterize the behaviour of pressure-compensated flow control configurations [4].

Contact author: Arash Safaei[1]

[1] C.so Duca degli Abruzzi 24, 10129, Turin, Italy.
E-mail: arash.safaei@polito.it

ISSN 1590-8844
International Journal of Mechanics and Control, Vol. 27, No. 01, 2026

The growing interest in hydrogen as an energy carrier for aviation, particularly in the context of fuel cell-powered aircraft, further reinforces the demand for compact, reliable, and lightweight components in the fluid distribution systems on board next-generation aircraft [5].

The Passive Pressure Reducer (PPR) presented in this work represents an innovative and robust device designed to significantly reduce fluid pressure without the need for conventional active or moving elements such as springs and spools. At the heart of PPR's design is the concept of employing multiple annular chambers strategically positioned within a convergent-divergent pipe. As the fluid enters the convergent section, it accelerates through the annular chambers, which lead to a consistent pressure drop. The absence of moving parts represents a key advantage, since it eliminates the failure modes typically associated with the wear of mechanical components, the fatigue of springs, or the contamination of sliding surfaces, thus enhancing the overall reliability of the device. Furthermore, the simplicity of the construction allows an easier integration of the PPR into existing fuel distribution architectures, with the additional benefit of reducing the maintenance effort and the global weight of the system.

The goal of this paper is therefore to provide a new pressure reducing technology, capable of ensuring a consistent pressure reduction, in a controlled, precise and safe way. A simplified Lump Parameter analysis will be provided, which models the contribution of the annular chambers in terms of pressure reduction. This model will be compared and validated through CFD simulations, in order to assess the validity of the presented PPR and the effective pressure drop achieved across the annular chambers. The combined use of a simplified lumped-parameter formulation and detailed CFD simulations is here adopted in order to take advantage of the strengths of both approaches: while the lumped-parameter model allows a rapid evaluation of the design choices and offers physical insight on the local contributions of each stage, the CFD analysis provides a high-fidelity description of the complex three-dimensional flow field inside the device.

2 LUMPED-PARAMETER ANALYSIS

The analysis of the PPR's architecture (Fig. 1) performed in this study is based on fundamental fluid dynamic principles and physics of flow through an orifice. Since the PPR is characterized by a series of orifices spaced by ring-shaped chambers within a conduit that exhibits convergent-divergent geometry, it is of utmost importance to set up a relationship between the volume flow rate through each individual orifice and the related pressure drop. For the purposes of the analysis, a pressure drops Δp of 23 bars through the entire PPR is set up as boundary condition, using liquid hydrogen (LH2) as operating fluid. The initial geometry of the PPR and the pressure drop at the boundary allow the resolution and closure of the fluid dynamic problem.

The most important parameters are then computed: the volume flow rate Q through the whole PPR, and the related discharge coefficient C_D.

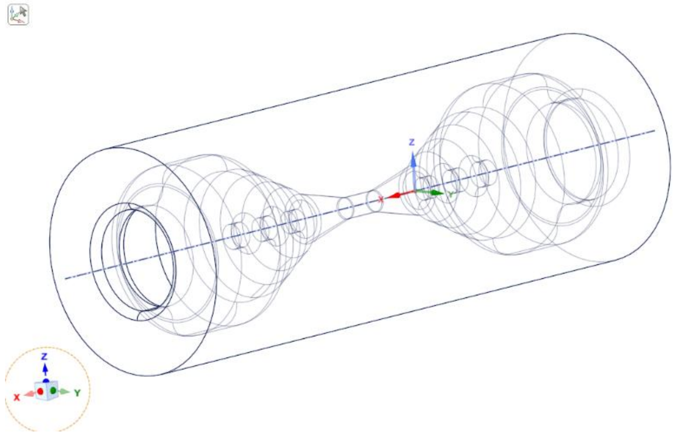

Figure 1 3D Model of the PPR.

The LH2 flow through the orifices of the PPR can be modeled, precisely, by considering the classical flow equations that result from mass, momentum and energy conservation. In this approach, the discharge coefficient C_d across the orifice is supposed only dependent on the Reynolds number, as it occurs for a circular section orifice [6]:

$$Q = C_d A \sqrt{\frac{2\,\Delta p}{\rho}} \tag{1}$$

where Q is the volume flow rate, C_d the orifice discharge coefficient, A the orifice area, Δp the pressure drops across the orifice and ρ the density of the operating fluid. In the considered scenario of a $\Delta p = 2.3 * 10^6\ Pa$ as pressure drop across the whole PPR, being the density of liquid hydrogen $\rho_{LH_2} = 70.97\ kg/m^3$, with dynamic viscosity $\mu_{LH_2} = 1.392 * 10^{-5}\ Pa\ s$ [7], with a throat diameter of $D = 5.34\ mm$, the resulting Reynolds number is of the order of magnitude of:

$$Re = \frac{\rho_{LH_2} v_t\, D}{\mu_{LH_2}} \cong 6.9 * 10^6 \tag{2}$$

with v_t the velocity of the flow across the throat of the PPR, which can be computed with good approximation with Bernoulli's equation. Since the orifices are designed with a rounded entrance edge and a live spike on the exit edge, it is known from orifice theory [8][9] that the contracting vein of the flow through this kind of circular orifice is of maximum thickness, therefore with a flow contraction coefficient C_c equal to 1 and a discharge coefficient C_d which ranges from 0.98 to 0.99 [10]. The discharge coefficient C_D of the whole PPR is the result of the combined discharge coefficients of the six orifices and the relative annular chambers; this parameter represents the efficiency which the orifice-annular chamber combination allows the passage of a certain volume flow rate with.

Therefore, the overall discharge coefficient C_D of the PPR can be estimated in first approximation as the multiplication of the C_{d,o_i} of all the orifices, minus the additional contribution C_{d,a_i} of each annular chamber, according to the following formula:

$$C_D = \prod_{i=1}^{6}(C_{d,o_i} - C_{d,a_i}) = \prod_{i=1}^{6}(C_{d,o_i} - \frac{5}{100}C_{d,o_i}) = \left(0.98 - 5\frac{0.98}{100}\right)^6 = 0.651 \quad (3)$$

The resulting C_D value of 0.651 approaches the asymptotic value of $C_D = 0.611$ (Von Mises, 1917), reached for high Reynolds numbers. The C_D value of the combined orifice-annular chamber is therefore equal to 0.931, lower than the value of 0.98 initially considered, but physically more realistic since the annular chamber itself also represents an additional obstacle that the flow must overcome. The volume flow rate Q can be easily computed through Eq. (1):

$$Q = C_D A_t \sqrt{\frac{2\,\Delta p}{\rho}} = 0.00371\ \frac{m^3}{s} \quad (4)$$

where A_t represents the area of the throat of the PPR, the minimum section that the flow encounters during its path from upstream to downstream. The value of Q computed in Eq. (4), which will be compared with the value obtained by the CFD analysis in the next session, represents the expected volume flow rate through the PPR, with a pressure drop set to 23 bar between upstream and downstream. In the presented architecture, each orifice is positioned in spatial succession with respect to the previous one, and this implies that the flow jet of the contracting vein that comes from one orifice conveys directly to the entrance of the next orifice. The result is a continuous and long jet which crosses all the orifices, taking the form of a column-shaped jet, as it will be shown in the CFD analysis. Furthermore, thanks to the performed CFD simulations, it will be noticeable that the annular chambers, in addition to allowing a gradual decrease in flow pressure, also enable the lamination of the flow maintaining it as a column-shaped jet through the orifice. This action prevents the flow from decelerating excessively as it crosses the stage constituted by the orifice and annular chamber, resulting in a continuous pressure decrease without significant pressure recoveries. By using Bernoulli equation, and taking into consideration the resistance effect of the discharge coefficient on the local pressure reduction, it is possible to approximate the pressure drop through each annular chamber by calculating the flow rate through each orifice, as reported in the following system:

$$\begin{cases} v_{i+1} = \sqrt{2\,\dfrac{\Delta p_i}{\rho_{LH_2}} + {v_i}^2} \qquad i = 1, \dots, 5 \\ v_i = \dfrac{Q}{A_i} \\ \Delta p_i = \dfrac{1}{{C_{d_i}}^2}\dfrac{1}{2}\rho_{LH_2}({v_{i+1}}^2 - {v_i}^2) \end{cases} \quad (5)$$

where v_i is the real velocity of the flow through orifice i, v_{i+1} is the velocity through the immediately next staged orifice *i+1* and C_{d_i} is the discharge coefficient of each orifice, assumed equal to 0.931 as previously computed.
The values of the theoretical velocity $v_{i+1,th}$, the real velocity v_{i+1} and the pressure drop Δp_i for each PPR's stage are computed through the equations of system Eq. (5) and listed in the following table:

Table I - Pressure drop contribution Δp_i of each stage

Stage n°	v_{i+1} **[m/s]**	Δp_i**[bar]**
1	128.3	5.80
2	157.2	3.38
3	188.9	4.39
Throat	206.3	2.82
4	177.8	4.48
5	199.5	3.35
6	236.9	6.68
Total Δp		21.94

According to this lumped-parameter analysis presented in this work, the maximum flow velocity reached in the final stage of the PPR, corresponding to the orifice n° 6, is equal to 236.9 m/s, while the total pressure drop across the PPR is around 21.94 bar, close to the pressure boundary condition value set equal to 23 bar. This data will be compared with the results of the CFD analysis in the following section.
It is worth noting that the small discrepancy between the imposed boundary condition of 23 bar and the computed total pressure drop of 21.94 bar can be attributed to the simplifying assumptions adopted in the lumped-parameter formulation, in particular the use of a constant discharge coefficient for all the stages and the neglect of viscous losses within the annular chambers.

3 CFD SIMULATION

The purpose of the CFD in this paper is specifically to validate the results obtained from the lump-parameter analysis, to better understand and predict the behaviour of the PPR in terms of pressure reduction and distribution. Special attention is needed for the description of the boundary layer; since the capture of the viscous effect on the wall is fundamental to ensure the convergence and fluid dynamic accuracy of the simulations, a sufficient number of layers must be provided.
To create a suitable and reliable mesh, it is necessary to ensure a good geometry's tessellation, so as to approximate as much as possible the shape of the orifices to that of a circle rather than of a polygon. In this way it is possible to capture with high resolution the pressure and velocity field of the fluid in the proximity of the orifices.

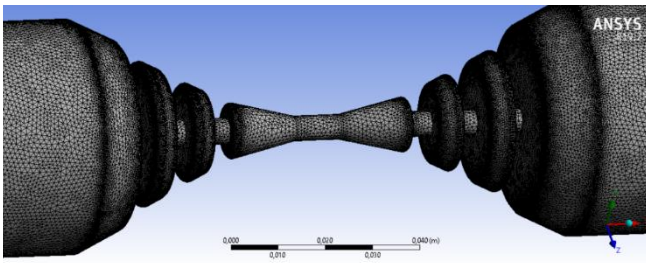

Figure 2 Volume Mesh with Tetrahedral cells.

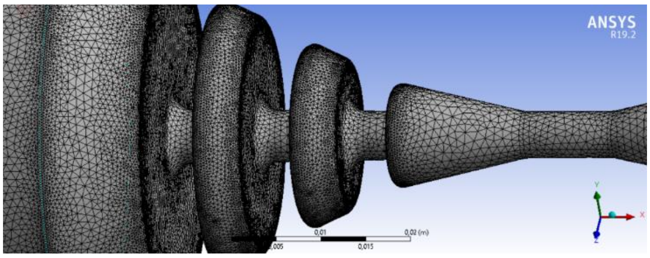

Figure 3 Closeup View of the Annular Chambers Volume Mesh.

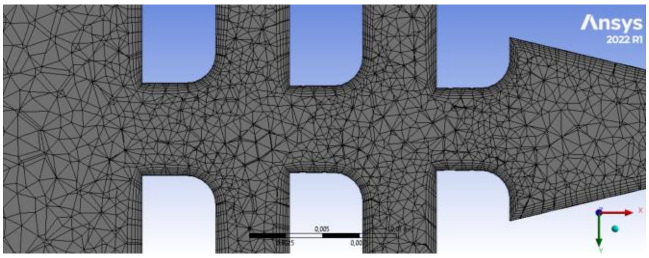

Figure 4 Cross-Section View of the Internal Volume Mesh.

3.1 GEOMETRY AND MESHING

ANSYS Fluid Flow (Fluent) software is used for meshing. Patch conforming and tetra dominant shell mesh is used as well as tetra/mixed volume meshing with tetrahedrons mesh method. The volume mesh is shown in Fig. 2. The Prism mesh is used in the entire wall to ensure accurate simulation of boundary layer. The inflation method adopted is the smooth transition, extending from the first layer with a growth ratio of 1.2 for 15 layers. Mesh quality values is used to assess the quality of the mesh and to ensure no negative volume exists in the mesh. Minimum element quality is 0.22 with maximum mesh quality of 1, averaging at 0.90 for a total of 8,976,503 elements. Therefore, the mesh is suitable for the simulation. A particular attention has been devoted to the refinement of the mesh in the proximity of the orifices and inside the annular chambers, where the strongest velocity and pressure gradients are expected. The progressive refinement allows to capture with adequate fidelity the formation and the development of the recirculation patterns generated downstream of each orifice, which play a fundamental role in the dissipative behavior of the device.

3.2 SOLVER SETTING

Fluid Flow (Fluent) solver is used to solve Reynolds-Averaged steady state Navier-Stokes equation with k-Omega SST turbulence model, with an inviscid flow. The wall is set to no-slip, with an inlet and outlet pressure driven boundary conditions. The choice of the turbulent model is decisive for the quality of the results. Generally, two turbulent models are widely used in CFD problems: k-ω and k-ε models. The main difference between the two models is that k-Epsilon model poorly resolves the viscous layer, unlike k-Omega model [11]. Furthermore, k-ω model is good in resolving internal flows, separated flows and jets and flows with high-pressure gradient and also internal flows through curved geometries like the PPR's orifices [12]. Considering the advantages and disadvantages of the considered models, the k-omega SST formulation is chosen eventually to perform the simulations, owing to the fact that it combines the best of the k-ω and k-ε models [13]. In particular, the SST formulation employs the k-ω model in the near-wall region to accurately resolve the boundary layer, and progressively switches to the k-ε model in the free-stream region, where the latter is known to provide more reliable predictions. This hybrid behavior makes the k-omega SST particularly well suited for the simulation of complex internal flows characterized by significant adverse pressure gradients and strong streamline curvature, as those occurring inside the PPR.

4 RESULTS AND DISCUSSION

All performed simulations satisfy the convergence criterion with less than 2000 iterations, as can be seen from Fig. 5. The net residual of the solution is of the order of magnitude of 10^{-5}, thus the results of the CFD can be considered steady with negligible fluctuations. The CFD simulations carried out show and enhance how crucial the importance of variable orifice's section spaced by the annular chambers is. The annular chambers force the flow to maintain the high speed reached in the contraction vein jet without a substantial pressure recovery. The geometrical conformation of the chambers allows the circular crown that surrounds the central jet through the orifices to maintain the flow in the form of a column-shaped jet, as can be noticed in Fig. 6. By dividing the orifices into several stages, and then employing multiple pressure drops that are more contained than a single orifice in which 23 bars are reduced in a single stroke, the flow speed in the orifice can be limited. Consequently, having more pressure drops contained in the stages allows for a smaller final pressure gradient in the PPR. The CFD's output values of the velocity v_i and the pressure drop Δp_i for each PPR's stage are reported in the following table:

Table II - CFD's output

Stage n°	$\boldsymbol{v_{i+1}}$ **[m/s]**	$\boldsymbol{\Delta p_i}$**[bar]**
1	120.0	6.03
2	140.1	3.02
3	165.7	3.95
Throat	204.5	2.50
4	125.1	2.40
5	183.5	3.05
6	210.8	6.90
Total $\boldsymbol{\Delta p}$		23.05

As can be seen from Table 2, the total pressure drop of the CFD's value through the PPR is equal to 23.05 bar, practically overlapping with the 23 bar set at the boundary condition of the lumped-parameter problem. The discharge coefficient C_d derived from the CFD is equal to:

$$C_D = \frac{Q}{A_t\sqrt{\frac{2\,\Delta p}{\rho}}} = 0.662 \tag{6}$$

whose value shows a minimum discrepancy with respect to the value of 0.651 computed in Eq. (3). Therefore, the modeling of the contributions of individual orifice and annular chamber of each stage of the PPR performed in the previous sections, in terms of the global discharge coefficient C_D and contraction coefficient C_c, is accurate and consistent with the CFD results here reported. The good agreement between the lumped-parameter prediction and the CFD outcomes confirms that the proposed simplified analytical framework can be reliably exploited as a preliminary design tool for the PPR. This is particularly valuable in the context of system-level optimization activities, where many geometrical configurations may need to be explored in a limited amount of time, and where the high computational cost associated with full three-dimensional CFD simulations would represent a major limitation. The presented results also highlight that the stage-wise pressure reduction approach adopted in the PPR design effectively distributes the global pressure drop among the individual orifices, preventing the onset of localized phenomena such as cavitation or excessive flow acceleration that could compromise the structural integrity of the device.

5 CONCLUSIONS

A simplified lumped-parameter analysis and related CFD simulation are presented and discussed. The reported fluid dynamic analysis is able to describe the key feature of the Passive Pressure Reducer (PPR) in terms of controlled pressure drop. The performed analysis is therefore able to predict the behavior of a CFD simulation with good accuracy, including the effect and contributions of each stage, made of the combination of a proper designed orifice and annular chamber. Strategic placement of multiple annular chambers within the passive pressure reducer allows progressive pressure reduction along the flow path. Each chamber performs as a stage in the pressure reduction process, with the combined effect of these annular chambers producing a pressure reduction that is precisely tuned and stable. The absence of active or moving parts further enhances the inherent reliability of the device, making it particularly attractive for aerospace applications where the operational environment is characterized by harsh thermal and mechanical conditions. Future work will focus on testing the PPR in different testing environments and pressure conditions, to get experimental data and assess the maximum operating range that this device is capable to withstand still guaranteeing high efficiency in volume flow rate passage and depressurization.

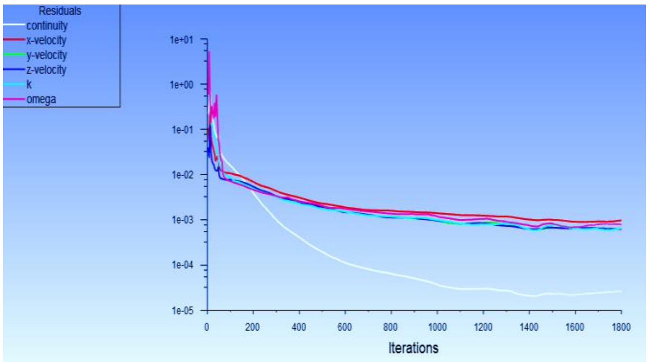

Figure 5 Convergence Plot of the simulation performed with ANSYS.

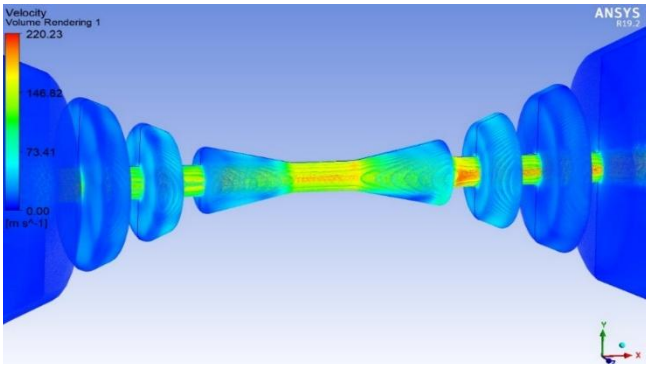

Figure 6 Volume mesh rendering of the velocity field across the orifices and annular chambers.

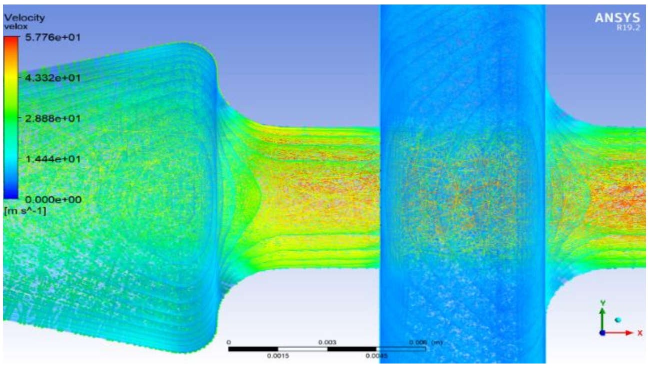

Figure 7 Closeup view of the mesh rendering around the orifice.

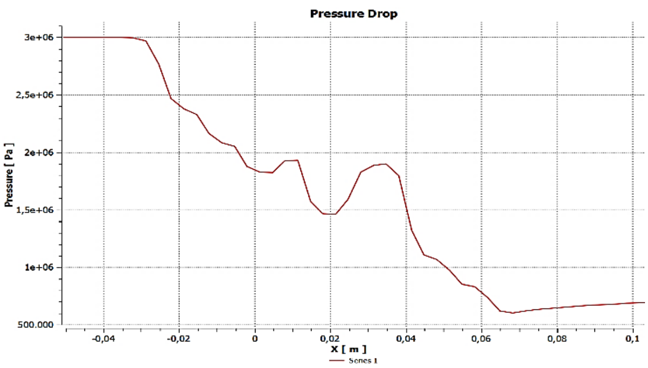

Figure 8 Pressure drop across the PPR, from inlet (left side) to outlet (right side).

In addition, further investigations will be devoted to the parametric optimization of the PPR geometry, with particular attention to the shape, size, and number of the annular chambers, with the aim of identifying the most effective configuration for a given target pressure drop and operating fluid.

REFERENCES

[1] Safaei A., Dalla Vedova M.D.L. and Maggiore P., CFD-based design and optimization of a cryogenic piston valve for liquid hydrogen flow control. *International Journal of Mechanics and Control*, Vol. 26, No. 02, pp. 69–82, 2025.

[2] Aimasso A., Alimhillaj P., Bertone M., Ferro C.G. and Dalla Vedova M.D.L., A new servovalve simplified fluid dynamic model sensitive to system hydraulic capacities. *International Journal of Mechanics and Control*, Vol. 25, No. 01, pp. 161–171, 2024.

[3] Alimhillaj P., Poçari S., Lamani L. and Dorri A., Numerical model and simulation for the influence of temperature on the pressure control valve in an oleodynamic system. *International Journal of Mechanics and Control*, Vol. 24, No. 02, pp. 63–68, 2023.

[4] Poçari S., Alcani M., Alimhillaj P., Londo A. and Hoxha A., Numerical and experimental study of the pressure-compensated flow control valve in an hydraulic system using mathematical model and LabView. *International Journal of Mechanics and Control*, Vol. 25, No. 01, pp. 69–75, 2024.

[5] Favre S., Di Fede F., Brusa E. and Delprete C., Innovative thermal management systems for fuel cell electric aircraft. *International Journal of Mechanics and Control*, Vol. 26, No. 01, pp. 159–183, 2025.

[6] Pace L., Ferro M., Fraternale F., Dalla Vedova M., Caimano A. and Maggiore P., Comparative Analysis of a Hydraulic Servo-Valve. *International Journal of Fluid Power*, No. 2, pp. 53–62, 2013.

[7] Kim H.I., Han K.Y. and Park J.H., *Liquid Hydrogen Properties*. HANARO Utilization Technology Development Div, p. 32, 2004.

[8] NACA Technical Note 1947, *Investigation of Flow Coefficient of Circular, Square and Elliptical Orifices at high pressure ratios*. Numeric-GmbH 2010-2018.

[9] NACA Technical Note 3466, *Investigation of the Discharge and Drag characteristics*. Numeric-GmbH 2010-2018.

[10] Ahmed M.A., Mostafa A.A., Comparative Study Between Different Orifice Shapes in Terms of the Effect of Pressure Head on the Discharge Coefficient. *Al-Azhar University Civil Engineering Research Magazine (CERM)*, Vol. 41, No. 4, October 2019.

[11] Minsheng Z., Decheng Wa, and Yangyang G., Comparative Study of Different Turbulence Models for Cavitational Flows around NACA0012 Hydrofoil. *Journal of Marine Science and Engineering*, MDPI, 2021.

[12] Thakare H.R., Parekh A.D., CFD analysis of energy separation of vortex tube employing different gases, turbulence models and discretisation schemes. *International Journal of Heat and Mass Transfer*, Vol. 78, pp. 360–370, November 2014.

[13] Menter, F. R., Zonal Two Equation k-ω Turbulence Models for Aerodynamic Flows. AIAA Paper 93-2906, 1993.

[14] Shivarudrappa K.B., Sargunar E.V.M. and Sakthivadivel R., An Experimental Investigation of Pressure Recovery Factor in Discharging Manifolds. *6th Australasian Hydraulics and Fluid Mechanics Conference*, Adelaide, Australia, 5–9 December 1977.

ISSN 1590-8844
International Journal of Mechanics and Control, Vol. 27, No. 01, 2026
https://doi.org/10.69076/jomac.20XX.00YY

TEMPLATE FOR PREPARING PAPERS FOR PUBLISHING IN INTERNATIONAL JOURNAL OF MECHANICS AND CONTROL

Author1* Author2**

* affiliation Author1

** affiliation Author2

ABSTRACT

This is a brief guide to prepare papers in a better style for publishing in International Journal of Mechanics and Control (JoMaC). It gives details of the preferred style in a template format to ease paper presentation. The abstract must be able to indicate the principal authors' contribution to the argument containing the chosen method and the obtained results. (max 200 words)

Keywords: keywords list (max 5 words)

1 TITLE OF SECTION (E.G. INTRODUCTION)

This sample article is to show you how to prepare papers in a standard style for publishing in International Journal of Mechanics and Control.
It offers you a template for paper layout, and describes points you should notice before you submit your papers.

2 PREPARATION OF PAPERS

2.1 SUBMISSION OF PAPERS

The papers should be submitted in the form of an electronic document, either in Microsoft Word format (Word'97 version or earlier).
In addition to the electronic version a hardcopy of the complete paper including diagrams with annotations must be supplied. The final format of the papers will be A4 page size with a two column layout. The text will be Times New Roman font size 10.

Contact author: author1[1], author2[2]

[1]Address of author1.
[2]Address of author2 if different from author1's address
E-mail: author1@univ1.com , author2@univ2.com

2.2 DETAILS OF PAPER LAYOUT

2.2.1 Style of Writing

The language is English and with UK/European spelling. The papers should be written in the third person. Related work conducted elsewhere may be criticised but not the individuals conducting the work. The paper should be comprehensible both to specialists in the appropriate field and to those with a general understanding of the subject.
Company names or advertising, direct or indirect, is not permitted and product names will only be included at the discretion of the editor. Abbreviations should be spelt out in full the first time they appear and their abbreviated form included in brackets immediately after. Words used in a special context should appear in inverted single quotation mark the first time they appear. Papers are accepted also on the basis that they may be edited for style and language.

2.2.2 Paper length

Paper length is free, but should normally not exceed 10000 words and twenty illustrations.

2.2.3 Diagrams and figures

Figures and Tables will either be entered in one column or two columns and should be 80 mm or 160 mm wide respectively. A minimum line width of 1 point is required at actual size. Captions and annotations should be in 10 point with the first letter only capitalised *at actual size* (see Figure 1, Figure 2, Table VII and Table VIII).

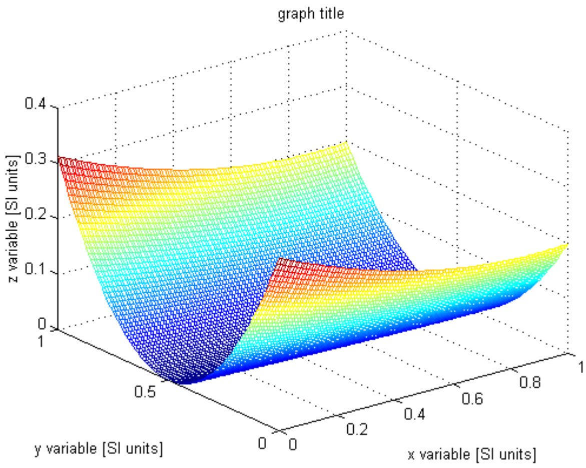

Figure 1 Simple chart.

Table VII - Experimental values

Robot Arm Velocity (rad/s)	Motor Torque (Nm)
0.123	10.123
1.456	20.234
2.789	30.345
3.012	40.456

2.2.4 Photographs and illustrations

Authors could wish to publish in full colour photographs and illustrations. Photographs and illustrations should be included in the electronic document and a copy of their original sent. Illustrations in full colour …

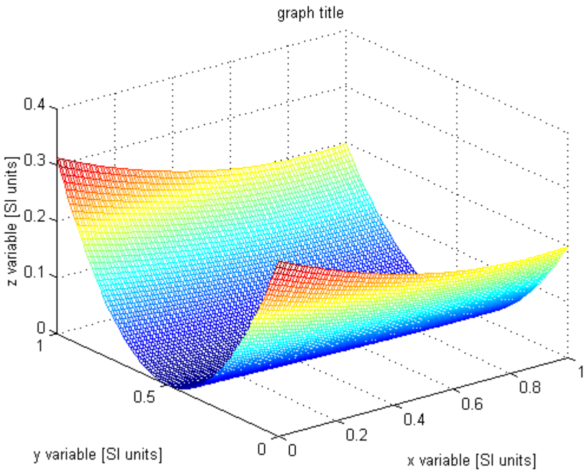

Figure 2 Simple chart.

2.2.5 Equations

Each equation should occur on a new line with uniform spacing from adjacent text as indicated in this template. The equations, where they are referred to in the text, should be numbered sequentially and their identifier enclosed in parenthesis, right justified. The symbols, where referred to in the text, should be italicised.

- point 1
  - point 2
    - point 3

1. numbered point 1
   2. numbered point 2
      3. numbered point 3

$$W(d) = G(A_0, \sigma, d) = \frac{1}{T}\int_0^{+\infty} A_0 \cdot e^{-\frac{d^2}{2\sigma^2}} dt \tag{1}$$

3 COPYRIGHT

4 PEER REVIEW

Papers for publication in JoMaC will first undergo review by anonymous, impartial specialists in the appropriate field. Based on the comments of the referees the Editor will decide on acceptance, revision or rejection. The authors will be provided with copies of the reviewers' remarks to aid in revision and improvement where appropriate.

5 REFERENCES (DESCRIPTION)

The papers in the reference list must be cited in the text. In the text the citation should appear in square brackets [ ], as in, for example, "the red fox has been shown to jump the black cat [3] but not when...". In the Reference list the font should be Times New Roman with 10 point size. Author's first names should be terminated by a 'full stop'. The reference number should be enclosed in brackets.

The book titles should be in *italics*, followed by a 'full stop'. Proceedings or journal titles should be in *italics*. For instance:

Table VIII - Experimental values

Robot Arm Velocity (rad/s)	Motor Torque (Nm)	Motor Torque (Nm)	Motor Torque (Nm)
0.123	10.123	10.123	10.123
1.456	20.234	20.234	20.234
2.789	30.345	30.345	30.345
3.012	40.456	40.456	40.456

REFERENCES (EXAMPLE)

[1] Smith J., Jones A.B. and Brown J., *The title of the book*. 1st edition, Publisher, 2001.

[2] Smith J., Jones A.B. and Brown J., The title of the paper. *Proc. of Conference Name*, where it took place, Vol. 1, paper number, pp. 1-11, 2001.

[3] Smith J., Jones A.B. and Brown J., The title of the paper. *Journal Name*, Vol. 1, No. 1, pp. 1-11, 2001.

[4] Smith J., Jones A.B. and Brown J., *Patent title*, U.S. Patent number, 2001.

International Journal of Mechanics and Control – JoMaC
Published by ASTRA M B S.R.L.

TRANSFER OF COPYRIGHT AGREEMENT

NOTE:
Authors/copyright holders are asked to complete this form signing section A, B or C and mail it to the editor office with the manuscript or as soon afterwards as possible.

Editorial Secretary address:
Andrea Manuello Bertetto
Matteo D. L. Dalla Vedova, Simone Venturini, Alessandro Aimasso
Dept. of Mechanical and Aerospace Engineering
Politecnico di Torino
C.so Duca degli Abruzzi, 24 – 10129 Torino – Italy
e_mail: jomac@polito.it
fax n.: +39.011.090.6999

The article title:

By:____

To be Published in ***International Journal of Mechanics and Control JoMaC***
Official legal Turin court registration Number 5320 (5 May 2000) - reg. Tribunale di Torino N. 5390 del 5 maggio 2000

A Copyright to the above article is hereby transferred to the JoMaC, effective upon acceptance for publication. However the following rights are reserved by the author(s)/copyright holder(s):
1. All proprietary rights other than copyright, such as patent rights;
2. The right to use, free or charge, all or part of this article in future works of their own, such as books and lectures;
3. The right to reproduce the article for their own purposes provided the copies are not offered for sale.

To be signed below by all authors or, if signed by only one author on behalf of all co-authors, the statement A2 below must be signed.

A1. All authors:

SIGNATURE______________________________DATE__________ SIGNATURE______________________________DATE__________

PRINTED NAME____________________________________ PRINTED NAME____________________________________

SIGNATURE______________________________DATE__________ SIGNATURE______________________________DATE__________

PRINTED NAME____________________________________ PRINTED NAME____________________________________

A2. One author on behalf of all co-authors:
"I represent and warrant that I am authorised to execute this transfer of copyright on behalf of all the authors of the article referred to above"

PRINTED NAME____________________________________

SIGNATURE______________________________ TITLE____________________________ DATE____________

B. The above article was written as part of duties as an employee or otherwise as a work made for hire. As an authorised representative of the employer or other proprietor. I hereby transfer copyright to the above article to *International Journal of Mechanics and Control* effective upon publication. However, the following rights are reserved:
1. All proprietary rights other than copyright, such as patent rights;
2. The right to use, free or charge, all or part of this article in future works of their own, such as books and lectures;
3. The right to reproduce the article for their own purposes provided the copies are not offered for sale.

PRINTED NAME____________________________________

SIGNATURE______________________________ TITLE____________________________ DATE____________

C. I certify that the above article has been written in the course of employment by the United States Government so that no copyright exists, or by the United Kingdom Government (Crown Copyright), thus there is no transfer of copyright.

PRINTED NAME____________________________________

SIGNATURE______________________________ TITLE____________________________ DATE____________

CONTENTS

NEWS FROM THE JOMAC EDITORIAL BOARD:

Starting from the June 2024 issue, JoMaC provides an Open Access service to our authors.
You are invited to visit the JoMaC website (http://www.jomac.it) for further details.